UNIVERSITE DE STRASBOURG

École doctorale MSII

ICube - UMR 7357

THÈSE présentée par :

Nadège CORBIN

pour obtenir le grade de: **Docteur de l'université de Strasbourg**

Discipline/ Spécialité: **SIAR-Génie Biomédical**

soutenue le : **14 Décembre 2015**

Interventional Magnetic Resonance Elastography dedicated to the monitoring of percutaneous thermal ablations

Directeur de thèse

Michel de Mathelin	Professeur, Université de Strasbourg

Rapporteurs

Bruno Quesson	Directeur de recherche CNRS, IHU Bordeaux
Ingolf Sack	Professeur, Charité - Universitätsmedizin Berlin

Examinateurs

Benoît Larrat	Chargé de recherche, CEA Saclay
Elodie Breton	Ingénieur de recherche CNRS, Université de Strasbourg
Jonathan Vappou	Chargé de recherche CNRS, Université de Strasbourg

Résumé Les ablations thermiques percutanées permettent aujourd'hui de traiter des tissus cancéreux en minimisant les risques de complication. L'Imagerie par Résonance Magnétique (IRM) est une modalité d'imagerie très appréciée pour le suivi de ces procédures minimalement invasives, notamment parce qu'elle permet la mesure de la température en temps réel. Néanmoins, aucune information directement reliée aux propriétés structurelles du tissu traité n'est disponible. Puisque la possibilité de mesurer les propriétés mécaniques des tissus grâce à l'Elastographie par Résonance Magnétique (ERM) a largement été démontrée, l'objectif de ce travail de doctorat est de développer un système d'ERM interventionnelle permettant d'étudier l'évolution des propriétés mécaniques des tissus au cours de l'ablation. A l'heure actuelle, les dispositifs d'ERM ne répondent pas aux contraintes de l'IRM interventionnelle en termes de rapidité et d'encombrement. Un système tout-en-un d'ERM interventionnelle a donc été développé spécifiquement pour cette application. L'onde mécanique est générée par la vibration d'une aiguille directement au sein de la région d'intérêt. Le mouvement induit par cette excitation est encodé par une séquence rapide et interactive. Un algorithme de résolution de problème inverse permet de mesurer l'élasticité et la température en temps réel. Grâce à ce système, les modifications des propriétés mécaniques des tissus ont pu être observées pour la première fois en temps réel lors d'ablations thermiques *ex vivo* et *in vivo*. Une nouvelle méthode de traitement des données ERM est aussi proposée afin de s'affranchir d'étapes conventionelles fastidieuses. Cette alternative permet d'obtenir l'information d'élasticité sans reconstruction au préalable d'images de phase. La pertinence et la faisabilité de la méthode ont été démontrées grâce à des expériences sur gélatine et *in vivo*.

Mots-clés: Elastographie, Imagerie par Resonance Magnétique, ablation thermique, IRM interventionnelle

Abstract Percutaneous thermal ablations have emerged as an efficient alternative to open-surgery for the destruction of cancerous tissue while minimizing the complication rate. Magnetic Resonance Imaging (MRI) is appreciated to monitor these minimally-invasive procedures, especially because the temperature of the ablated region can be measured in real-time. Nevertheless, no information related to structural properties of the tissue is available during the procedure. The possibility of measuring mechanical properties by Magnetic Resonance Elastography (MRE) has already been clearly demonstrated but the current systems do not meet the demanding conditions of interventional MRI in terms of bulk and update rate. The objective of this doctoral work is therefore to develop interventional MRE dedicated to the monitoring of percutaneous thermal ablations. The designed system is composed of a needle MRE driver that generates waves directly within the region of interest, a fast and interactive MR pulse sequence that encodes the motion on MR phase images and an inverse problem solver that reconstructs elasticity maps in real-time. Thanks to this interventional MRE system, the temporal evolution of elasticity and temperature induced by *ex vivo* and *in vivo* thermal ablations were successfully observed in real-time for the first time. An innovative method for MRE data processing was also proposed in order to avoid challenging steps of the conventional process. This alternative consists in obtaining elasticity information without reconstructing any phase image. Promising results obtained in phantoms and *in vivo* have demonstrated the relevance and the feasibility of the method.

*Key-words:*Elastography, Magnetic Resonance Imaging, thermal ablation, interventional MRI

Remerciements

Voici probablement la partie de ce manuscrit la plus difficile à écrire. Elle ne requiert aucune connaissance scientifique ni équation mathématique mais fait appel à des capacités littéraires oubliées afin de remercier avec justesse et sincérité chacune des nombreuses personnes qui ont contribué au bon déroulement de ces trois années.

Pour commencer je remercie l'IHU de Strasbourg qui a financé ce projet de thèse et m'a permis de le réaliser dans d'excellentes conditions. Je remercie aussi le service de radiologie interventionnelle du Nouvel Hopital Civil qui m'a accueillie de nombreux mercredis avec mes petits bocaux de gélatine.

Je tiens aussi grandement à remercier Michel, de m'avoir permis de réaliser ma thèse dans son laboratoire et d'avoir accepté la supervision de mes travaux de recherches en étant présent à chaque fois que j'en avais besoin malgré un agenda de ministre.

Evidemment, je remercie Elodie et Jonathan, de m'avoir encadrée de manière aussi impliquée. Je les remercie de m'avoir transmis leurs connaissances, de m'avoir emmenée avec eux lors des conférences, d'avoir consacré des journées avec moi devant l'IRM, d'avoir su me rebooster en cas de petite crise de pessimisme occasionnelle, de m'avoir laissé la liberté de développer mes propres idées et enfin d'avoir instauré ce climat de confiance sympathique et agréable. Pour compléter notre petite équipe d'IRM perdue dans ce grand labo de roboticiens, nous sont venus en aide Simon avec son énergie et sa bonne humeur ainsi que Pramod avec son savoir-faire et sa gentillesse.

De même, je souhaite remercier tous les membres du laboratoire et tout particulièrement ceux qui se sont penchés sur la réalisation de l'excitateur mécanique qui suscite toujours autant de curiosité à chaque conférence.

Mais cette thèse n'aurait pu aussi bien se dérouler sans hydratation hebdomadaire au Xanadu, sans compétition ardue sur les terrains de basket, sans pratique assidue du sens critique entre filles, sans voyage instructif dans des hôtels miteux ou des campings sous la tempête, sans exercice d'expression vocale sur bande-son de Mommy, sans débat constructif (ou pas) chaque midi au Stift, bref sans le soutien, la complicité et les délires des doctorants de ce labo : Cédric, Gauthier, Quentin, Arnaud, Nicole, Paolo, Markus, Laure, François, et Mathilde (t'inquiète pas ça passera sans problème!). Je remercie aussi les stagiaires et ingénieurs qui se sont incrustés au cours de ces trois années et qui ont aussi contribué à cette formidable ambiance de travail : Benoît, Florent, David, Thomas et Jérôme. Bien

entendu, je tiens à remercier tout particulièrement Emeric qui a eu la merveilleuse idée de débarquer au milieu de cette joyeuse bande d'illuminés.
Naturellement, un grand merci à ma famille qui me soutient dans toutes mes décisions en me faisant toujours croire que ce sont les meilleures.
Enfin, une petite dédicace s'impose: à tous ces petits cochons qui ont donné leur vie à la science ...

Contents

List of Figures

List of Tables

Introduction

In the fight against cancer, each advance in the medical research is intended to increase the longevity of the patient while ensuring him the highest quality of life possible. All scientific areas are mobilized and their alliance allows to develop efficient and reliable diagnostic and therapeutic tools. Among them, interventional magnetic resonance imaging (MRI) results from the combination of numerous fields of competence: mathematics, physics, chemistry and medicine. Interventional MRI allows performing minimally invasive procedures under MRI guidance to destroy cancerous tissue while reducing the complication rate and improving the comfort of the patient. The tumor can be destroyed by thermal ablation that consists in locally heating or freezing the tissue. Monitoring thermal ablations is essential to ensure the complete destruction of the cancerous tissue and avoid damages to surrounding tissues. Temperature measurement in real-time is available in MRI but no intrinsic information about the alteration of structural properties of tissue is provided. Based on published studies, providing information about mechanical properties in real-time during the procedures is expected to improve the control and thereby increase the reliability and efficiency of percutaneous thermal ablations. Magnetic Resonance Elastography (MRE), through an alliance of biomechanical and MRI skills, makes possible the non-invasive measurement of mechanical properties of tissues. Today, MRE is an accepted clinical tool used for the diagnosis of cancerous tissues that are associated to a change in mechanical properties. However, MRE can not be used for the real-time monitoring of thermal ablations in its current form because the requirements of interventional MRI in terms of bulk, acquisition and data processing speed are not met. The current project aims at adapting diagnostic MRE to interventional MRI in order to provide information about mechanical properties in real time and thereby improve the monitoring of percutaneous thermal ablations.

In this context, this doctoral thesis proposes an all-in-one interventional MRE system dedicated to the monitoring of percutaneous thermal ablations. The device is adapted to the interventional MRI environment. Acquisition time and processing time are optimized to meet the needs of interventional MRI. The feasibility of monitoring thermal ablations with the designed system is assessed by carrying out gelatin phantom, ex vivo and in vivo animal experiments. The interventional MRE system results from the combination and the adaptation of several conventional techniques and can be considered as a baseline for interventional MRE. A second part of this thesis is dedicated to the development of an innovative method of MRE data processing. The new method, namely *raw MRE method*, aims at improving the robustness of the protocol while accelerating it. The raw MRE method is based on the exploitation of raw data in order to avoid multiple data processing steps. Experiments are carried out to assess the relevance of using this method rather than the conventional MRE process.

The manuscript is divided into four chapters.

The first one outlines the context of this project. Relevant issues related to the subject are exposed in order to easily understand the objectives of the project and its underlying requirements.

The second chapter offers an overview of the current available MRE systems and describes in details the components of the proposed all-in-one interventional MRE system.

Experiments carried out to evaluate the feasibility of interventional MRE are described and discussed in the third chapter. This includes experiments on gelatin phantoms, liver samples and in vivo swine models.

The last chapter presents the alternative method proposed for MRE data processing. After detailing the underlying theory, an evaluation of the method in different cases is given in comparison with the conventional method.

Chapter 1

Context

> " *S'il n'y avait pas la science, combien d'entre nous pourraient profiter de leur cancer pendant plus de 5 ans ?*"
>
> Pierre Desproges

Contents

This section aims at presenting the context of this PhD thesis work. Cancerous tissue are increasingly treated by minimally invasive thermal ablations under imaging guidance. The different techniques of percutaneous thermal ablations are firstly introduced. Some limitations of the current approaches are provided in order to clearly describe the objective of the project.

1.1 Minimally invasive therapeutic approaches for cancer

1.1.1 Cancer: Facts and Figures

Cancer is one of the first causes of mortality worldwide. Cancer represents 12 millions of new cases in 2012 (350000 in France) and 8.2 millions of deaths (148000 in France). According to the WHO forecasts, the number of new cancer cases will increase up to 70% over the next two decades. The fight against cancer is one of the biggest economic and social issues of our century. In France, cancer cost is estimated to 11 billion of euros and the annual budget allocated to the research against cancer is estimated between 350 and 400 millions of euros. The evolution of cancer mortality over the last years in France and the distribution according to the affected organs are shown in Fig.1.1 and 1.2. Since 1989, the survival rate of cancer patients increased of 5 years thanks to the improvement of treatments. Today, radiotherapy, chemotherapy and surgical resection are the standard treatment available to the patients. According to the french national institute of cancer, 370000 cancer cases are treated by surgery every year, 270000 by chemotherapy and 170000 by radiotherapy. These treatments are exhausting and strongly impact the patient life. For many reasons, such as age, recurrence or disease extent, some patients cannot be candidate to these treatments. Many researches have focused on alternatives to the standard protocols. The development of new minimally invasive approaches that improve the patient comfort and decrease the complication rate has allowed the most fragile or vulnerable patients to be considered for treatment.

1.1.2 Thermal Ablation

During the last decades, attention has been given to the potential of thermal damages for the destruction of cancerous cells. Localized thermal ablations present the advantage of being minimally invasive, even non-invasive in the case of HIFU therapy. These techniques enable therefore the destruction of the tumor without risked and expensive surgical procedures. Localized thermal ablations offer the possibility of proposing another treatment to people who can not be candidate for surgery due to age, comorbidity or disease extent. All of the ablation methods require the application of thermal energy to the target tissue in order to destroy it. Nevertheless, these modalities present their own advantages and drawbacks, which are directly related to their physical principle. A brief overview of the thermal ablation techniques is provided in this section.

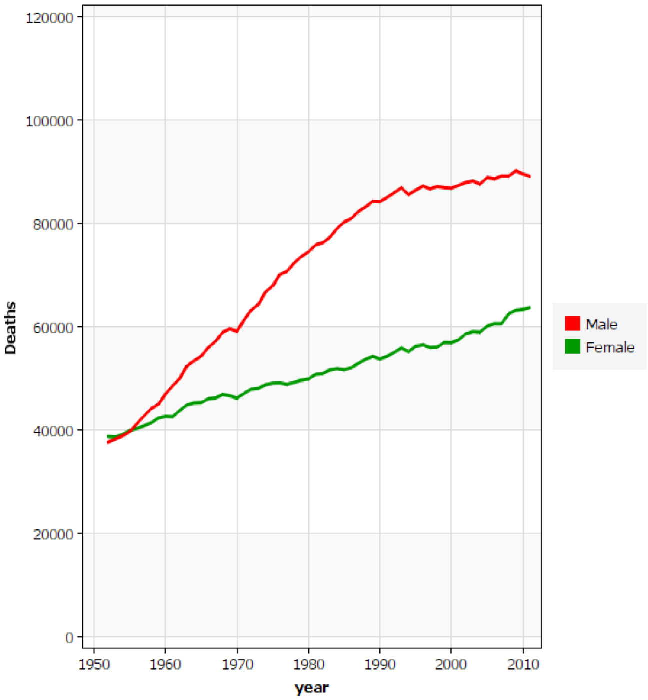

Figure 1.1 – Evolution of the number of cancer deaths in France over the last decades. From the International Agency for Research in Cancer.

Hyperthermia

Thermal tissue damage can be caused by the denaturation (shape and structure changes) of the molecules of the tissue (protein, collagen). The required energy to alter the standard configuration, which depends on the molecule type, is brought by local temperature increase, i.e. hyperthermia. Several studies have focused on the correlation between the exposure time, the temperature and the ratio of cell death in hyperthermia. Typical results show that exposing the tissue to 43°C during 60 minutes reduces the number of cells by a factor of 10 [Hildebrandt et al., 2002]. Given that a macroscopic tumor is approximately composed of 10^9 cells [Wust and Gellermann, 2007], the time required to destroy it, at the constant temperature of 43°C, is typically 10 hours. However, according to the Arrhenius equation, it has been shown that an increase of 1°C of the ablation temperature could reduce the required time by a factor of 2. For instance, at 50°C, only 10 minutes are needed to destroy the previous tumor. Fig.1.3 illustrates this phenomenon. Therefore, techniques have been developed to increase rapidly and locally the temperature up to 50°C. Increasing the temperature requires the deposit of energy. The required energy quantity in any material is described by its heat capacity. The heat capacity of a human tissue is approximately 4.2 kJ/kg/°C or 4200Ws/kg/°C, which means that a power of 1W/kg over 4200 s is required to increase the temperature of 1°C or a SAR (Specific Absorp-

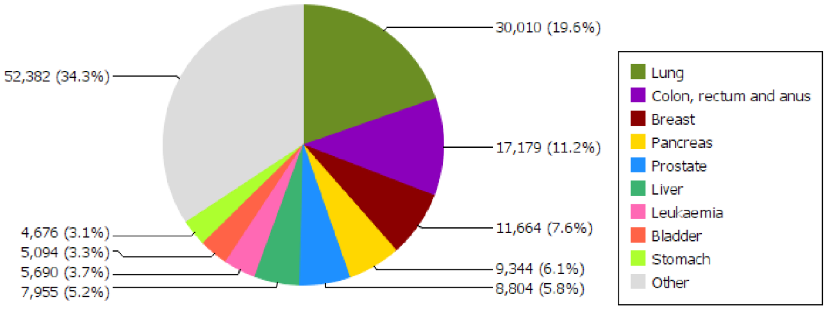

Figure 1.2 – Distribution of cancer according to the affected organ in France in 2011. From the International Agency for Research in Cancer.

tion Rate) of 70W/kg is needed to increase the temperature of 1°C in one minute. A thermal ablation consists in applying large SAR in the localized region to be destroyed. Several hyperthermia techniques emerged and are now clinically operational for a large variety of organs. Current localized thermal ablation methods (radiofrequency ablation, laser-induced thermotherapy or high intensity focused ultrasound) typically apply a SAR of 2500W/kg, which corresponds to temperature increase of 10°C/min.

- **Radiofrequency ablation (RFA)** RFA is the most investigated technology and the most used in clinical practice. RFA relies on the creation of a complete electrical circuit through the body thanks to the abundance of ionic fluid in the human body. The electrical current is generated by an RF applicator placed in the tumor region and exits the body through ground pads located on the skin of another part of the body. An RF applicator is shown in Fig.1.4. Available commercial RF systems work on frequencies between 375 and 480 kHz [Clasen and Pereira, 2008]. Application of radiofrequency current results in an increase in temperature by Joule effect around the applicator tip because of the non-negligible impedance of in vivo tissue. The final heating zone is extended to a few centimeters because of tissue thermal conduction. An alternative to monopolar RFA mode (one electrode with ground pads) is the bipolar mode which requires the insertion of a second applicator but enables to better focus the ablated region between the electrodes [Brace et al., 2011]. Depending on the objective, this method can be preferred to limit the ablated zone.

- **Microwave ablation (MWA)** Microwave ablation is a second method of thermal ablation that uses electromagnetic waves. However, MWA ablation operate at higher frequencies between 900 MHz and 2.45 GHz and the physical principle is completely different. An alternating electromagnetic field is applied on the target zone with a percutaneous applicator. Water molecules tend to align with the magnetic field and

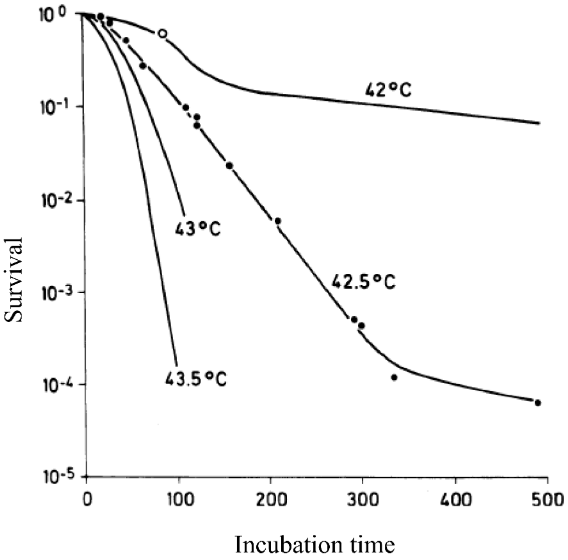

Figure 1.3 – Dose response relationship of thermal cell killing. Image from [Hildebrandt et al., 2002]

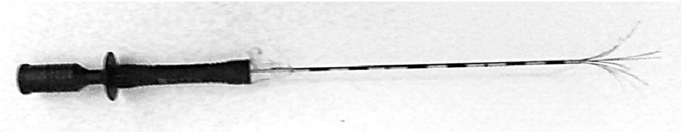

Figure 1.4 – RFA applicator (Starburst ®, Angiodynamics, NY)

hence rotate with the field [Brace, 2010]. This continuous oscillation increases kinetic energy and leads to temperature elevation. Unlike RFA, MWA can be performed on regions where electrical conductivity is null. On the other hand, the region treated by MWA is reduced to a limited area around the applicator and does not exceed 4 cm in diameter. A MWA applicator is shown in Fig.1.5.

- **Laser-induced thermotherapy (LITT)** A third clinically approved thermal ablation technique is the Laser-induced thermotherapy (LITT). LITT employs electromagnetic waves in the infrared domain. The energy of the light is delivered in the region of interest by a flexible optical fiber and is absorbed by the tissue and then converted into heat. The ideal lesions are those less than 3 cm in diameter [Gough-Palmer and Gedroyc, 2008], although the size of the ablated region depends on the optical properties of the treated tissue. Light is delivered by flexible optical fibers of 0.2-0.8 mm in diameter. Several fibers at lower power can be used to enlarge the lesion. More recently, the use of water-cooled fibers allowed using higher power while avoiding carbonization of tissue [Dick et al., 2003].

- **High Intensity Focused Ultrasound (HIFU)** Thermal ablations can be per-

Figure 1.5 – MWA applicator (Acculis ®, Angiodynamics, NY)

formed by a recent non-invasive technology that relies on the deposit of energy of ultrasound waves. Unlike other hyperthermal ablation techniques, the HIFU therapy does not use electromagnetic waves but mechanical pressure waves at frequencies around 1 MHz. By using dedicated devices that allow the generation of high intensity ultrasounds and by focusing the large beams of waves to a small spot, the intensity is greatly increased. Biological tissues absorb ultrasound, which results in an increase of temperature. The main advantage of this technique is the absence of applicator that allows a completely non-invasive ablation. The first organ treated by image-guided HIFU was the prostate in 1994 [Madersbacher et al., 1995] and numerous organs were tested after this successful ablation [Kim et al., 2008].

Cryotherapy

Unlike previously described thermal ablation techniques, tumors can also be destroyed by applying very low temperature. Cryotherapy or cryoablation also belongs to the family of thermal ablation techniques but uses extreme cold to destroy the tumor. Cryoablation became a clinically accepted tool for the treatment of numerous organs [Tatli et al., 2010]. Liquid nitrogen or argon gas is placed in contact with the tumor by using a cryoprobe. A temperature between 40°C and 20°C is obtained. Causes of cell death are different from hyperthermia. During a first freezing phase, ice crystals are formed in the extracellular space, which results in osmotic unbalance. The hypertonic environment involves the dehydration of cells resulting in their death. Then a thawing phase allows to let fluids flow from extracellular to intracellular spaces due to osmotic gradients which allows the formation of intracellular ice crystals during the second freezing phase. This phase results in membrane rupture and cell death. During the following thawing phase, ice crystals merge into bigger crystals that destroy even more cell membranes. The diameter of the iceball formed by one probe is around 2.5 cm. Several cryoprobes can be used to enlarge the ablated lesion. Cryoablation is the most suited technique for large tumors. Fig.1.6 illustrates a typical cryoablation procedure.

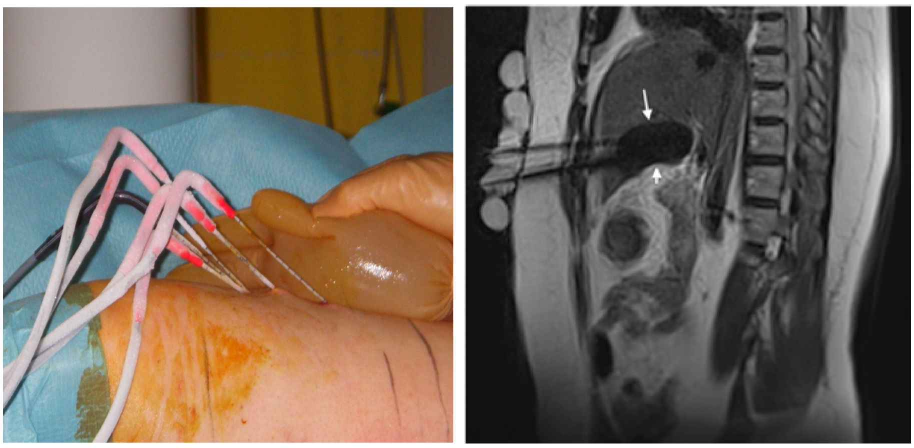

Figure 1.6 – a)Cryoablation procedure with several probes to enlarge the lesion. The hot water in the glove protects the skin from the very low temperature of the cryoprobes. b)Typical MR image of a cryoablation showing the iceball (arrows). Courtesy of Department of Interventional Radiology of the Strasbourg University Hospital.

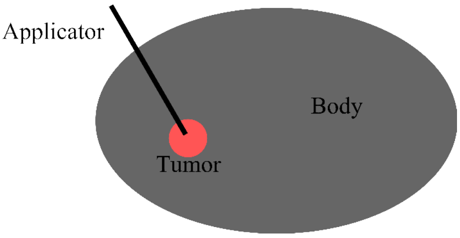

Figure 1.7 – Picture of a percutaneous thermal ablation. An applicator of RFA, LITT, cryotherapy or MWA is inserted in the patient through the skin to reach the tumor to be destroyed.

1.1.3 Image-guided percutaneous procedure

Focusing the energy during the appropriate time within the region of interest is the major requirement for the local ablation success. Interventional radiology enables to fulfill this objective by providing images of the patient's body during the procedure. Except HIFU therapies, which is totally non-invasive, all of the previously mentioned thermal ablation techniques require the insertion of an applicator through the patient skin to reach the target region. They are grouped together under the name "percutaneous thermal ablation". A percutaneous thermal ablation is schematized in Fig.1.7. A standardization of the percutaneous procedure protocol has been established [Goldberg et al., 2009] that describes 5 phases in the procedure, namely (1) planning, (2) targeting, (3) monitoring, (4) controlling and finally (5) assessing treatment response. Images are acquired in real-time and provide essential information at every steps of the procedure.

1. *Planning*
   During this step, the imaging modalities aim at determining whether patients are suitable candidates for the procedure. The decision depends on the number of tumors,

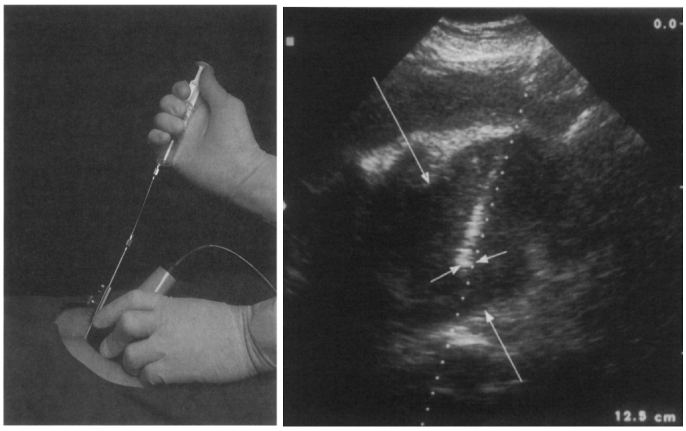

Figure 1.8 – a) Setup of an ultrasound-guided biopsy. b) Typical US image obtained during a biopsy of the caudate liver lobe (arrows). The needle tip (small arrows) is seen in the target. Images from [Holm and Skjoldbye, 1996]

their size and their location. If they are candidate, the size and the location of the region to be treated is identified.

2. *Targeting*
   The insertion point of the applicator is localized on the patient skin and the needle is inserted in the body to reach the region to be treated, under real-time imaging.

3. *Monitoring*
   The effects of the ablation must be evaluated in real-time in order to avoid damage to healthy tissue and ensure the complete destruction of the tumor.

4. *Controlling*
   The control of the ablation procedure depends on the acquired images and events that could happen. Based on monitoring, it may be necessary to stop the procedure, move the applicator and adjust ablation intensity parameters.

5. *Assessment of treatment*
   After the intervention, new images are acquired and analyzed to determine the efficiency of the procedure.

The imaging modality used during the procedure steps 2, 3 and 4 is not necessary the same as the one used for planning or controlling. The choice of imaging modality belongs to the planning step and depends on the tumor location and its visibility according to the type of image but also available equipments, patient requirements and operator preference.

- **Ultrasonography** Interventional ultrasonography (US) was the first modality commonly used to guide percutaneous procedures. Ultrasound images are acquired by sending ultrasound pulses into the investigated tissue with a compact transducer.

The echoes reflected by the tissue are recorded and displayed as an image. Typical setup and image of a biopsy guided by ultrasound are shown in Fig.1.8. This technique provides a real-time guidance. The equipment is mobile, non-expensive, non-ionizing and non-bulky. These advantages allowed the development of image-guided thermal ablations very quickly. In 1996, [Holm and Skjoldbye, 1996] have already published a review about ultrasound guided procedures and have listed successful thermal ablations guided by ultrasound. In 1993, a first laser ablation on liver metastasis guided by ultrasonography was proposed by [Nolsøe et al., 1993]. The same year, a radiofrequency ablation guided by ultrasonography was reported [Rossi et al., 1993]. In 1994, this modality was used to guide a microwave ablation of a liver tumor [Seki et al., 1994]. The first percutaneous procedure of cryoablation was performed on renal tumor in 1995 [Uchida et al., 1995]. The procedure is controlled by examining the size of the hyperechoic area, which indicates complete necrosis. However, edema, increasing acoustic attenuation of necrotic tissue and the heterogenetity of the lesion [Li and Wu, 2013], may prevent clear visualization of the necrotic area.

- **X-Ray imaging** Many percutaneous procedures are also performed under X-ray imaging. Computed Tomography (CT) scanner offers a good visualization and precision in three dimensions. Recently, technical advances (CT fluoroscopy) in reconstruction algorithms have allowed for real-time display of CT images (6 images per second) [Silverman et al., 1999]. However, patients and radiologists are exposed to ionizing X-ray radiation during the procedure, which is the main drawback of this modality.

- **Magnetic Resonance Imaging** Magnetic resonance imaging (MRI) provides a rich contrast in soft-tissue and enables the acquisition of any slice position and orientation. 3D acquisition and real-time imaging are possible. These characteristics make this non-ionizing modality very useful for thermal ablation guidance. MRI is the only one imaging modality that can provide a temperature map at higher temperature than 60 $°C$ in real-time by MR-thermometry, which is particularly helpful for the monitoring of thermal ablations [Quesson et al., 2000]. Although MRI guidance is particularly well adapted to thermal ablation monitoring, the number of interventions remains low due to high operational costs including the cost of specific MR-compatible devices. Since microwave and radiofrequency ablation may be source of noise in MR-images, advanced MR-compatible technologies are required. Simple custom-made notch filters are sufficient to obtain in real-time a good quality image for microwave ablations [Morikawa et al., 2002] but a more complex hardware design of the radiofrequency device is required to remove this noise [Zhang et al., 1998]. AngioDynamics (Queensbury, NY) is commercially well implemented on the market of MR-compatible RFA devices. Laser thermal ablation devices do not require any spe-

Figure 1.9 – Percutaneous thermal ablation performed under MRI guidance. Courtesy of Department of Interventional Radiology of the Strasbourg University Hospital.

cific changes to be MR compatible. Several commercial devices are available. More recently, non-invasive MR-guided HIFU therapy were allowed: FDA approved the treatment of uterine fibroids in 2004 and palliative treatment of bone metastases in 2012 [Schlesinger et al., 2013] with several devices commercialized by Insightec Ltd (Tirat Hacarmel, Israel) and Philips Healthcare (Amsterdam, Holland). MR-guided cryotherapies [Morrison et al., 2008] also emerged in clinical practice. The contrast between organs and ice-ball is extremely strong because the ice-ball results in a signal void in MR images (Fig.1.6b). Hence the ice-ball growth is easily evaluated on MR-images which allows to control accurately the procedure. MR-thermometry is not used in this case because of the lack of signal, but this contrast is sufficient and is even proved to be more efficient than ultrasound and CT contrast [Tacke et al., 1999]. Only one MR-compatible cryotherapy system is commercially available (Galil Medical, Yokneam, Israel).

Given the great potential of interventional MRI (iMRI), this project focuses on the percutaneous thermal ablations performed under MRI-guidance and aims at improving their monitoring and their control in order to increase their success rate.

1.2 From diagnostic MRI to interventional MRI

1.2.1 Nuclear magnetic resonance signal

In 1952, Felix Bloch and Edward Purcell won the Nobel prize in physics for their discovery of nuclear magnetic resonance. From water and paraffin samples, they measured for the first time the precessional signal of spins around a magnetic field. Three decades later, Lauterbur acquired the first MR image. The enthusiasm of universities for this new phe-

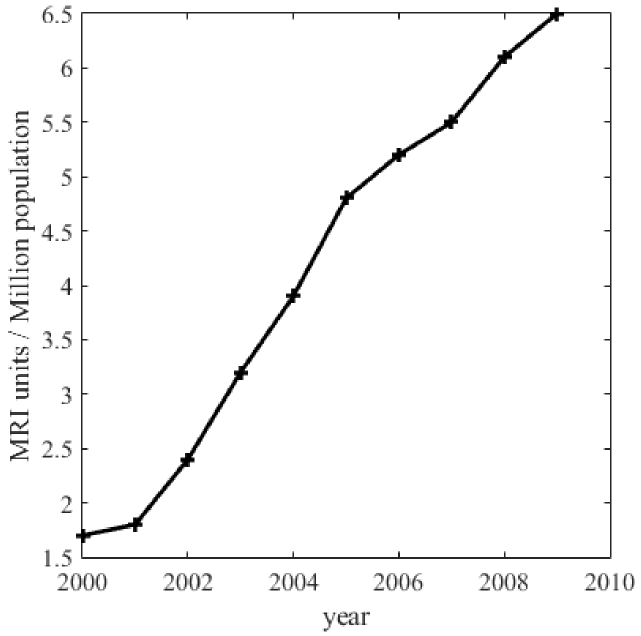

Figure 1.10 – Evolution of the number of MRI units in France during the last decade. Graph built from data of the Organization for Economic Co-operation and Development (OECD) Health Data 2011

nomenon allowed to improve the technique until the industry found its own interest and developed a commercial system for hospitals in the 1980's. In 1990, 800 MRI units were installed worldwide. Twenty years later, around 5000 MRI scanners were clinically available (from the Organization for Economic Co-operation and Development (OECD) Health Data 2011). The evolution of the number of MRI units in France is plotted in Fig.1.10. MRI relies on the interaction of atomic nuclei with an external magnetic field. Since the human body consists in 70% of water (H2O), the dominant nucleus investigated in MRI is the proton of the hydrogen. Every atomic nucleus has an intrinsic angular momentum $\vec{J}$ called *spin*, which arises from the coupling of neutrons and protons of the nucleus. A nuclear magnetic moment $\vec{\mu}$ is associated to each nucleus according to the following expression:

$$\vec{\mu} = \gamma \vec{J} \tag{1.1}$$

with γ being the gyromagnetic ratio that depends on the investigated nucleus. The gyromagnetic ratio of the hydrogen atom is $2.675.10^8$ rad/s/T. If we consider a nuclear spin in a static magnetic field $\vec{B_0}$, this spin is submitted to a moment $\vec{N}$ that tends to align it to the magnetic field:

$$\vec{N} = \vec{\mu} \wedge \vec{B_0} \tag{1.2}$$

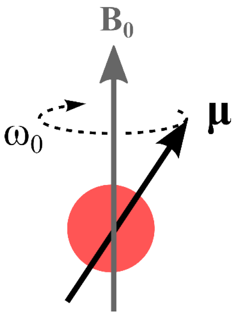

Figure 1.11 – Illustration of the precession motion around the external magnetic field axis at the Larmor frequency.

However, this alignment is not similar to the compass needle that aligns with a magnet. The comparison with a spinning-top is more relevant because all the nuclear magnetic moments rotate around the static magnetic field axis as demonstrated by the following equations. According to fundamental equations from classical mechanics, the variation of the angular momentum is described by:

$$\frac{d\vec{J}}{dt} = \vec{N} \tag{1.3}$$

Equations (1.2) and (1.3) result in the fundamental differential equation that governs the movement of spins in a magnetic field:

$$\frac{d\vec{\mu}}{dt} = \gamma\vec{\mu} \wedge \vec{B_0} \tag{1.4}$$

Assuming the static magnetic field $\vec{B_0}$ along the direction $\vec{z}$ in the reference frame, the previous equation can be decomposed over the three directions as follows:

$$\begin{aligned} \frac{d(\mu)_x}{dt} &= \gamma B_0(\mu)_y \\ \frac{d(\mu)_y}{dt} &= \quad \gamma B_0(\mu)_x \\ \frac{d(\mu)_z}{dt} &= 0 \end{aligned} \tag{1.5}$$

Previous equations clearly describe the precession of the spin around the magnetic field in the clockwise direction (when $\gamma > 0$) at the angular speed $\omega_0 = \gamma B_0$ commonly referred to as the Larmor frequency. Fig.1.11 illustrates this phenomenon of precession. In MRI, not only a spin but a set of spins included in a small volume V called *voxel* is investigated. The local magnetic moment per unit volume is then introduced:

$$\vec{M} = \frac{1}{V} \sum_{protons\ i\ in\ V} \vec{\mu_i} \tag{1.6}$$

By summing Eq.(1.4) over the individual spins of the voxel and neglecting in a first time proton interactions with their environment, the differential equation of the magnetization is obtained.

$$\frac{d\vec{M}}{dt} = \gamma\vec{M} \wedge \vec{B_0} \tag{1.7}$$

The magnetization vector is commonly expressed in terms of two components, the first one is along the magnetic field axis ($\vec{z}$ arbitrarily) and the other one is orthogonal to it.

$$\begin{aligned} \frac{d\vec{M_z}}{dt} &= 0 \\ \frac{d\vec{M_{xy}}}{dt} &= \gamma\vec{M_{xy}} \wedge \vec{B_0} \end{aligned} \tag{1.8}$$

However the assumption of non-interaction of protons with their surroundings is not realistic and nuclear magnetic moments are not only precessing around the magnetic field axis but also tend to align to it so that an equilibrium value of the magnetization vector is reached. Given that the potential energy of the system is $U = \quad \vec{M}.\vec{B_0} = \quad M_zB_0 = M_0$, the minimum is reached when the magnetization and the magnetic field are aligned, $M_{xy} = 0$. Although MRI relies on the study of the magnetization vector, $\vec{M}$ can not be measured in its equilibrium state because its amplitude is too weak compared to the amplitude of the static magnetic field. Receiving antenna can only measure the transverse magnetization orthogonal to the main B_0 axis.

Nuclear magnetic resonance relies on disturbing this equilibrium state and observing the return to equilibrium. The disturbance is provided by a radiofrequency (RF) pulse that is an external magnetic field $\vec{B_1}$ oscillating at the Larmor frequency and applied during a short period of time τ. When the RF pulse is turned off, the magnetization vector has been flipped around the $\vec{B_1}$ axis with an angle θ, called the *flip angle*. The effect of the RF pulse allows the magnetization vector to flip out of the static magnetic field and induce a voltage in the receiving antenna. More details are available in [Brown et al., 2014].

After being disturbed by the RF pulse, M_z tends to recover its equilibrium value M_0 and M_{xy} tends to vanish (Fig.1.12). Two relaxation terms T_1 and T_2 are therefore added to Eq.1.8 in order to take into account the interactions of protons with their surroundings. These terms express the relaxation phenomenon of both components involved in the recovery of their equilibrium value. It has been empirically shown that the relaxation of M_z is proportional to the difference $M_0 \quad M_z$:

$$\frac{dM_z}{dt} = \frac{1}{T_1}(M_0 \quad M_z) \tag{1.9}$$

where T_1 is the *spin-lattice relaxation time*. By solving this equation, the evolution of the longitudinal magnetization after an RF pulse can be described by:

$$M_z(t) = M_z(0)e^{\quad t/T_1} + M_0(1 \quad e^{\quad t/T_1}) \tag{1.10}$$

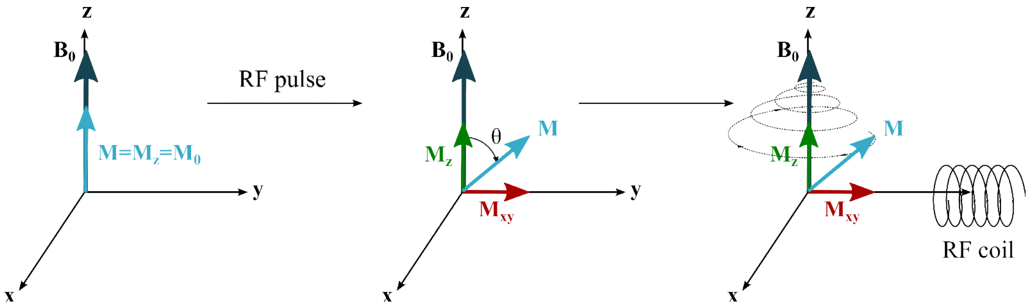

Figure 1.12 – The magnetization vector is flipped out of the static magnetic field with an angle θ thanks to RF pulse. Then, the magnetization vector tends to recover its equilibrium value corresponding to the minimum of energy. The transverse magnetization induces a voltage in the receiving antenna.

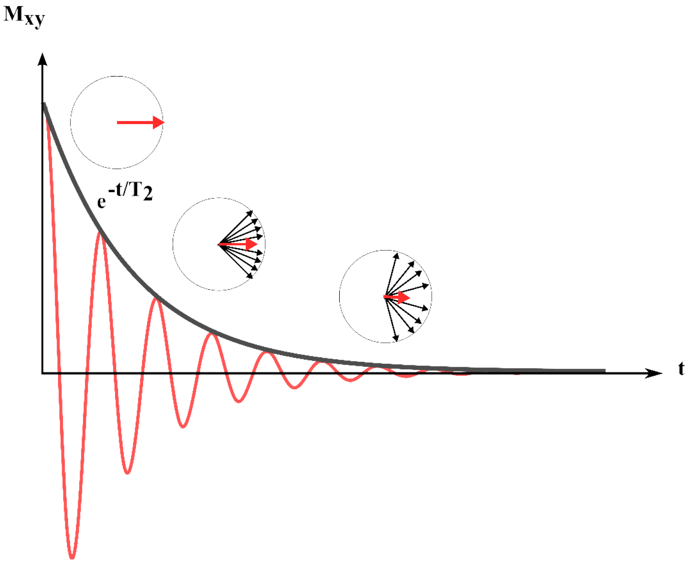

Figure 1.13 – T_2-relaxation of the magnetization vector. Spins are dephased due to small local variation of the magnetic field, which leads to the decrease of the net transverse magnetization

Regarding the relaxation of the transverse component M_{xy}, another mechanism is involved: the small local variation of the magnetic field due to the interaction between the external field and the field of the neighbors results in a variation of precessional frequencies of different spins included in the voxel. As a result, spins are dephased, which leads to the decrease of the net transverse magnetization (Fig.1.13). In order to take into account this spin-spin interaction, a term is added to the transverse component of Eq.(1.8):

$$\frac{d\vec{M}_{xy}}{dt} = \gamma \vec{M}_{xy} \wedge \vec{B}_0 \quad \frac{1}{T_2}(M_{xy}) \tag{1.11}$$

where T_2 is the *spin-spin relaxation time*. This additional term leads to an exponential decay of the transverse magnetization amplitude.

$$M_{xy}(t) = M_{xy}(0)e^{\ t/T_2} \tag{1.12}$$

The combination of the differential equations of both components of the magnetization, Eq.(1.9) and Eq.(1.11), enables to establish the phenomenological *Bloch equation*:

$$\frac{d\vec{M}}{dt} = \gamma\vec{M} \wedge \vec{B_0} + \frac{1}{T_1}(M_0 \quad M_z) \quad \frac{1}{T_2}(M_{xy}) \tag{1.13}$$

and its decomposition over the three directions:

$$\begin{array}{rcl} \frac{dM_x}{dt} & = & \omega_0 M_y \quad \frac{M_x}{T_2} \\ \frac{dM_y}{dt} & = & \quad \omega_0 M_x \quad \frac{M_y}{T_2} \\ \frac{dM_z}{dt} & = & \frac{1}{T_1}(M_0 \quad M_z) \end{array} \tag{1.14}$$

The resolution of these equations provides a complete set of solutions:

$$\begin{array}{rcl} M_x(t) & = & e^{\ t/T_2}(M_x(0)cos(\omega_0 t) + M_y(0)sin(\omega_0 t)) \\ M_y(t) & = & e^{\ t/T_2}(M_y(0)cos(\omega_0 t) \quad M_x(0)sin(\omega_0 t)) \\ M_z(t) & = & M_z(0)e^{\ t/T_1} + M_0(1 \quad e^{\ t/T_1}) \end{array} \tag{1.15}$$

The use of a complex notation for the transverse magnetization is helpful for clarity. Let us note $M_\perp(t) = M_x(t) + iM_y(t)$. Eq.(1.15) reduces to:

$$\begin{array}{rcl} M_\perp(t) & = & e^{\ t/T_2}e^{\ i\omega_0 t}M_\perp(0) \\ M_z(t) & = & M_z(0)e^{\ t/T_1} + M_0(1 \quad e^{\ t/T_1}) \end{array} \tag{1.16}$$

with $M_\perp(0) = |M_\perp(0)|e^{i\phi_0}$ being defined as the transverse magnetization in the rotating frame just after the RF pulse. Let us notice that its magnitude and its phase depend on the RF pulse characteristics.

Without going into too much details, in practice, another mechanism is implied in the transverse magnetization relaxation: the inhomogeneities of the external field which increase the phase shift between individual spins. In order to consider this phenomenon, the relaxation time T_2 is replaced by T_2^* according to the following expression: $\frac{1}{T_2^*} = \frac{1}{T_2} + \frac{1}{T_2'}$ with T_2' representing this additional decay time due to the inhomogeneities of the magnetic field.

The whole field of MRI relies on this set of solutions. Given that the relaxation times and the magnetization amplitude are tissue dependant, MRI consists in distinguishing different tissues through these parameters.

1.2.2 MR-image formation

As previously explained, the observed MR signal is a temporal one-dimensional signal. The challenge behind MRI is to create from this signal a map of the investigated tissues as a function of their magnetic resonance characteristics. The following section aims at describing the formation of MR-images.

In order to simplify the demonstration, T_2 relaxation is neglected. Now, let us consider a theoretical 1D object subjected to a magnetic field $\vec{B_0} = B_0\vec{z}$. An RF pulse is applied for a given short time period and turned off. The temporal signal S measured from the transversal magnetization vectors of each voxel of coordinates x is described by the following expression:

$$S(t) = \int M_{\perp}(x,0)e^{\ i\gamma B_0 t}dx \tag{1.17}$$

The objective is to individually identify the transverse magnetization of each voxel. The key is to apply a magnetic field gradient G_{RO}, called *read-out gradient*, in such a way that the voxels are subjected to a different magnetic field amplitude as a function of their position along $\vec{x}$: $B(x) = B_0 + G_{RO}x$. The general principle of a magnetic field gradient is described in Fig.1.14. During the application of the magnetic field gradient, the precession frequency of the magnetization vectors depends on their location. When the gradient is turned off, they recover their initial angular frequency but have accumulated a different phase. In the current case, the impact of the magnetic field gradient during its application is exploited. Eq.(1.17) becomes:

$$\begin{aligned} S(t) &= \int M_{\perp}(x,0)e^{\ i\gamma(B_0+G_{RO}x)t}dx \\ &= e^{\ i\omega_0 t}\int M_{\perp}(x,0)e^{\ i\gamma G_{RO}xt}dx \end{aligned} \tag{1.18}$$

In practice, the received signal is demodulated at the demodulating frequency ω_0. The resulting signal is given by:

$$S(t) = \int M_{\perp}(x,0)e^{\ i\gamma G_{RO}xt}dx \tag{1.19}$$

Let us introduce the variable $k_x = \frac{\gamma}{2\pi}G_{RO}t$. The previous Eq.(1.19) reduces to:

$$F(k_x) = S(t) = \int M_{\perp}(x,0)e^{\ i2\pi k_x x}dx \tag{1.20}$$

The previous equation makes a Fourier transform expression appear. By applying an inverse Fourier transform, the transverse magnetization $M_{\perp}(x,0)$ can be recovered. To summarize it, the spatial frequency domain (called k-space) of the signal is acquired before reconstructing the spatial domain.

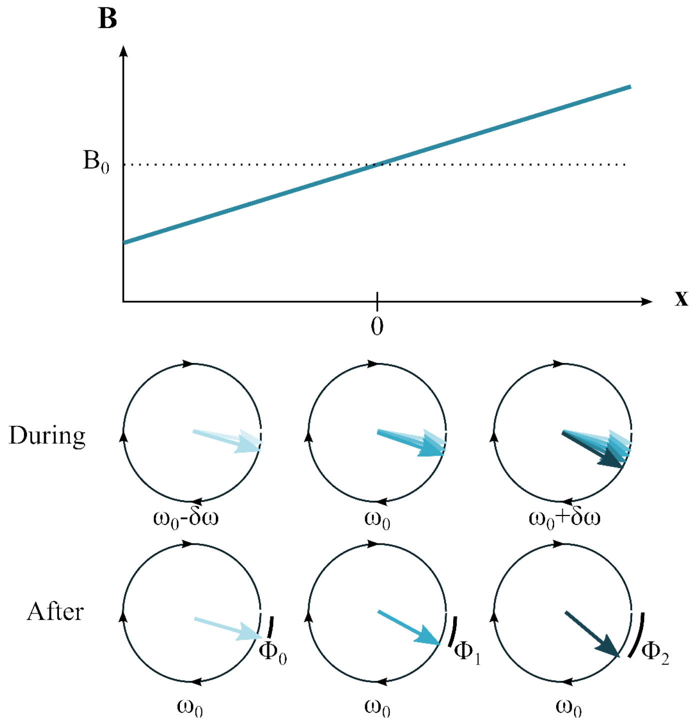

Figure 1.14 – Magnetic field gradient. During the application of a linear magnetic field gradient, the magnetization vector of each voxel precesses with a different angular frequency according to its location along the gradient axis. When the gradient is turned off, all the magnetization vectors turn with the same angular frequency but they have accumulated different phases according to their location.

It is now easy to extend the method to 2D images. Let us consider a theoretical infinite 2D object. The lines of the k-space are acquired in accordance with the previous 1D description. This method is repeated as many times as the number of k-space lines. Each line acquisition is differentiated by a second gradient G_{PE}, called *phase encoding gradient*, which value changes with each line acquisition l. This gradient is applied for a time T between the RF pulse and the signal acquisition. Spins are subjected to a different magnetic field which results in a controlled dephasing at the end of the gradient. They accumulate a delay ϕ due to their different precession frequencies during the application of the magnetic field gradient. As a result, the acquired demodulated signal is :

$$S(t,l) = \iint M_{\perp}(x,y,0)e^{\ 2i\pi(\gamma G_{RO}xt+\phi(l,y))} \tag{1.21}$$

with $\phi(l,y)$ being defined by:

$$\phi(l,y) = \gamma \int_0^T G_{PE}(l)ydt = \gamma G_{PE}(l)yT \tag{1.22}$$

By inserting the expression Eq.(1.22) in Eq.(1.21), the acquired demodulated raw MR signal is given by:

$$S(t,l) = \iint M_\perp(x,y,0)e^{\ 2i\pi(\gamma G_{RO}xt+\gamma G_{PE}(l)yT)}dxdy \tag{1.23}$$

In the same manner as previously, the variable k_y is introduced in accordance to: $k_y = \frac{\gamma}{2\pi}G_{PE}(l)T$ in order to describe the signal by the following expression:

$$F(k_x,k_y) = \iint M_\perp(x,y,0)e^{\ i2\pi(k_x x+k_y y)}dxdy \tag{1.24}$$

The application of a 2D inverse Fourier transform to Eq.(1.24) makes possible the recovery of the complex quantity $M_\perp$ for each voxel.

$$M_\perp(x,y) = \iint F(k_x,k_y)e^{i2\pi(k_x x+k_y y)}dk_x dk_y \tag{1.25}$$

The nature of the acquired signal is fundamental to understand the mechanisms of MRI. The k-space of the image is firstly acquired. Each line of the image in the k-space is acquired separately by receiving the signal of the transverse magnetization flipped after an RF pulse. Two magnetic field gradients, namely the phase encoding and the readout gradients, are required to cover the k-space in the two dimensions. Only after processing data, the image in the spatial domain can be reconstructed. Without going into further details, a third gradient is required to select only one slice in the third direction. This gradient is played out during the RF pulse, in this example along $\vec{z}$. According to the resonance condition, only spins that precess at the same frequency as the RF pulse are flipped to the transverse plane. These selected spins are included in a slice perpendicular to the gradient direction. Only these spins can provide the MRI signal because only their magnetization has a transverse component.

It must be emphasized that the previous demonstration is simplified. The integration in Eq.(1.25) requires a complete coverage of the k-space. Given that $k_x = \dfrac{\gamma}{2\pi}G_x t$, the ideal k-space coverage would be achieved only if the signal is measured continuously over a very long time. Actually, the signal is sampled over a finite time. and relaxation effects that were neglected in the previous demonstration prevent to acquire a signal over a long period. As a consequence, additional mathematical phenomena arise from the use of a discrete Fourier Transform. Inevitably, a truncated data set causes a blurring effect that can be minimized by using a large field of view to cover a larger frequency domain. Particular care should be paid to the sampling frequency: the resolution of the image depends on this sampling frequency and the *Nyquist sampling condition* must be fulfilled to avoid aliasing in the image.

Let us notice that the observed quantity $M_\perp$ is complex (Fig.1.15). The amplitude of the complex signal contains the main information such as spin density, T_1 and T_2 effects.

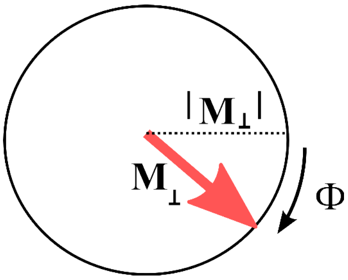

Figure 1.15 – Phase and amplitude of the transverse magnetization

Nevertheless, a particular attention will be paid to the phase of this signal in this project.

1.2.3 MR-pulse sequence design

The completion of the project summarized in this document has involved programming MR-pulse sequences. An MR-pulse sequence is a succession of events that are intended to acquire an image. The sequence contains all the characteristics of RF pulses and magnetic field gradients such as the amplitude, the shape, the start time and the duration. A sequence is schematized by a chronogram composed of several lines. In the simplest chronogram, one line is dedicated to the RF pulse events, three lines describe the events related to the magnetic field gradients in the three directions. For this project, MR pulse sequences were implemented in C++ language in the Siemens IDEA environment.
Most of the sequences arise from two basic sequences: *the gradient echo sequence* and *the spin echo sequence.*

- **Gradient echo sequence** As previously explained, a line of the image in the k-space is acquired by sampling the received signal of the transverse magnetization obtained after an RF pulse along one direction of the rotating frame. In order to fill both the negative and positive parts of the k-space, one of the methods is the use of a gradient echo sequence. First, spins are dephased using a preparation gradient applied during T in the read-out direction without acquiring any signal. Then, a second gradient with opposite polarity and twice its surface area is applied while acquiring the signal. In the middle of the second gradient, the dephasing effect of the gradient is canceled. This is commonly called a gradient echo. At this time, the first negative part of the k-space is filled, the second part is completed at the end of the readout gradient. The duration between the centers of the RF pulse and the echo is called the *echo time*(TE). The longer the TE is, the more the effect of T_2^* relaxation will affect the signal amplitude. By adequately adjusting this timing, it is possible to obtain a contrast between different tissues that do not have the same T_2^* properties. This pattern is reproduced as many times as there are lines in the

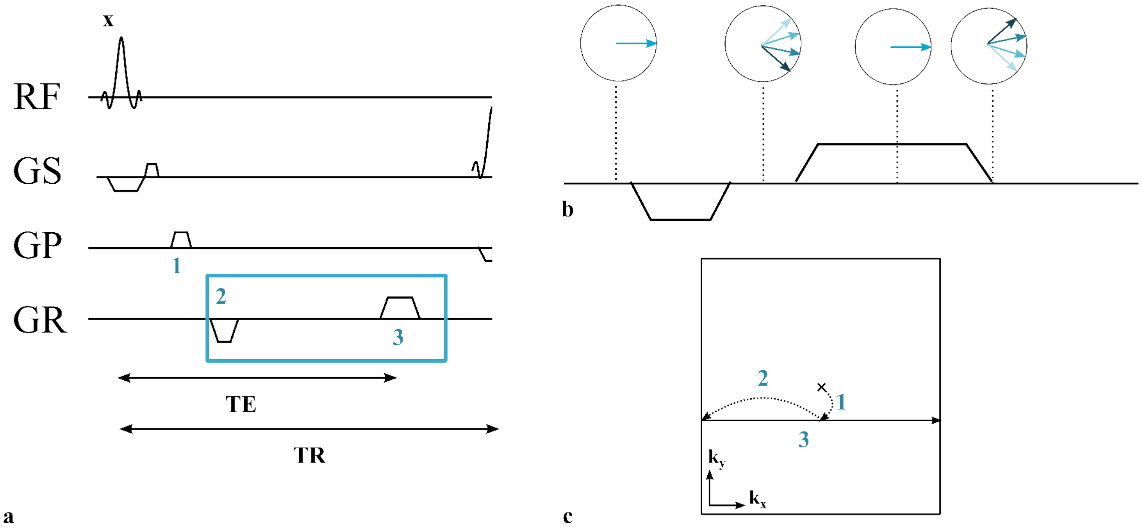

Figure 1.16 – a)Chronogram of a gradient echo sequence. The first line represents RF pulse events. The others lines include all events associated to the gradients in the three directions: slice selection (GS), phase encoding (GP) and read-out (GR) directions. The events included in the blue square are explained in (b) in terms of magnetization vector dephasing and refocusing. Only the dephasing due to magnetic field gradients is represented. The numerated events are explained in (c) in terms of trajectory k-space.

k-space. The duration between two RF pulses is called the *repetition time* (TR). The chronogram of a basic gradient echo sequence is shown in Fig.1.16. A contrast can also be obtained as a function of the parameter T_1 of each tissue by correctly choosing the repetition value, the flip angle and the echo time.

- **Spin echo sequence** The gradient echo sequence is sensitive to gradient field inhomogeneities, only the T_2^* decay can therefore be observed. On the contrary, spin echo sequences allow to obtain T_2-weighted images by compensating the magnetic field inhomogeneities. The solution involves the application of a second RF pulse of 180° at the middle of the echo time. The same preparation gradients as the gradient-echo sequence are used to spatially dephase the magnetization vectors. However, inhomogeneities of the magnetic field cause a supplementary dephasing. This dephasing is not compensated with gradient-echo sequences. By applying an RF pulse of 180° at time TE/2, the accumulated phase is inverted without changing the rotation speed. An echo is created at TE thanks to the rephasing gradients. At this time, the effects of the magnetic field inhomogeneities are also canceled. The spin-echo sequence allows the study of spin-spin interactions without the bias of static field inhomogeneities. In return, the acquisition time of a spin echo sequence is necessarily extended. The chronogram of a basic spin echo sequence is shown in Fig.1.17.

The context of this project is interventional MRI, which requires a sufficient frame rate to update spatial information as fast as possible. Due to this time constraint, fast gradient

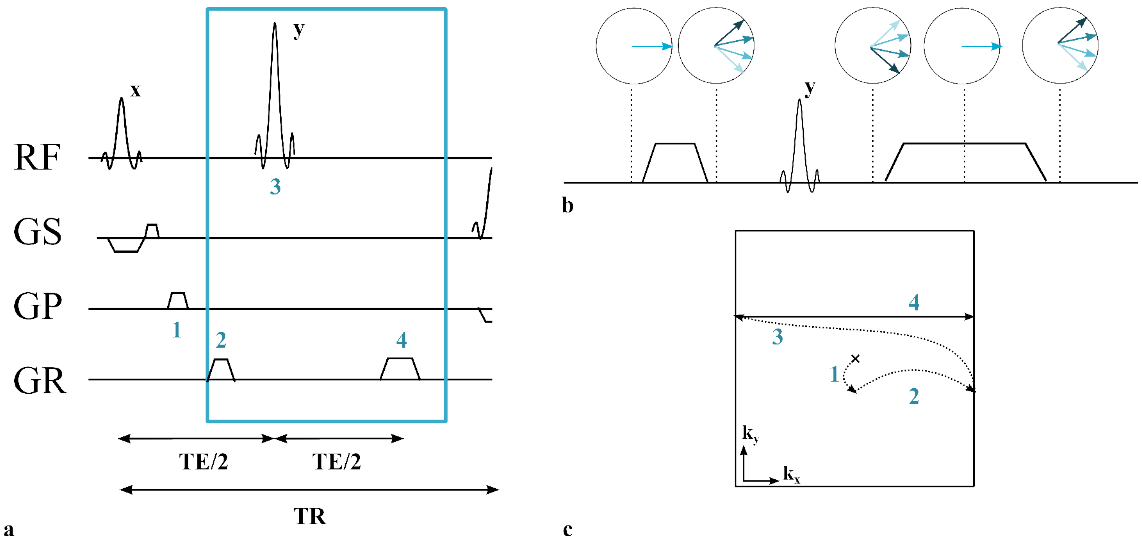

Figure 1.17 – Chronogram of a spin echo sequence. A second pulse of 180°along y is added to refocus the magnetization vectors. The events included in the blue square are explained in (b) in terms of magnetization vectors dephasing and refocusing. Only the dephasing due to magnetic field gradients is represented. The numerated events are explained in (c) in terms of trajectory k-space.

echo sequences have been preferred in this project.

1.2.4 Acceleration methods

Although the weakness of MRI compared to other imaging modalities is its acquisition speed, many improvements have been proposed. Short acquisition time is an essential point in interventional radiology. Physicians need to visualize the needle and the tissue in real-time, which requires a high update rate. MRI acceleration methods can be divided in two main groups. Given that the image is conventionally acquired line by line in the k-space, increasing the image acquisition speed means either optimizing the k-space filling or reducing the acquisition time for each k-space line. An overview of the main refinements is available in the two following paragraphs.

k-space filling optimization

Many research groups focused on optimizing the k-space filling to reduce the total acquisition time.

The first idea consists in acquiring incomplete data of the k-space by taking advantage of the redundancy properties for the complete reconstruction. As mathematically proven, the Fourier transform of a purely real quantity has an hermitian symmetry. The measured quantity in MRI is the transverse magnetization which is a complex quantity. Nevertheless, the phase of the signal is theoretically constant and can be defined as zero in a specific frame. In this case, the measured signal is considered to be real and therefore its representation in the k-space is hermitian. The technique that is called *Partial Fourier acquisition* uses this property by acquiring only the half or a bit more of the k-space and reconstructing the other part by symmetry. This technique allows the reduction of the acquisition time by a maximum factor of 2. Nevertheless, it is important to highlight that this technique assumes a purely real acquired signal. In practice, unwanted phase shifts resulting from motion, resonance frequency offsets or RF pulse inhomogeneities imply the measurement of a complex quantity. Methods were developed in this case to reconstruct a phase-corrected image by removing the imaginary part. This method requires the acquisition of more than half of the k-space. The part which is symmetrically sampled is used to approximate the imaginary part and remove it from the reconstructed image. More details are provided in the Handbook of MRI pulse sequence [Bernstein et al., 2004]. Nevertheless, information included in the phase is not always undesired. Temperature or motion information of interest can be encoded in the phase. In this case, partial Fourier acquisition is not the most recommended method.

The temporal redundancy of the information acquired in the k-space can also be exploited. The view-sharing methods are based on the reuse of previously acquired data in the k-space to reconstruct the latest image. The first method is the MR fluoroscopy that provides one image every time a new line is acquired. The keyhole technique acquires the complete k-space only once. Given that the dynamic information of interest, i.e. the contrast, comes from low spatial frequencies, only data of the k-space center is refreshed, the rest comes from the initially acquired dataset. Numerous methods, listed in this review [Tsao and Kozerke, 2012], are based on these two principles of spatial and temporal redundancies. Some studies have focused on the adaptation of these methods to interventional MRI [Duerk et al., 1996, Busch et al., 1998].

The optimization of the acquisition scheme of the k-space is another alternative to avoid missing significant information while saving time. The center of the k-space requires high sampling while the outer part can be sparsely sampled. Radial k-space filling can therefore be performed in order to gain time. Spiral k-space filling is also possible by combining it with echo-planar imaging. Fig.1.18 illustrates the three main manners of filling the k-space, i.e. cartesian, radial and spiral.

The last technique, namely parallel imaging, emerged with the development of multi-element coils. The k-space is acquired by N independant coils at the same time. It is then possible to reconstruct an image with N times more lines than the individual k-spaces, which allows saving time. The fusion algorithm may be applied before (GRAPPA) or after (SENSE) the Fourier transform required to obtain an image in the spatial domain. A review paper details all the parallel imaging techniques [Deshmane et al., 2012].

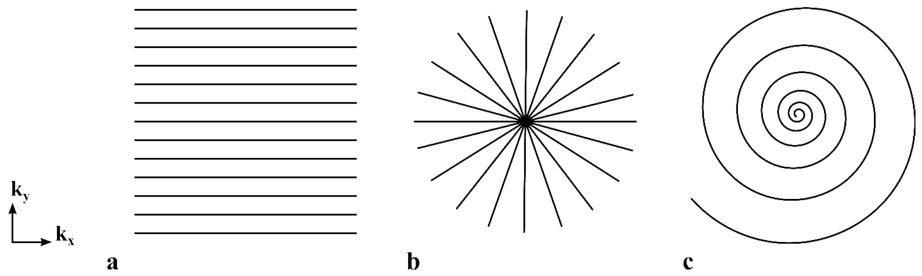

Figure 1.18 – Three examples of k-space filling schemes. a) Cartesian, b) radial and c) spiral k-space filling.

Reduction of the acquisition time of each line

Instead of reducing the number of acquired lines, one alternative is to accelerate the acquisition of each line. Unlike previous methods that were related to mathematical concepts and post-processing techniques, these ones involve refinements in terms of MR-pulse sequence design. The objective is to reduce the repetition time. However, the longer the TR is, the higher the acquired signal is because the longitudinal magnetization recovers its equilibrium value and can be flipped again by the next RF pulse. In this section, short-TR imaging is studied. The spin system is repeatedly disturbed by a repetition of RF pulses, with TR being inferior to T_1 and even T_2. In this last case, some tricks are needed to deal with the residual transverse magnetization. Two approaches are possible: either removing the remaining transverse magnetization or recycling it for the next acquisition. In both approaches, the longitudinal magnetization just before each RF pulse reaches a steady-state value after a finite number of pulses. Therefore, these MR-pulse sequences are called Steady-State Incoherent (SSI) and Steady-State Coherent (SSC) sequences:

- SSI sequences contain RF spoilers and/or gradient spoilers to make incoherent the residual transverse magnetization and therefore destroy it. RF spoilers consist in varying phase of successive RF pulses according to a predetermined schedule. Because of their different phases, the combination of the residual transverse magnetizations to the signal approaches zero. Gradient spoilers consist in dramatically dephasing spins by a supplementary gradient added between two RF pulses. The resulting incoherence yields a close to null transverse magnetization just before the next RF pulse.

- SSC sequences require balanced gradients in order to refocus the transverse magnetization and reuse it for the next cycle.

A particular interest will be taken to SSI sequences in this PhD thesis work.
An alternative to short-TR imaging is to increase the number of acquired lines per TR. The acquisition of several lines with only one excitation pulse is possible thanks to echo planar imaging (EPI). After a single RF pulse, an oscillating gradient in the read-out

Figure 1.19 – Interventional procedure in a large-bore 1.5T MRI scanner. Department of Interventional Radiology of the University Hospital of Strasbourg.

direction and short gradient pulses in phase encoding direction are applied during the magnetization decay. In the single-shot case, the full k-space is acquired with only one RF pulse excitation in 100 msec approximately. However, the SNR is generally affected due to a very wide frequency bandwidth. Besides, distortions occur in the reconstructed images because of the high sensitivity to field inhomogeneities during the long readout. This phenomenon gets worse in the air-tissue interfaces and the region close to the device required for interventional MRI. In order to reduce these distortions, several RF pulses can be used with a partial acquisition of the k-space acquired for each pulse. A refocusing 180° RF pulse can be added before the acquisition to create a T2-weighted spin echo at the cost of a longer acquisition time (EPI-SE). The fast spin echo sequence is more appreciated by interventional radiologists when the contrast brought by steady-state sequences does not allow to localize the target tissue accurately [Yutzy and Duerk, 2008]. Several 180° refocusing pulses are implemented for one RF pulse excitation. At each refocusing pulse, the phase-encoding gradient increases to encode a new line. This design allows for a better T_2 contrast.

1.2.5 Adapted MRI machine, devices and interface

Interventional MRI (iMRI) is associated with requirements in terms of acceleration of pulse sequences but also with the development of imaging systems, MR-compatible surgery tools, post-processing software and user-friendly interfaces. Several dedicated systems have been proposed by MR system manufacturers. The iMRI scanner available for this project is a large bore 1.5 Tesla (T) MRI scanner (MAGNETOM Aera, Siemens, Germany). The wide bore allows the radiologist to insert the arms and perform the procedure with more comfort and visibility in the scanner. A typical scene of an interventional procedure is shown in Fig.1.19. The emergence of interventional MRI encouraged manufacturers to develop interactive user interface. Interactive sequences allow the operator to change

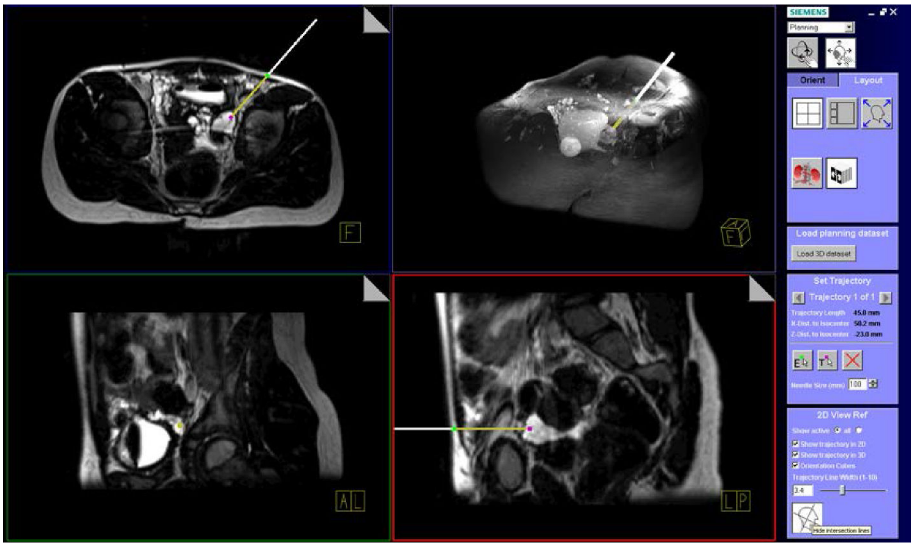

Trajectory Length 45.0 mm
X-Dist. to Isocenter 50.2 mm
Z-Dist. to Isocenter -23.0 mm
Needle Size (mm) 100
Show active ● all ○
☑ Show trajectory in 2D
☑ Show trajectory in 3D
☑ Orientation Cubes
Trajectory Line Width (1-10) 3.4

Figure 1.20 – Interface of the IFE planning mode. The environment allows the user to plan trajectories and review images along those trajectories prior to starting real time imaging.

sequence parameters without interrupting image acquisition. Hence slice position and orientation can be changed without loss of time, allowing tracking of the needle in real-time. Interactive environments intended to work with this kind of sequences were also developed. For example, Interactive Front System (IFE), a product of Siemens, designed to work with the interactive real-time pulse sequence (Beat-IRTTT)[Pan et al., 2011], allows the operator to focus on navigation rather than on manipulating classic MR parameters. This user-friendly interface is expected to save time. The trajectory and the insertion point can be planned in 3D according to anatomical constraints. (Fig.1.20). Slice parameters of the desired position are directly updated in the sequence parameter to save time. A thermal vizualisation mode offers the possibility of providing temperature and thermal dose maps in real-time in order to monitor thermal ablations. (Fig.1.21).

1.2.6 Monitoring by thermometry

MRI guidance is particularly suitable for the monitoring of thermal ablations thanks to its sensitivity to temperature changes. By providing a map of temperature in real-time, MR thermometry allows the radiologist to reach the target temperature for the destruction of cells. The first report of temperature mapping was based on the longitudinal relaxation time T_1 and was published in 1983 [Parker et al., 1983]. Today, other methods are also available to perform temperature mapping based on the diffusion coefficient and proton resonance frequency (PRF). A review of these techniques is available in [Quesson et al., 2000], but we will focus on the PRF technique because this method can be easily combined with elastography, as explained later. PRF technique is based on the fact that a temperature change yields a modification of the resonance frequency, resulting in a phase accumulation.

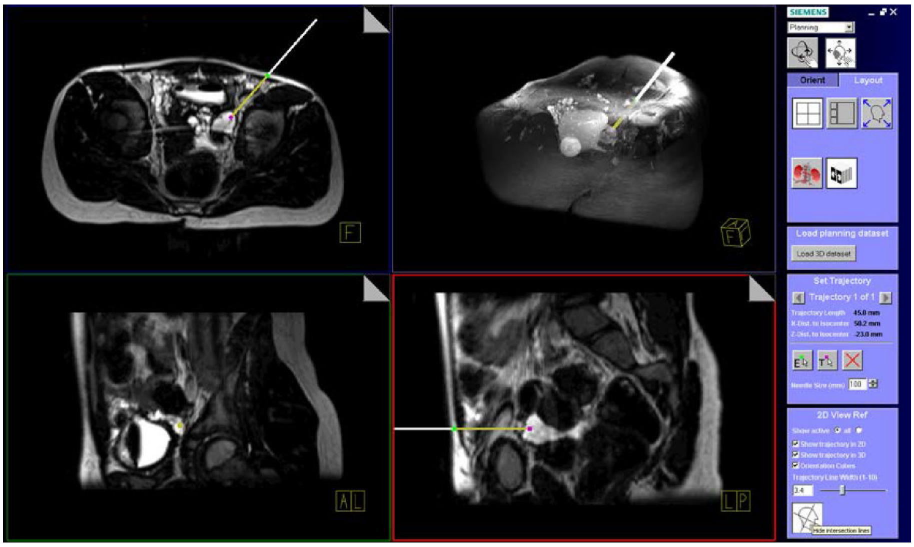

Trajectory Length 45.0 mm
X-Dist. to Isocenter 58.2 mm
Z-Dist. to Isocenter -23.0 mm
Needle Size (mm) 100
3.4

Figure 1.21 – Interface of the IFE thermometry mode. The environment allows the user to visualize a temperature or a thermal dose map refreshed in real-time.

This phase accumulation is visible on phase images after reconstruction in the spatial domain. According to the Larmor equation, the resonance frequency of a molecule depends on the local magnetic field observed by this molecule. The local microscopic magnetic field B_{loc} is not exactly the static magnetic field B_0 but also depends on the electron configuration that changes as a function of the temperature. Thus, the local magnetic field is defined as:

$$B_{loc} = (1 - \sigma)B_0 \tag{1.26}$$

with σ being the screening constant. Given that spins precess around B_{loc} axis with a precessional frequency ω_{loc}, the accumulated phase ϕ in radians during a gradient echo sequence is therefore described by:

$$\phi = \omega_{loc}TE = -\gamma TE(1 - \sigma)B_0 \tag{1.27}$$

with TE being the echo time. The minus sign in the first term is related to the fact that spins are precessing clockwise, whereas the positive direction for the phase is counterclockwise. The screening constant is directly related to the temperature T by a coefficient α ($\approx 0,01.10^{-6}\ {}^{\circ}C^{-1}$ for the water proton):

$$\sigma(T) = \alpha T \tag{1.28}$$

Let us take the example of two samples at different temperature T_a and T_b. The respective accumulated phase ϕ_a and ϕ_b are different:

$$\begin{aligned}\phi_a &= -\gamma TE(1-\sigma(T_a))B_0 = -\gamma TE(1-\alpha T_a)B_0 \\ \phi_b &= -\gamma TE(1-\sigma(T_b))B_0 = -\gamma TE(1-\alpha T_b)B_0\end{aligned} \tag{1.29}$$

The expression of the resulting difference $\Delta\phi = \phi_b - \phi_a$ provides the fundamental equation of the PRF method:

$$\Delta\phi = \alpha\gamma TEB_0(T_b - T_a) \tag{1.30}$$

By measuring the phase difference in the phase images , it is possible to estimate the temperature difference. It is important to highlight that the accuracy of the measurement and the temperature range depend on the TE parameter. The higher the range is, the lower the accuracy is. Combined to the temperature differences obtained with MR thermometry, the Arrhenius equation can be used to estimate the thermal dose and the area of cell death. Real-time MR thermometry based on PRF method has been successfully applied during thermal ablations and appears to be helpful to monitor the procedures and to precisely delineate the ablated zone [Seror et al., 2008].

1.2.7 Limitations and identification of needs

MRI is the most appropriate modality for the monitoring of thermal ablation, particularly thanks to MR thermometry. MR thermometry provides instantaneous information about an external parameter, the temperature. However, there is no information about structural property alteration. Thanks to the thermal dose estimation [Sapareto and Dewey, 1984], an approximation is provided but this equation does not take into account the local tissue conductivity, the variability of the tissue sensitivity or the blood flow. Besides, cell alteration may still occur after the ablation process without being related to a temperature increase. Furthermore, it must be emphasized that the required thermal dose is different according to the organ involved. More recently, it has been shown that the thermal dose required for the tumor destruction varies according to the modality used [Mertyna et al., 2009]. Supplementary information about an intrinsic property of the tissue is needed. Providing such an indicator is expected to improve the success rate of MR-guided thermal ablations. This project aims at providing a new indicator directly related to structural properties of tissues in real-time.

1.3 Mechanical properties as a new biomarker

1.3.1 Mechanical properties of tissue

A particularly interesting biomarker is the biomechanical properties. For a long time, palpation has been widely used as a clinical tool for the diagnosis of disease because of the relationship between significant changes in biological tissue mechanical properties and a pathology. For example, the breast cancer prevention is based on encouraging women to regularly palpate their breasts in order to detect the presence of stiffer regions as soon as possible. Palpation consists in estimating the deformation of a tissue subjected to a stress applied by the fingers. Palpation suffers from some limitations: some regions are difficult to reach with fingers and the diagnosis remains qualitative. Elastography methods have been developed in the 1990's to circumvent these limitations. Elastography methods are non invasive techniques allowing to quantitatively measure mechanical properties of biological tissues by using an imaging modality. The next paragraph is dedicated to the description of mechanical properties measured in elastography.

Elasticity in soft tissues

According to the theory of linear elasticity, the small deformations of an isotropic and homogeneous medium subjected to a stress is governed by the Hookes law:

$$\sigma_{ij} = \frac{E}{1+\nu}(\epsilon_{ij} + \frac{\nu}{1-2\nu}\epsilon_{kk}\delta_{ij}) \tag{1.31}$$

with σ_{ij} and ϵ_{ij} are the components of the stress and strain tensors respectively. ϵ_{kk} is the trace of the strain tensor in the Einstein notation and δ_{ij} is the Kronecker delta. E is known as the **Young's modulus**. ν is called the **Poisson's ratio** and provides information about the compressibility of the object. Fig.1.22 illustrates the case of an uniaxial stress. Typical values of E and ν are $E = 12$ GPa and $\nu = 0$ for cork, $E = 210$ GPa and $\nu = 0.3$ for steel.

The **shear modulus** μ is defined as $\mu = \frac{E}{2(1+\nu)}$. Given that an incompressible material has a Poisson's ratio equal to 0.5, the relationship $E = 3\mu$ is verified in this medium. The parameter λ is introduced, namely the **first Lamé coefficient**, defined by: $\lambda = \frac{E\nu}{(1+\nu)(1-2\nu)}$. Replacing the expression of μ and λ in Eq.(1.31) yields the Hooke's law:

$$\sigma_{ij} = 2\mu\epsilon_{ij} + \lambda\epsilon_{kk}\delta_{ij} \tag{1.32}$$

Let us remark that μ is also called the **second Lamé coefficient** but will be called shear modulus in the rest of the manuscript. The estimation of the shear modulus μ is at the heart of this project.

Wave propagation in elastic media

MRE relies on the analysis of the displacement induced by a harmonic excitation to the investigated tissue. This section focuses on wave propagation in isotropic and homogeneous media under assumption of small deformations. The underlying displacement is governed

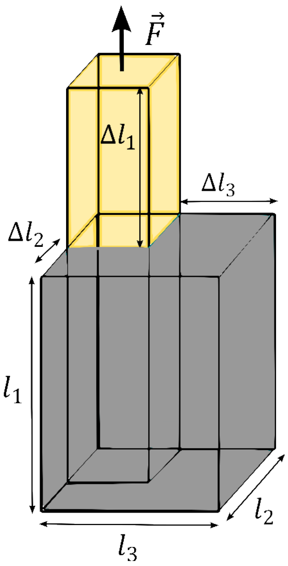

Figure 1.22 – Example of an object subjected to a uniaxial stress.In this case, $\epsilon_{ii} = \frac{\Delta l_i}{l_i}$ with $i = 1, 2, 3$ and $\sigma_{11} = \frac{F}{l_2 l_3}$. The Young modulus E and the Poisson coefficient ν are therefore equal to $E = \frac{\sigma_{11}}{\epsilon_{11}}$ and $\nu = \frac{\epsilon_{22}}{\epsilon_{11}} = \frac{\epsilon_{33}}{\epsilon_{11}}$

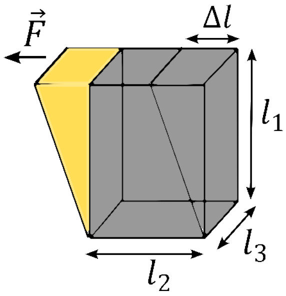

Figure 1.23 – Example of an object subjected to a shear stress.In this case, $\sigma_{12} = \frac{F}{l_2 l_3}$ and $\epsilon_{12} = \frac{\Delta l}{l_1}$. The shear modulus μ is therefore equal to $\mu = \frac{1}{2}\frac{\sigma_{12}}{\epsilon_{12}}$

by the motion equation (written with the Einstein notation):

$$\rho \frac{\partial^2 u_i}{\partial t^2} = \sigma_{ij,j} + \rho f_i \tag{1.33}$$

with u_i being the component of the displacement vector along the direction i, ρ the density of the medium and f_i the external volumetric forces. The strain tensor ϵ is defined from the displacement vector components u_i :

$$\epsilon_{ij} = \frac{1}{2}(u_{i,j} + u_{j,i}) \tag{1.34}$$

Under the assumption of no external volumic forces, replacing Eq.(1.32) and Eq.(1.34) in Eq.(1.33) yields :

$$\begin{aligned} \rho\tfrac{\partial^2 u_i}{\partial t^2} &= \mu(u_{i,j}+u_{j,i})_{,j}+\lambda\delta_{ij}u_{n,nj} \\ &= \mu u_{i,jj}+(\mu+\lambda)u_{j,ji} \end{aligned} \tag{1.35}$$

By using the conventional notations, the equation of the propagating wave in the elastic medium reduces to :

$$\rho\frac{\partial^2 u}{\partial t^2}=\mu\Delta\vec{u}+(\mu+\lambda)\vec{\nabla}(\vec{\nabla}.\vec{u}) \tag{1.36}$$

The first group of solutions of the equation is called longitudinal waves. A longitudinal wave is characterized by a propagation direction parallel to the produced motion. Mathematically, the rotational of the underlying motion of a longitudinal wave is null $\vec{\nabla}\wedge\vec{u}=0$. Under this condition and by using the following relationship $\vec{\nabla}(\vec{\nabla}.\vec{u})=\vec{\nabla}\wedge(\vec{\nabla}\wedge\vec{u})+\Delta\vec{u}$, Eq.(1.36) reduces to:

$$\rho\frac{\partial^2 u}{\partial t^2}=(2\mu+\lambda)\Delta\vec{u} \tag{1.37}$$

The longitudinal harmonic wave, solution of the equation, is hence described by:

$$\Delta\vec{u}+\frac{\rho\omega^2}{\lambda+2\mu}\vec{u}=0 \tag{1.38}$$

with ω being the angular frequency. From Eq.(1.38), the longitudinal wave celerity C_l is deduced:

$$C_l=\sqrt{\frac{\lambda+2\mu}{\rho}} \tag{1.39}$$

The second group of solutions is called shear waves. A shear wave is characterized by the absence of volume change, which is related to a null divergence $\vec{\nabla}.\vec{u}=0$. In this particular case, Eq.(1.36) reduces to:

$$\rho\frac{\partial^2 u}{\partial t^2}=\mu\Delta\vec{u} \tag{1.40}$$

The harmonic shear wave is therefore governed by this expression:

$$\Delta\vec{u}+\frac{\rho\omega^2}{\mu}\vec{u}=0 \tag{1.41}$$

In the same manner, the celerity of the shear wave is defined by:

$$C_s=\sqrt{\frac{\mu}{\rho}} \tag{1.42}$$

In biological tissues, the celerity of compression waves is typically 1000 times higher than the celerity of the shear wave ($1\ m/s$). Let us notice that an additional assumption of incompressibility ($\nabla.\vec{u}=0$) enables to select only shear waves as solutions of the equation. Incompressibility is an acceptable assumption for most soft tissues. It is important to highlight that the celerity of the shear waves is directly related to the shear modulus. Dynamic elastography relies on computing the shear modulus by estimating the celerity of shear waves from images.

It must be reminded that above mentioned equations are valid under assumption of purely elastic medium. Although the viscosity parameter is not investigated in the current project, its effect is not negligible. A significant viscosity is responsible of the wave attenuation. This effect is more important at high frequencies. Without entering into details, viscosity can also be estimated in elastography by defining a complex coefficient μ^*. The real part refers to the shear modulus and the imaginary part is related to the viscosity [Vappou et al., 2009].

1.3.2 Harmonic motion encoding on MR images

It has been previously shown that mechanical properties of a medium can be assessed when knowing the celerity of a shear wave propagating in this medium. Estimating velocity information requires the knowledge of the displacement field. The current section aims at describing how the underlying displacement of a shear wave is encoded on MR images. Nuclear magnetic resonance equations introduced in the section 1.2.1. are needed to describe the relationship between the position vector of a particle subjected to a shear wave and the phase of its magnetization vector. When applying a linear magnetic field gradient $\vec{G_r}$ in an arbitrary direction $\vec{r}$ during a time T, the phase ϕ accumulated by the transverse magnetization of a particle during this period is obtained by integrating the Larmor relationship:

$$\phi(\vec{r}) = \gamma \int_0^T \vec{G_r}(t).\vec{r}(t)dt \tag{1.43}$$

with $\vec{r}$ being the position vector of the particle. Under the assumption of a monofrequential wave propagating through the tissue, the expression of $\vec{r}(t)$ satisfies Eq.(1.41):

$$\vec{r}(t) = \vec{r_0} + \vec{u_0}\sin(\omega t - \vec{k}.\vec{r} + \alpha) \tag{1.44}$$

with $\vec{r_0}$ being the mean position, $||\vec{u_0}||$ the motion amplitude, α the initial phase and ω the mechanical angular frequency. $\vec{k}$ is the wave vector defined as:

$$\vec{k} = \frac{2\pi}{\lambda_s}\vec{u_k} = \sqrt{\frac{\rho\omega^2}{\mu}}\vec{u_k} \tag{1.45}$$

with $\vec{u_k}$ being the propagation direction and λ_s the spatial wavelength. Let us now implement N_p cycles of a bipolar magnetic field gradient, the duration of one cycle is set to one mechanical excitation period T_e.

$$G(t) = \begin{cases} G_0 \sin(2\pi f_e t) & t \in [0, N_p T_e] \\ 0 & otherwise \end{cases} \tag{1.46}$$

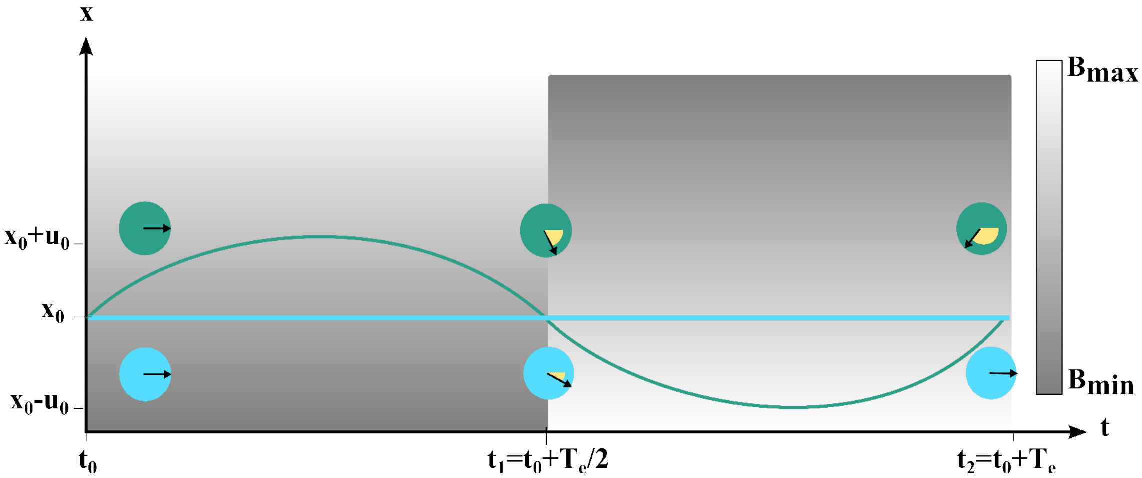

Figure 1.24 – Illustration of the motion encoding. A bipolar magnetic gradient field (MEG) is applied along the x-direction, the spatial resulting magnetic field variation is represented on a gray scale. The accumulated phase of the transverse magnetization vectors of an unmoving spin (blue) and a moving spin(green) are shown in the circular diagrams before, in the middle, and after the MEG. The moving spin has a sinusoidal trajectory along x. At $t = t_0$, the accumulated phase of the transverse magnetization vectors are equal to 0. After applying the first lobe of the MEG, both spins have accumulated phase but the phase of the unmoving spin is canceled by the second lobe while the phase of the moving spin is increased by a factor 2.

with $f_e = \frac{\omega}{2\pi} = \frac{1}{T_e}$. Replacing the expression of $\vec{G_r}$ and $\vec{r}$ in Eq.(1.43), leads to:

$$\phi(\vec{r}, \alpha) = \gamma \int_0^{N_p T_e} \vec{G_0} \sin(\omega t).\vec{u_0} \sin(\omega t - \vec{k}.\vec{r} + \alpha) dt \tag{1.47}$$

Using classic trigonometric formula allows writing the expression of the phase signal:

$$\phi(\vec{r}, \alpha) = \frac{\gamma N_p (\vec{G_0}.\vec{u_0})}{2 f_e} \cos(\vec{k}.\vec{r} - \alpha) \tag{1.48}$$

The observed MRI phase shift acquired with a gradient echo sequence including the described *Motion Encoding Gradient*, MEG, $\vec{G_r}$, is proportional to the scalar product of the position vector and the MEG. Let us highlight that the more MEG cycles there is and the higher the amplitude is, the higher the motion encoding is. It is also important to notice that the encoding direction is an essential parameter, since the MEG encodes only the movement in its direction.

To better understand the motion encoding principle, the relevance of using a bipolar gradient must be emphasized. The second lobe of the gradient (same amplitude, same duration, opposite polarity) allows refocusing the phase of unmoving spins that has been accumulated during the first lobe. The accumulated phase of moving spins is increased by a factor of 2 because the polarity of the gradient is inverted as well as the displacement. The principle is illustrated in Fig.1.24. Eq.(1.48) can be interpreted as follows: the phase image

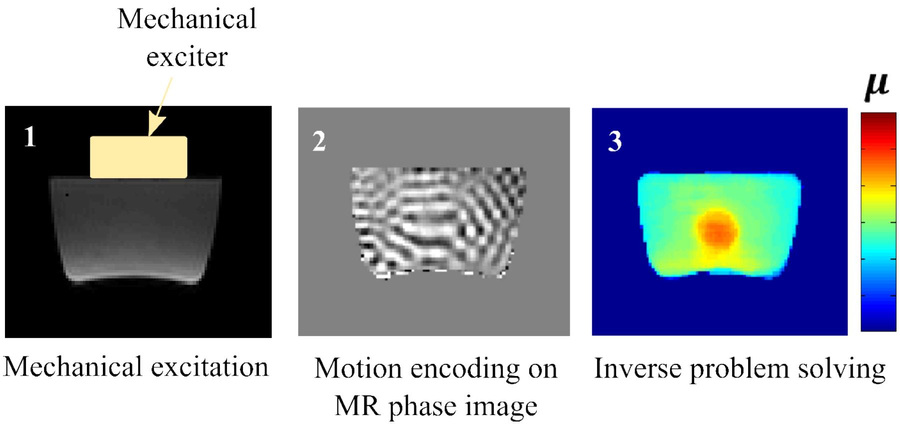

Figure 1.25 – Basic principle of MRE illustrated on a gelatin phantom with a stiffer inclusion. The first step is the generation of a mechanical wave through the object. The produced motion is encoded on MR phase images by a motion encoding MR pulse sequence. By solving an inverse problem, the wave propagation speed is estimated in every pixel to compute an elasticity map.

acquired with a motion encoding sequence is a kind of photography at a given time of the displacement induced by the harmonic excitation.

Let us remind that the objective is to estimate the mechanical properties of the tissue. It has previously been shown that the celerity of the shear wave propagating through a medium depends on its shear modulus (Eq.(1.42)). As demonstrated in this section, the displacement at a given time, generated by the excitation can be encoded on MR phase images. An inverse problem solver is then required to estimate the celerity of the wave and consequently the shear modulus from the known displacement.

1.3.3 Magnetic Resonance Elastography

First MRE experiments, as we know it today, were reported in[Muthupillai et al., 1996]. MRE relies on 3 steps: the mechanical excitation, the motion encoding and the inverse problem solving. The mechanical excitation is required to generate a shear wave propagating through the investigated tissue. The classic way is the use of a surface driver that transmits the wave through the skin. The displacement produced by the excitation is encoded on a MR-pulse sequence by implementing a MEG. Since the wave propagation speed depends on mechanical properties, resulting MR phase images are processed to estimate the shear modulus by solving an inverse problem. Fig.E.1 summarizes this principle. During the last decades, the ability of MRE to detect pathology has been proven. For example, hepatic fibrosis has been shown to be related to an increase in the shear modulus [Asbach et al., 2010, Huwart et al., 2006] (Fig.1.26). A higher modulus may also reflect the presence of cancerous tissue as it has been shown in liver, breast and prostate [Sinkus et al., 2000, Garteiser et al., 2012, Chen et al., 2010]. On the contrary, neurodegenerative disorders may be related to a lowered stiffness [Streitberger et al., 2012,

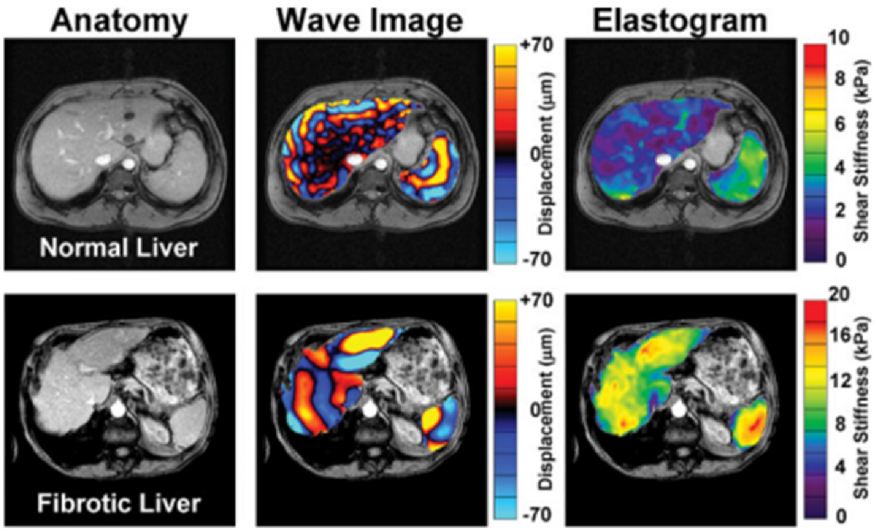

Figure 1.26 – Hepatic fibrosis assessed by MRE . Image from [Yin et al., 2007]

Schregel et al., 2012, Murphy et al., 2012]. MRE has also shown promising results for the detection of dysfunction of the cardiac muscle [Elgeti et al., 2010a]. Recently, the Duchenne muscular dystrophy has been proven to be associated with changes in muscle stiffness [Bensamoun et al., 2015]. Promising results on rat lungs have shown that edemateous lung are softer than normal lung. More surprising organs were also investigated by MRE: the tongue [Cheng et al., 2011] or even an ex-vivo eye [Litwiller et al., 2010].

1.3.4 Changes in mechanical properties

MRE is now clinically accepted as a tool for diagnosis of pathology because a change in stiffness may reflect the presence of disease. In the context of this project, a biomarker is wanted for the monitoring of thermal ablations. The biomarker analysis is expected to quantitatively assess the tissue damage. The energy deposit occuring during a thermal ablation results in a modification of the structural organization (protein denaturation, vaporization, carbonization). The hypothesis behind this work is that these structural changes will significantly alter the intrinsic properties of the tissue and consequently its elastic properties. Over the past two decades, several research groups have attempted to verify this hypothesis. First results in [Stafford et al., 1998] have shown a good correlation between an increased elastic modulus and the necrosis (Fig.1.27). Ultrasound elastography measurements were performed in different parts of the region ablated by laser and compared to histopathological results. The lesion size assessed by the two methods were well correlated. This study has also proven the ability of ultrasound elastography to distinguish different regions of the lesion in term of stiffness. These promising results encouraged other groups to pursue in this direction. Stiffness was shown to increase strongly after in vivo radiofrequency ablation [Varghese et al., 2002] or laser ab-

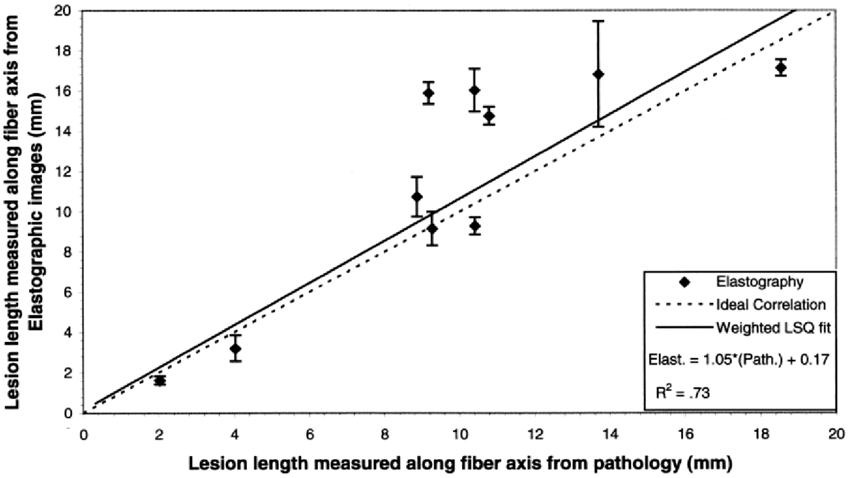

Figure 1.27 – Correlation between elastographic and gross pathology assessment of the laser-induced lesion size. Image from [Stafford et al., 1998]

lation [Mariani et al., 2014] in the liver and after in vivo HIFU therapy in the prostate [Souchon et al., 2003] and in the brain [Larrat et al., 2010]. Based on these successful experiments, the study of elastic parameters has been extended from before/after to during the procedure. First, a small dependence of the shear modulus versus temperature before necrosis was assessed by ultrasound elastography during HIFU treatments while a significant change in stiffness occurred after the necrosis [Bercoff et al., 2004]. Further studies allowed a better understanding of the relationship between elasticity changes and the increased temperature [Wu et al., 2001, Sapin-de Brosses et al., 2010]. Muscular samples were slowly warmed up and cooled down into a thermally controlled container. Reversible changes in stiffness before reaching 49 °C were observed while irreversible changes occurred for temperature between 50 °C and 80 °C (Fig.1.28). The reversible modifications are probably due to the folding/unfolding proteins and irreversible changes are explained by the irreversible collagen denaturation and myosin gelation. In the muscle, the relationship between exposure time, temperature and elasticity was also demonstrated to be equivalent to the relationship between exposure time, temperature and necrosis established by [Sapareto and Dewey, 1984]. Based on these promising conclusions, real-time elastography recently emerged to assess tissue damages during a thermal ablation. The real-time monitoring of a HIFU ablation by shear wave ultrasound elastography was firstly successfully performed [Arnal et al., 2011]. Experiments were carried out on ex vivo and in vivo muscles. The elasticity increase is shown in Fig.(1.29). Shortly afterwards, the MRE monitoring of a laser thermal ablation of in vivo swine livers was published [Chen et al., 2013]. MRE acquisitions were performed with a minimum interval of 30 seconds. Temporal evolution of the elasticity is shown in Fig(1.30).

It must be noticed that each organ has a different composition and the assumptions about

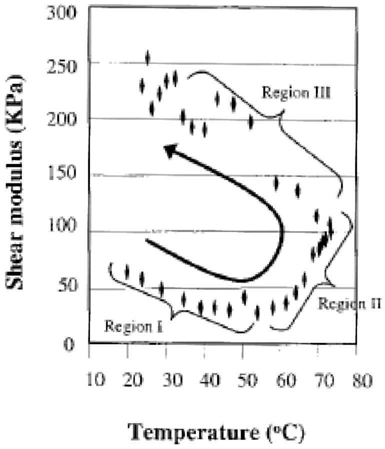

Figure 1.28 – A bovine tissue sample shear modulus during the heating and cooling down process.Image from [Wu et al., 2001]

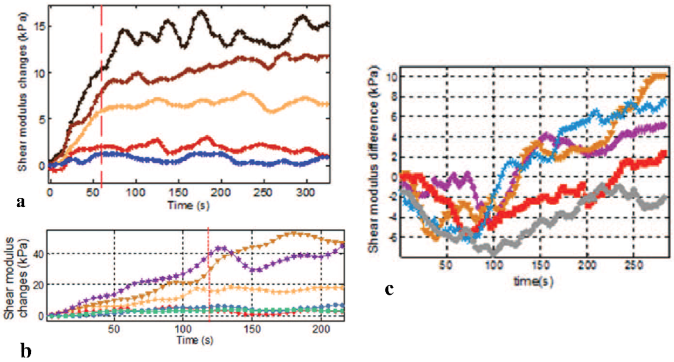

Figure 1.29 – a)Evolution of the shear modulus changes measured by ultrasound elastography at different locations during HIFU treatment performed on a)in vivo sheep muscle, b) ex vivo porcine muscle and c)ex vivo turkey breast. Images from [Arnal et al., 2011]

denaturation of proteins are only appropriate to this particular organ. For the same reason, the curve of the shear modulus versus temperature is different according to the investigated organ. This explains why it is difficult to establish empirical temperature thresholds and use them with confidence to assess the treatment response. A case-by-case evaluation of changes in mechanical properties is required. Each tissue, each patient do not react in the same manner to a thermal ablation procedure. An elasticity monitoring is required to assess with efficiency and accuracy the treatment response.

The current project aims at developing interventional MRE. The objective of the first part of this study is the design of an all-in-one interventional MRE system, so that an elasticity map of the ablated region is provided to the radiologist with a high refresh rate (of the order of a second). In order to achieve this goal, a dedicated excitation device must be

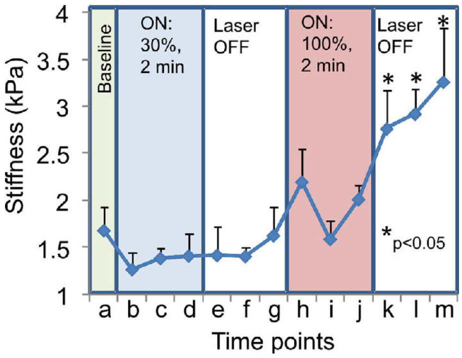

Figure 1.30 – a)Evolution of the shear modulus measured by MRE at different time points of the in vivo laser thermal ablation performed on a swine liver. Image from [Chen et al., 2013]

designed, a specific MR pulse sequence with motion encoding must be developed and an inverse problem solver must be implemented.

Chapter 2

From diagnostic MRE to interventional MRE

> " *Aussitôt qu'on nous montre quelque chose d'ancien dans une innovation, nous sommes apaisés.* "
>
> Friedrich Nietzsche

Contents

This chapter introduces a new interventional MRE system dedicated to the monitoring of percutaneous thermal ablations. A quick overview of existing mechanical exciters, MRE pulse sequences and inverse problem solvers is provided. After defining the specifications required for interventional MRE, the different parts of interventional MRE system that we have developed are detailed.

2.1 Mechanical excitation

2.1.1 Overview of MRE mechanical exciters

In MRE, an excitation device is required to generate a shear wave inside the investigated tissue. The commercial device (Resoundant®, Rochester, MN) is a pneumatic surface exciter. A loudspeaker is placed outside the MRI scanner room to avoid any interference and a passive driver of 17cm in diameter is placed on the skin of the patient. The mechanical vibration is transmitted by a pneumatic tube (Fig. 2.1). Although the exciter is specifically designed for liver examination [Talwalkar et al., 2008, Dresner et al., 2004], other organs such as thigh muscles have been studied with this device [Bensamoun et al., 2006]. Instead of using a loudspeaker and a pneumatic tube, [Lewa et al., 2000] proposed a rigid transmission of motion using a long rod. Based on the two latter principles, [Sack et al., 2008] developed a device dedicated to the brain examination using a long rod driven by a loudspeaker (Fig.2.2). More recently, the same group demonstrated the possibility of generating a mechanical wave in the brain with an actuator driven by medical compressed air [Braun et al., 2015]. Another approach to generate a wave inside biological tissues from the surface is the use of a piezoelectric actuator. Piezolectric materials are composed of quartz crystals that change shape when exposed to an electrical potential. Since piezoelectric material are MR compatible and the resulting motion is more precisely controlled, this technology was widely investigated for the purpose of MRE actuation. [Uffmann et al., 2002, Tse et al., 2011, Weaver et al., 1999] (Fig.2.3). The last option proposed to induce a vibration from the surface is the use of electromagnetic coils. This technique uses the property of the main magnetic field of inducing a mechanical torque into active coils. The mechanical vibration is obtained by applying an alternative current through the coil [Braun et al., 2003, Rossman et al., 1999]. The MRE excitation by electromagnetic coils is inexpensive but is limited in terms of position and orientation.

Surface excitation devices suffer from the wave attenuation through the biological tissue. Given that high frequencies are rapidly attenuated, only low frequencies can be used to reach deep-lying regions. However, the lower the frequency is the higher the wavelength is, and the size of the smallest detectable object is limited by the wavelength of the propagating wave. Therefore, a tradeoff is needed between a low attenuation and a high resolution. In order to limit the attenuation through the tissue when investigating deep-lying regions, several alternatives to surface exciters have been proposed. MRE experiments were

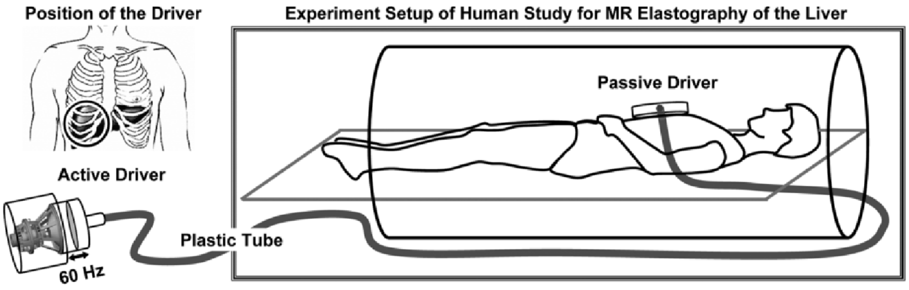

Figure 2.1 – Pneumatic surface exciter. Image from [Talwalkar et al., 2008]

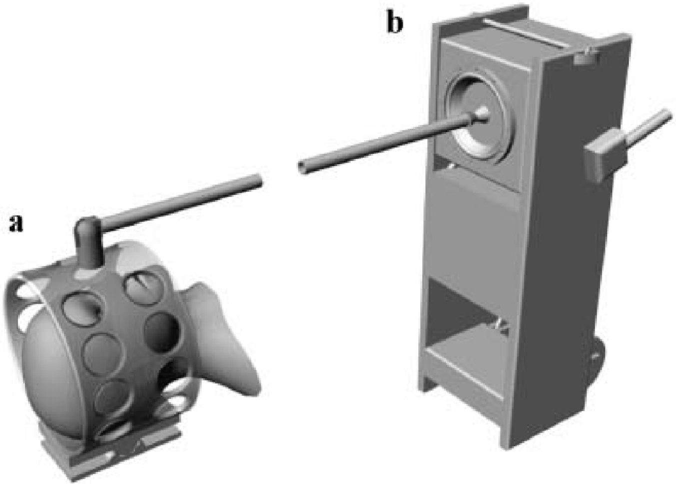

Figure 2.2 – a)Head rocker unit and b) remote vibration generator. Image from [Sack et al., 2008]

carried out by using the vibration of the MRI table induced by the MR pulse sequence [Gallichan et al., 2009]. This technique is limited by the fact that the frequency and the amplitude are imposed by the MRI table. Others groups proposed to use the intrinsic excitation due to physiological phenomena. Elasticity measurements were obtained by using the blood pressure pulses and cerebrospinal fluid exchange, as excitation sources [Zorgani et al., 2015, Weaver et al., 2012].

In the years 2000, the excitation by ultrasound was investigated. As described in the introduction, tumoral tissue can be destroyed using focused ultrasound. By modulating the signal at a frequency between 50 and 200 Hz, the same device can be used to generate a shear wave that propagates around the focal point [Wu et al., 2000]. The main advantage of the excitation by focused ultrasound is that a controlled shear wave is directly generated within the region of interest, which circumvents the attenuation problem. There is currently growing interest for the excitation by focused ultrasound within the context of the monitoring of HIFU ablations [Yuan et al., 2007]. The same non-invasive device would be used for the treatment and the monitoring. This excitation source is particularly well-adapted for this application but the setup is bulky and its use is not

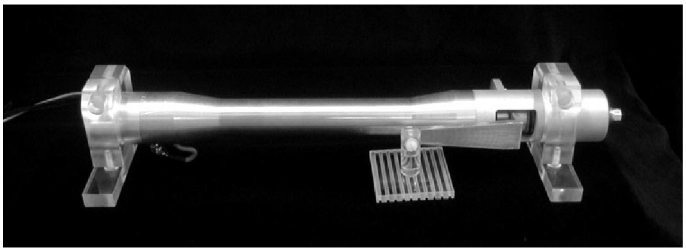

Figure 2.3 – Piezoelectric actuator that must be placed such as the coupling plate is in contact with the tissue surface. Image from [Uffmann et al., 2002]

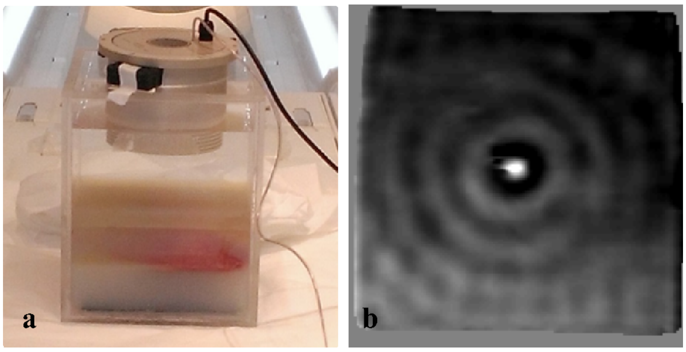

Figure 2.4 – a)Setup of an MRE experiment on a gelatin phantom in a water bath with focused ultrasound excitation. b) MRE Wave pattern obtained with this setup.

trivial. Extreme care must be taken to avoid acoustic obstacles, such as air regions along the ultrasonic beam trajectory. In order to ensure acoustic coupling, phantoms experiments can be carried out in a water bath (Fig.2.4). The in vivo experiments are more challenging. More invasive methods have aroused interest in specific applications. Transurethral and endorectal actuators were designed to directly generate a shear wave in the prostate [Chopra et al., 2009, Thörmer et al., 2013]. More recently, it has been shown that the vibration of a needle inside the tissue of interest is able to generate a shear wave [Chan et al., 2006]. The needle MRE driver consists in a piezolelectric actuator mounted on a needle (Fig.2.5.a). Although the method is more invasive, specific applications can benefit from the needle excitation that allows to easily generate a shear wave within any deep-lying region. The wave pattern induced by a surface exciter and a needle driver are compared in a gel phantom in Fig.2.5.b-c [Chan et al., 2006]. The wave generated by the surface driver propagates in a limited region near the surface while the wave generated by the needle driver is well-defined along the entire length of the needle. Therefore, deep-lying regions are expected to be easily reached by this kind of device. Furthermore, the circular wave pattern induced by this kind of device is particularly well-defined, which makes easier the inverse problem solving. This device is particularly relevant in the context of percutaneous procedures because needles are already required. The use of a needle as an MRE exciter was proposed to complete a biopsy protocol [Zhao et al., 2008]. A complementary

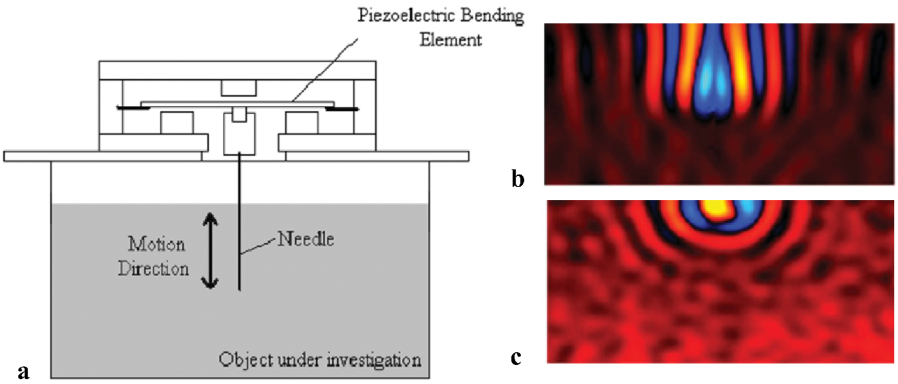

Figure 2.5 – Needle MRE driver. Image from [Chan et al., 2006]

MRE examination would be performed in the same time as the biopsy with the same needle. The needle is driven by an electromechanical actuator. Lately, a successful use of a needle driver for the assessment of a thermal ablation was reported [Chen et al., 2013]. An acoustic actuator is mounted on a laser ablation cooling catheter to generate a wave directly in the ablated region of interest. MRE acquisitions were performed before, after and during the ablation with a miminum of 30 seconds between two of them.

2.1.2 A needle MRE driver as mechanical exciter for interventional MRE

A wide variety of mechanical exciters are available in the literature. However, the mechanical exciter required for our all-in one interventional MRE system has to meet the specifications imposed by the context of interventional MRI. Radiologists must handle in a confined space limited by the patient body and the MRI scanner tunnel. The mechanical exciter has to be compact and leave enough space for the needle insertion. Given that the all-in-one interventional MRE system is intended to monitor a small region of interest under ablation, the spatial resolution must be high enough to detect the lesion. As previously explained, this constraint prevents the use of very low excitation frequencies. However, the tumor can be located in a deep-lying region, which prevents the use of a surface driver due to wave attenuation through the tissues. For all these reasons, a surface exciter is not recommended in this context.

In the framework of percutaneous thermal ablation, we designed a minimally invasive system inspired from the needle drivers previously mentioned (Fig.2.6). A piezoelectric actuator makes a needle longitudinally vibrate inside the tissue directly within the region of interest. The mechanical stimulation of the needle can vary from 50 Hz to 200 Hz. The displacement amplitude depends on the applied voltage and the constraint exerted by the tissue on the needle. The typical displacement is 100 μm in the direction of the needle shaft axis in the absence of any mechanical load. More details are given in Appendix A

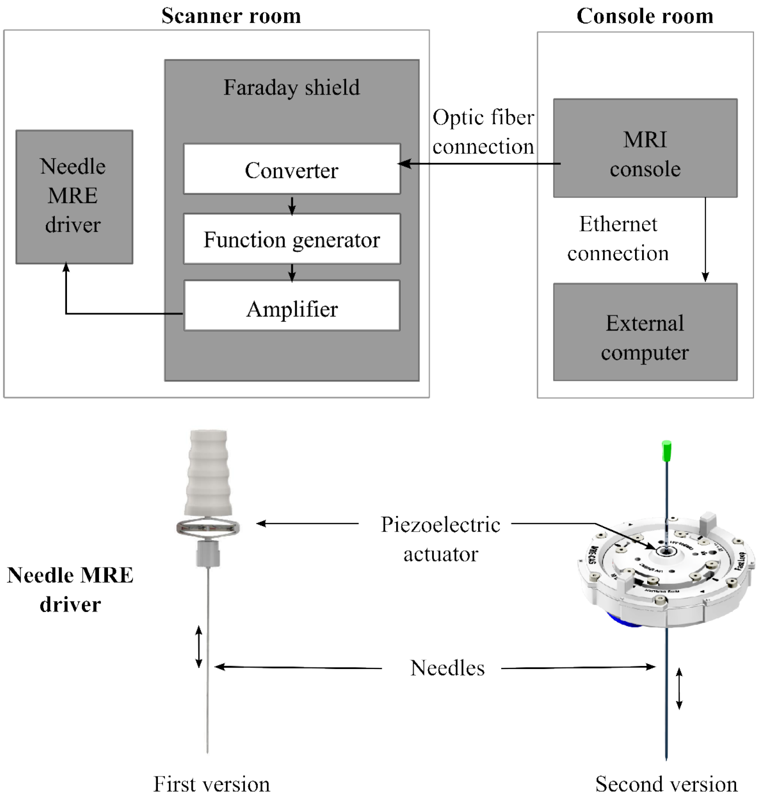

Figure 2.6 – Needle MRE drivers and schematic diagram of the interventional MRE system. The piezoelectric actuator is triggered by the MR pulse sequence. It makes the needle vibrate longitudinally. Elastograms are reconstructed in real-time on an external computer connected to the MRI console.

and B.

Two different needle MRE drivers were designed: the first version is composed of an MR-compatible piezoelectric stack driver (APA™150M, Cedrat) and the second one includes a ring-shaped piezoelectric bending actuator (CMBR08, Noliac ®) (Fig.2.6). The MR-compatible piezoelectric stack driver was chosen for its simplicity of use, its low bulk that was particularly appreciated in the interventional MRI environment, and its reliability and safety in terms of displacement range, intrinsically limited by the actuator. The needle is fixed to the actuator and the device is hand-held. More details about this device are given in Appendix A. In order to more easily use any needle even cryoablation applicator, we designed the second version of the needle MRE driver. This circular shape of the actuator with a hole in the middle offers the possibility of inserting the needle or removing it once the device is correctly positioned on the skin. A pneumatic system enables to secure the needle when required. The radiologist does not need to held the needle. More details are given in Appendix B.

2.2 Motion encoding MR pulse sequences

2.2.1 Overview of MRE pulse sequences

The motion induced by the mechanical excitation is encoded on phase images, by adding a bipolar gradient to a standard MR pulse sequence. Gradient echo sequences were the first pulse sequences used to develop MRE [Muthupillai et al., 1996]. As previously described, a bipolar motion encoding gradient is added before the readout gradients. In order to synchronously encode the movement for every line of the k-space domain, the sequence must be triggered on the mechanical excitation (or reverse) so that a whole number of mechanical periods corresponds to exactly one TR. From the first reported experiments, several improvements have been developed to enhance the wave image. First, two images are acquired with opposite MEG polarities. Their difference allows to remove the constant phase background while increasing the motion encoding by a factor 2. An alternative consists in acquiring a single reference phase image without mechanical excitation that is subtracted to the motion encoded phase images. This approach requires less image acquisitions but the motion encoding is not increased. The second refinement is based on harmonic analysis. Although the MEG is designed to particularly well encode the sinusoidal movement at a given frequency, any movement may be encoded. In order to select only the motion component of interest, a temporal Fourier transform is performed. Several images are acquired with a different delay between the motion encoding and the mechanical excitation. The phase-offsets are regularly spaced across a mechanical period. A temporal Fourier transform is performed over the phase image dataset and only the component associated to the mechanical excitation frequency is selected. The image processing steps are performed on the resulting wave image. Fig. 2.7 shows the chronogram of a basic MRE sequence based on a gradient echo pulse sequence. In order to simplify the chronograms, the MEG with opposite polarity and the phase-offsets will not be represented thereafter in the next figures.

Many MRE parameters can be adjusted to improve the quality of the measurements:

- increasing the number of MEG cycles and the MEG amplitude improves the sensitivity to the motion (Eq.(1.48))
- increasing the number of phase-offsets improves the efficiency of the temporal filtering
- acquiring several wave images with different motion encoding directions allows to better characterize the wave propagation
- investigating a range of excitation frequencies allows to study viscoelastic properties

While main refinements intended to improve the elastogram quality imply longer acquisition times, many factors incite the reduction of acquisition times in order to:

- improve the patient comfort

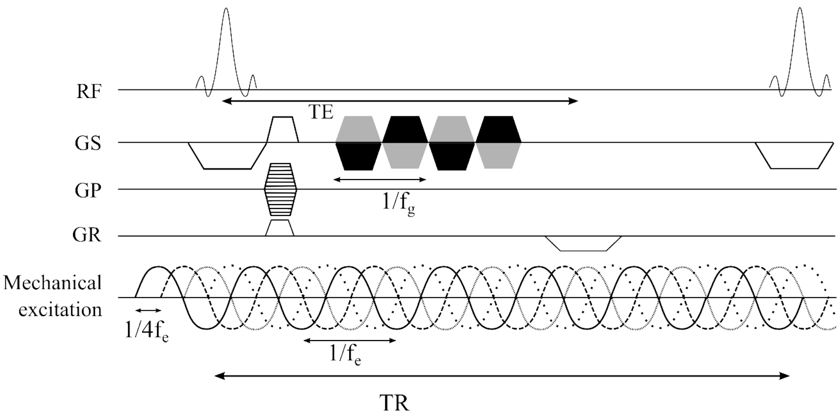

Figure 2.7 – Chronogram of a basic MRE pulse sequence with motion encoding. Two cycles of MEG are implemented in the SS direction (in black). GS, GP, GR, are gradients in slice, phase and read direction, respectively. The MEG can be applied in any direction. f_g and f_e are encoding and mechanical excitation frequencies, respectively. Same images are also acquired with the opposite MEG polarity (in gray). Several pairs of images are acquired with different delays between motion encoding and mechanical excitation represented here by four different lines corresponding to four phase-offsets between mechanical excitation and MEG.

- overcome the issue of a finite T_2 relaxation time
- minimize the impact of physiological motions
- decrease the breath-hold duration when needed
- increase the high refresh rate required in interventional MRI

Most of MRE technical improvements rely on finding the best tradeoff between acquisition time and elastogram quality. Standard MRI acceleration techniques were used to optimize the acquisition time. MEG were then implemented into many other MR pulse sequences. Implementing MEG in spin-echo sequences allows to circumvent the issue of the T_2^* decay due to main magnetic field inhomogeneities. MEG can be implemented on each side of the refocusing pulse to increase the motion encoding. Given that spin-echo sequences require a long acquisition time, echo planar imaging is used to reduce the total acquisition time. Single shot SE-EPI with motion encoding was used for the study of several organs such as the brain [Sack et al., 2008], liver [Asbach et al., 2010] and kidney [Lee et al., 2012]. The use of a segmented SE-EPI with an echo train of 3 was also proven to provide equivalent results to those obtained by the standard spin echo while reducing the acquisition time from 20 minutes to 120 seconds for a typical protocol [Huwart et al., 2008]. The use of fast gradient echo sequences had to wait until the development of the fractional encoding. The feasibility of using a MEG duration shorter than a mechanical excitation period was demonstrated in [Rump et al., 2007]. Fractional encoding consists in using an encoding

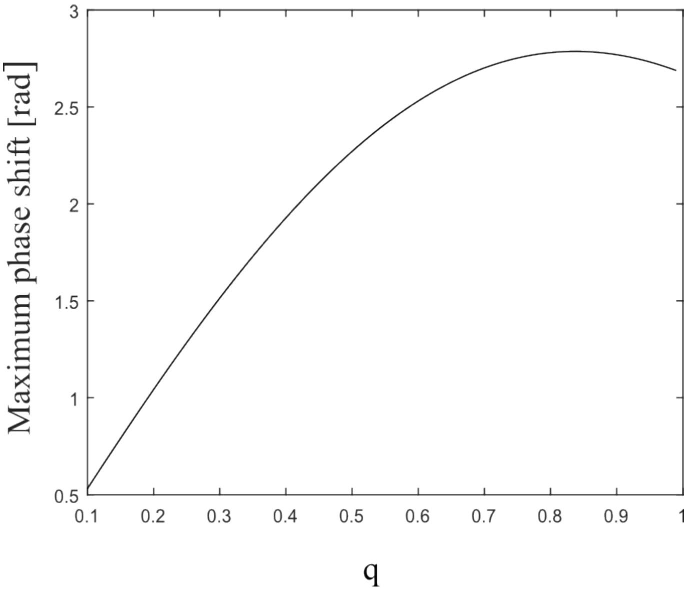

Figure 2.8 – Maximum phase shift originating from the motion encoding in function of the ratio $q = \frac{f_e}{f_g}$. The maximum displacement u_0, the MEG amplitude G_0 and the MEG duration T_g are respectively set to 100 μm, 20 mT/m and 10 ms.

frequency $f_g = \frac{1}{T_g}$ superior to the mechanical excitation frequency $f_e = \frac{1}{T_e}$:

$$G(t) = \begin{cases} G_0 \sin(2\pi f_g t) & t \in [0, T_g] \\ 0 & otherwise \end{cases} \tag{2.1}$$

By replacing the expression of $\vec{G}$ in Eq.(1.43), the accumulated phase by a particle moving at the excitation frequency is:

$$\phi(\vec{r}, \alpha) = \gamma \int_0^{T_g} \vec{G_0} \sin(2\pi f_g t).\vec{u_0} \sin(2\pi f_e t \quad \vec{k}.\vec{r} + \alpha) dt \tag{2.2}$$

The use of trigonometric properties allows to reduce the previous Eq.(2.2) to:

$$\phi(\vec{r}, \alpha) = \frac{\gamma f_g (\vec{G_0}.\vec{u_0})}{\pi (f_g^2 \quad f_e^2)} \sin(\frac{\pi f_e}{f_g}) \cos(\frac{\pi f_e}{f_g} \quad \vec{k}.\vec{u} + \alpha) \tag{2.3}$$

Fig.2.8 shows the relationship between the maximum phase shift originating from the motion encoding gradients and the ratio $q = \frac{f_e}{f_g}$. Although the sensitivity to the motion decreases when the ratio is low, the phase shift is still proportional to the displacement. The feasibility of reducing the MEG duration by using a smaller frequency is of great benefit to reduce the echo time and consequently the repetition time in gradient echo sequences. Thanks to fractional encoding, the use of steady state gradient echo sequences with motion encoding emerged (see section 1.2.4). Steady-state gradient echo sequences involve a short

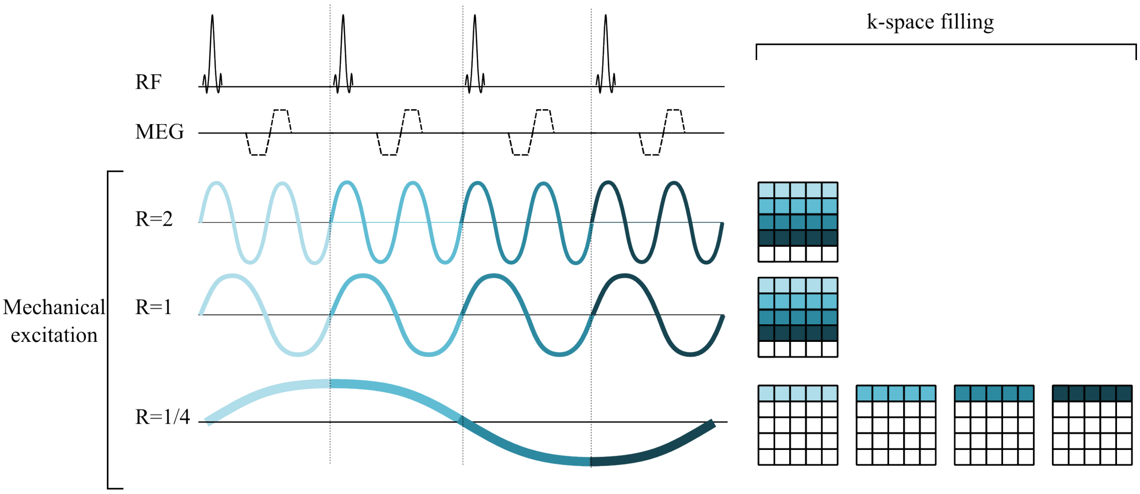

Figure 2.9 – Three types of fractional encoding. One vibration period is matched to $\frac{1}{2}$, 1 and 4 TR ($R = 2$,$R = 1$ and $R = \frac{1}{4}$ respectively). The corresponding k-space filling is schematized on the right. When $R \geq 1, R \in \mathbb{N}$, one k-space image is filled line by line. When $R < 1$ several k-space images are filled at the same time, corresponding to different phase-offsets

TR and the transverse magnetization is spoiled (SSI) or refocused (SSC) before each rf-pulse. The echo time is as short as possible to minimize T_2^* decay, the MEG duration must therefore be short as well. Since the MEG duration is not determined by the mechanical excitation period anymore, the MEG duration is adjusted so that the motion sensitivity is sufficient and the echo time is not considerably extended. The number of mechanical excitation periods included in one repetition time is variable. When the ratio $R = \frac{TR}{T_e} \geq 1$ and $R \in \mathbb{N}$, the phase shift accumulated after each MEG is unchanging and the k-space domain is filled in the same manner as the conventional MRE without fractional encoding. When $R < 1$ and $R \in \mathbb{Q}$, the MEG does not encode the motion at the same time of the mechanical period for each rf pulse, several images are therefore acquired in the same time corresponding to different phase-offsets of the mechanical excitation. Let us take the case of $R = \frac{1}{4}$, 4 images corresponding to 4 phase-offsets are acquired by interleaving the lines of the 4 k-space images (Fig.2.9). The resulting images are used for the harmonic analysis intended to select only the temporal frequency component of interest. The combination of two low ratios $q = \frac{f_e}{f_g}$ and $R = \frac{TR}{T_e}$ allows to perform MRE acquisitions on moving organs even with a low mechanical frequency. Successful MRE acquisitions of the heart were performed with $R = \frac{1}{8}$ and $q = 0.05$ [Sack et al., 2009, Elgeti et al., 2010b]. Higher ratios (q=0.5 and R=1) have also been used for the heart examination [Kolipaka et al., 2012]. This technique was also used to reduce the TE in case of short T_2 relaxation time, especially when the magnetic field is high: it has been proposed to combine echo planar imaging with fractional encoding (q=0.5) in spin-echo sequence for the liver examination at 3T [Herzka et al., 2009]. The emergence of fractional encoding also made multifrequency MRE acquisitions possible. Due to viscoelastic properties of the biological tissues, mechanical properties may vary according to the excitation frequency applied to the tissue. Some groups were therefore interested in investigating the viscoelastic properties of the tissues. The first possibility is to multiply MRE acquisitions by varying the excitation and MEG frequencies, but a faster approach using the fractional encoding was proposed [Asbach et al., 2008]. Instead of one monochromatic excitation, several sinusoidal waves with different frequencies are generated at the same time inside the tissue. One MEG cycle at a given frequency is implemented in the sequence. Several acquisitions with different phase-offsets are required to sample all the waves while satisfying the conditions of the Nyquist-Shannon sampling theorem. A harmonic analysis allows to distinguish the different frequency components and to recover several wave images corresponding to different excitation frequencies.

Merging several MRE acquisitions and separating them using an harmonic analysis is a principle that has been adopted by the technique of multidirectional MRE. Encoding the displacement in the three directions may be useful to provide the inverse problem solver with the most complete information possible about the displacement. Furthermore, as a longitudinal component may sometimes be present, the knowledge of the three displacement components is useful to distinguish the shear wave component from the longitudinal component. In this case, the curl operator is applied to the acquired displacement and the inverse problem is performed on the resulting data set [Sinkus et al., 2005]. In order to acquire the displacement in the three directions, MRE acquisitions are conventionally repeated three times with a different motion encoding direction each time. Recently, the feasibility of encoding in the three directions at once has been demonstrated [Klatt et al., 2013]. Like conventional MRE, several acquisitions are acquired with different delays between MEG and mechanical excitation. However, three MEG are implemented in the three directions and they are shifted with a different delay according to the direction. Hence the wave directional components are not sampled in the same manner which makes possible their distinction after a harmonic analysis. More recently, instead of shifting the MEG, which extends the echo time, it was proposed to rearrange their shape so that their initial phase are different [Kearney et al., 2015].

The addition of a gradient for the motion encoding is one of the major problems in MRE, because the echo time is significantly extended. Fractional encoding solved a part of the issue by reducing its duration but it remains significant. A more radical solution was proposed, that consists in remaining the additional gradient [Bieri et al., 2006, Numano et al., 2015]: the motion encoding is exclusively performed by the readout gradients. This solution allows to save a significant time but the encoding frequency and direction are constrained by the readout parameters and cannot be easily modified.

More standard acceleration methods may also be efficient to reduce acquisition time. The k-space filling optimization in MRE [Murphy et al., 2010] has been the subject of a published study . As it has already been mentioned, several acquisitions with different phase-offsets are required in MRE to perform an harmonic analysis and select only the temporal frequency of interest. The study relies on the assumption that the variability between the different k-space data are not substantially different, because only the phase of the wave varies. The experiments are based on the preliminary observation that the relevant MRE information is included in the center of the k-space. The proposed principle consists in acquiring only a part of the k-space (except on first acquisition) and in using the redundancy of the information on the side of the k-space. Several alternatives are possible, either the first k-space image is completely acquired and information is reused to complete the next incomplete ones (keyhole method), or incomplete data are filled with zero (zero-padding method). MR experiments on the brain were carried out in this study and results indicate that the keyhole method with the acquisition of 16 lines over 256 yields an elasticity error inferior to 10%.

2.2.2 A fast and interactive MRE pulse sequence for interventional MRE

Our all-in-one interventional MRE system must include a dedicated MRE pulse sequence. The sequence must be fast in order to provide an elasticity map refreshed in real-time ($\sim$ 1Hz).

MEG implementation

We have implemented bipolar motion sensitizing gradients on an interactive and fast spoiled gradient echo sequence (Beat-IRT, Siemens Healthcare, Germany). A major advantage of the proposed MRE sequence is its interactivity, which allows changing the monitored image plane dynamically. The operator has the possibility of interactively changing the position and the orientation of the acquired slice without interrupting the acquisition. This is expected to help to the dynamical monitoring of thermal therapy. The MR-pulse sequence chronogram including MEG is shown in Fig.2.10. To reduce the image acquisition time, the repetition time is equal to only one mechanical excitation cycle using a fractional encoding scheme $R = 1$. The movement is encoded in only one direction by one cycle of a bipolar motion sensitizing gradient. A phase difference image is reconstructed from two images with opposite MEG polarities to cancel the constant noise and increase the motion encoding. It is important to emphasize that the proposed method is optimally developed for the real-time monitoring of elasticity changes in interventional radiology, and not for full 3D quantitative biomechanical characterization. Only one excitation frequency and one slice are therefore investigated. Moreover, as previously mentioned, the needle MRE driver generates a well-defined shear wave pattern. Additional steps of acquisition and processing aiming at removing the longitudinal component are therefore not expected to improve substantially the result of the inverse problem. Motion is thus encoded in only one direction, parallel to the needle shaft axis.

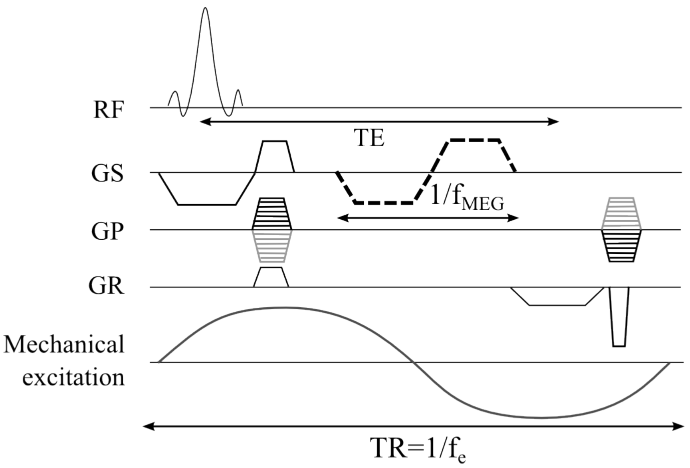

Figure 2.10 – Chronogram of the motion encoding spoiled gradient-echo sequence developed for the all-in-one interventional MRE system.

Optimization of the number of phase-offsets

What takes a long time in MRE is not only the acquisition time of one image but also the need of acquiring several images to reconstruct only one elastogram. MRE experiments reported in the literature use four, eight, or more phase difference images obtained by changing the shift between the mechanical wave and the MEG. The phase-offsets are regularly spaced across a mechanical period. Acquiring several phase offsets enables to apply a temporal Fourier transform and then to select only the displacement induced by the generated shear wave at a given frequency. As opposed to diagnostic MRE, interventional MRE requires a short acquisition time: acquisition speed of all images necessary for one elastogram must be high enough compared with typical elasticity rate of change. We carried out a preliminary experiment to evaluate the relevance of reducing the number of phase-offsets for one elastogram computation. Comparison was performed between elastograms reconstructed using 1 phase-offset only (no temporal Fourier transform) or 3, 4, 6, or 12 phase-offsets. Elastograms were reconstructed using the classic inverse problem solver of the Local Frequency Estimation algorithm that is described in details in the next section 2.3.1. A mechanical wave of 120 Hz was generated with an in-house conventional surface pneumatic exciter in a homogeneous phantom made of gelatin (5%). The designed pulse sequence previously described was used to encode the movement. A set of 240 phase images was collected with 12 phase-offsets evenly spaced across a phase cycle, and two images with opposite MEG polarities for each phase-offset. From this set of 240 images, 10 elastograms were reconstructed after subtracting, unwrapping, and filtering of the temporal Fourier transform for the 12 phase-offsets (Fig.2.11.a). Then, one phase difference image out of two was selected from the entire set to simulate an MRE acquisition with six phase-offsets, yielding 10 other elastograms. This decimation was repeated for simulation of MRE acquisition with four and three phase-offsets, respectively. Finally, 10

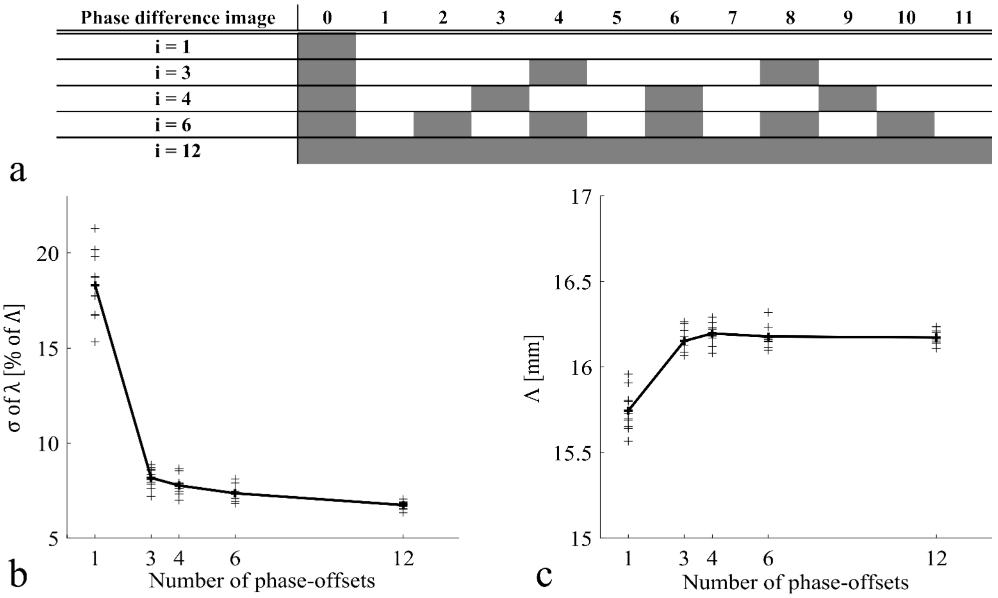

Phase difference image	0	1	2	3	4	5	6	7	8	9	10	11
i = 1	▨											
i = 3	▨				▨				▨			
i = 4	▨			▨			▨			▨		
i = 6	▨		▨		▨		▨		▨		▨	
i = 12	▨	▨	▨	▨	▨	▨	▨	▨	▨	▨	▨	▨

Figure 2.11 – Impact of the number of phase-offsets on the elastogram quality. a)Decimation scheme used for data analysis. One MRE acquisition protocol with 12 phase-offsets evenly spaced across a mechanical excitation cycle provides 12 phase difference images. Different combinations of them are made to simulate acquisition protocols with i phase-offsets ($i = 1$, 3, 4, 6, or 12). b,c) Standard deviation σ and mean Λ of the wavelength λ in the region of interest of each elastogram (cross) and average of the 10 elastograms (line).

other elastograms were reconstructed without applying the temporal Fourier transform using every first difference image of 12 (Fig.2.11a). Relevant parameters of acquisition include: wide bore 1.5 T MRI scanner (MAGNETOM Aera, Siemens, Germany), excitation frequency 120 Hz, MEG frequency and amplitude 290 Hz and 20 mT/m, respectively, encoding direction: phase encoding, axial slice orthogonal to the surface of the pneumatic exciter, slice thickness 10 mm, field of view (FOV) 300 mm × 300 mm, acquisition matrix 128 × 128, repetition time/echo time (TR/TE) 8.33/5.7 ms, flip angle 10° and bandwidth frequency 400 Hz pixel ^{1}. Mean Λ_i^j and standard deviation σ_i^j of wavelength λ were calculated in a large elliptical region of interest (166 mm × 58 mm) on every elastogram j of each data set i. A total of five datasets ($i = 1$, 3, 4, 6, and 12 corresponding to the number of phase-offsets) was obtained after appropriate data decimation. For each data set, 10 elastograms ($j = 1$ to 10) were reconstructed. Data analysis was performed on median filtered (kernel of 4× 4) elastograms, given in terms of wavelength λ[mm]. Analysis of statistical parameters was performed on computed elastograms to evaluate their precision. The average Λ_i of the means and the average σ_i of the standard deviations of each data set i of elastograms ($i = 1$, 3, 4, 6, and 12 corresponding to the number of phase-offsets) are shown in Fig.2.11b-c. The implementation of the temporal Fourier transform allows for substantial improvement of elastogram reliability as shown by the significantly higher mean standard deviation σ of λ obtained for $i = 1$ compared with $i = 3$, 4, 6 or 12. Elastograms obtained using the LFE method are stable between $i = 3$ to 12 phase-offsets. Three phase-offsets allow obtaining results close to those obtained with a conventional protocol with four phase-offsets, but with a 25% reduction in image acquisition time per elastogram. The first idea would be to remove this step and reduce by 75% minimum the acquisition time compared with four phase-offsets. However, this experiment have shown us that removing the temporal Fourier transform suggests a dramatic decrease of the elastogram quality. We therefore propose here a tradeoff to improve acquisition times while preserving the quality of elastograms. Acquiring only three phase-offsets allows us to reduce by 25 % the acquisition time (compared with 4 phase-offsets) without significant loss of the elastogram quality. The chosen number of three phase-offsets is the minimum number required by the Nyquist-Shannon sampling theorem to apply the discrete Fourier transform. Only three phase-offsets are therefore acquired with our interventional MRE system to reduce the total acquisition time of all phase images that will be used to reconstruct one elastogram.

Respiratory triggering

Our first in vivo experiments (described in the next section 3.3) were carried out during one breath-hold. However, thermal ablation procedures typically last up to several tens of minutes. Breath-holding is therefore not appropriate in this case. We therefore refined the sequence to adapt the sequence to free-breathing procedures. Two phenomena coexist: on the one hand, the motion occurring during the acquisition of one image, *intraview motion*, leads to artifacts in the phase image, on the other hand, the potential displacement of structures between two MRE images, *interview motion*, will make useless the phase difference image used to remove the phase background or the temporal Fourier transform used to select the frequency of interest. Indeed, these two processing steps rely on the assumption that there is no macroscopic displacement of structures between acquired images. Fig.2.12 illustrates the phenomena by comparing two magnitude images acquired in different phases of a same respiratory cycle. Respiratory motion is a major issue in MRI of the abdomen. Most of the motion correction techniques require the monitoring of the respiratory motion, which can be done by the use of navigators or pneumatic bellows.

- Navigators require the acquisition of an extra signal coming from a small area that moves during the respiration such as the diaphragm. This acquisition is repeated as often as possible between acquisitions of interest in order to estimate the spatial displacement as a function of time.

- A pneumatic bellows is an elastic belt that is fastened around the patient's abdomen. A pressure transducer is attached to the belt and transmits a signal as a function of the lung expansion and contraction. The signal is processed in real-time and offers a monitoring of the respiratory with a high update rate.

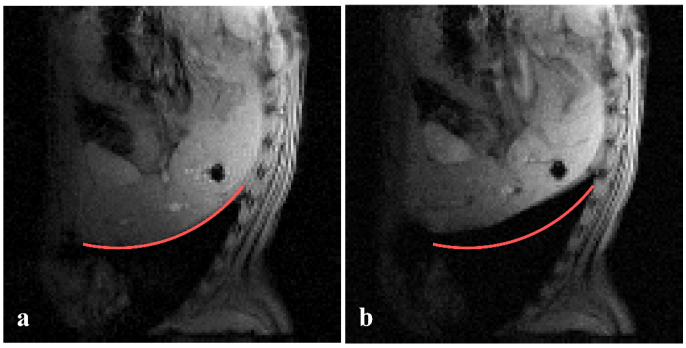

Figure 2.12 – Displacement of structures observed on two images acquired at different times of the respiratory cycle. In order to visualize the displacement, the side of the diaphragm line of (a) is drawn on (b).

Several strategies are available for respiratory motion correction and can be divided in two main groups: *Prospective correction* and *Retrospective correction*. In retrospective correction, images corrupted by motion are corrected after the acquisition. The information provided by navigators can be used to correctly reconstruct images. Based on autocorrelation and data consistency, some other techniques enable the image reconstruction with motion correction without requiring any additional acquisition. The prospective correction consists in compensating the motion during the acquisition. Based on the respiratory cycle monitored in real-time by navigators or pneumatic bellows, the MR pulse sequence can be triggered on the cycle so that the motion is minimal during the acquisition window. Either two time points of the respiratory cycle are specified to open and close the acquisition widow (respiratory gating) or only one time point is selected to open the acquisition window and a fixed number of RF pulses is played (respiratory triggering). Another prospective technique, called view reordering, aims at removing ghosting artifacts while avoiding to increase the total acquisition time but does not reduce image blurring and does not address interview motion issue. More details on respiratory motion correction techniques are available in [Bernstein et al., 2004].

In a first time, we have chosen the simple and efficient solution of respiratory triggering to enable the use of interventional MRE on breathing patients. Respiratory triggering offers the advantage of addressing both intraview and interview motion issues. Besides, this technique does not require change in the image reconstruction algorithm and changes in the sequence design are minimal. Given that the respiratory rate for a healthy adult at rest is typically 12-20 breaths per minute, the interval between two inspirations is approximately 4 seconds. Typical MRE acquisition times obtained with the interventional MRE system are in the order of a second per image without acceleration factor (parallel imaging or partial Fourier). Typical temporal acquisition windows that ensure minimum breathing motion are equal to one-half of the respiratory cycle, corresponding to the expiration phase. As a consequence, the acquisition of two images corresponding to the images

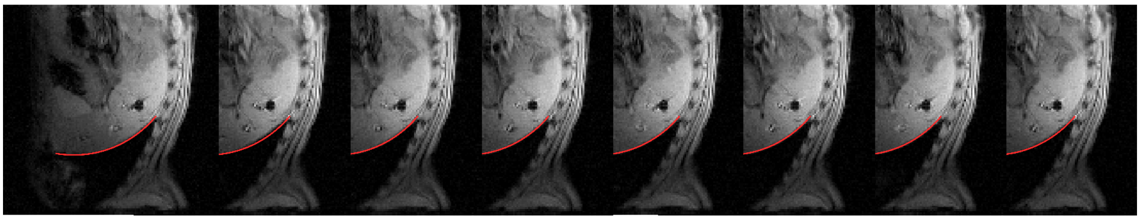

Figure 2.13 – Absence of structure displacement on magnitudes images acquired with respiratory triggering. Two images are acquired per respiratory cycle. In order to visualize the displacement, the diaphragmatic line of the first image(left) is drawn on the following ones.

with opposite gradient polarities would be possible during one respiratory cycle. We therefore implemented the respiratory triggering in the interventional MRE system so that two images used for the phase difference are acquired in the same respiratory cycle. A phase difference image is obtained after each respiratory trigger so that every phase image pair is acquired at the same time of the respiratory cycle. In order to assess the robustness of the respiratory triggering, we carried out an experiment on a swine under ventilation (12 cycles/minute). The acquisition time of one image was set to 1.2 s resulting in a period of acquisition per respiratory cycle of 2.4 s (two images). We compared several magnitude images acquired by the designed sequence. The acquired images are shown in Fig.2.13. The side of the diaphragm of the first image is drawn on the next images and perfectly coincides with the limits of the diaphragm of the other images.

The described sequence modification leads to a new issue, which deserves particular attention. The MRE pulse sequence is based on a spoiled gradient echo sequence that involves a steady-state incoherent imaging. SSI occurs when all transverse magnetization is zero before the next RF pulse. In case of breath holding, images are continuously acquired. Once the steady-state is established, next images are similar in terms of signal amplitude. However, in the case of respiratory triggering, the acquisition of images is interrupted at each respiratory pulse, hence disrupting the steady-state. We have therefore conducted a theoretical study to evaluate the time required to reach the steady-state at each respiratory pulse. The longitudinal magnetization M_z at the end of the $(n+1)^{st}$ repetition time is described as follows:

$$M_z((n+1)T_R) = M_z(nT_R)\cos\theta E_1 + M_0(1 \quad E_1) \qquad\qquad E_1 \equiv e^{\frac{T_R}{T_1}} \tag{2.4}$$

The steady-state is attained in M_{ze} after N excitation pulses and the longitudinal magnetization satisfies :

$$M_z(mT_R) = M_{ze} \qquad m \geq N \tag{2.5}$$

Our objective is to evaluate how many pulses are needed for a tissue magnetization to approach the steady-state. This number is easily estimated at the Ernst angle $\theta_E =$

$\cos\ ^1(E_1)$, where the maximum SSI signal occurs. In this case, it can be demonstrated [Brown et al., 2014] that the number of pulses required to obtain the equilibrium to a given relative error α is:

$$n_\alpha = \left[\frac{T_1}{2T_R}\ln\alpha \quad \frac{1}{2}\right] \tag{2.6}$$

The number of dummy cycles required to reach a steady state at the Ernst angle is calculated with typical MRE parameters of this project and reported in Table 2.1.

α	$T_R[ms]$	$T_1[ms]$	$\theta_E[°]$	n_α
0.01	10	2000 (gelatin)	6	461
0.1	10	2000 (gelatin)	6	230
0.01	10	586 (liver)	10	134
0.1	10	586 (liver)	10	67
0.01	20	2000 (gelatin)	8	230
0.1	20	2000 (gelatin)	8	114
0.01	20	586 (liver)	15	67
0.1	20	586 (liver)	15	33

Table 2.1 – Number of dummy cycle n_α required in different cases. Gelatin and liver T_1 coefficients come from [Unger et al., 1988] and [de Bazelaire et al., 2004] respectively

.

Let us take the example of liver examination at 100 Hz corresponding to a TR of 10 ms with the previously described sequence. Assuming a flip angle equal to the Ernst angle, the steady-state is established at 90% after 67 RF pulses corresponding to 670 ms.

Based on these observations, we adapted our respiratory-triggered MRE pulse sequence in order to ensure that the steady-state is reached at each respiratory cycle. We have therefore included a user-defined number of dummy cycles to the sequence. Every trigger is followed by a judiciously chosen number of dummy cycles and two MRE images with opposite gradient polarities. The phase-offset of the mechanical excitation varies from one respiratory trigger to the next one. The chronology of the events is shown in Fig.2.14.

The respiratory triggering offers the advantage of being robust, efficient and easy to implement. Nevertheless, this option suffers from increased acquisition time that is directly related to the respiratory cycle duration. Retrospective motion correction techniques do not present this drawback but, to our knowledge, no respiratory motion correction algorithm has ever been applied to MRE image series. We have recently started a new project in collaboration with the Lyric laboratory of Bordeaux in order to study the feasibility of applying motion correction algorithm to MRE phase images. This work is still in progress. The investigated algorithm has shown great potential for the monitoring of thermal ablations by thermometry [Ozenne et al., 2015].

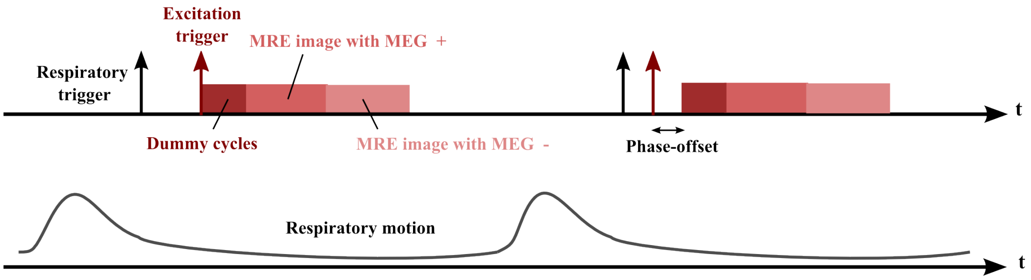

Figure 2.14 – Implementation of the interventional MRE sequence triggered on the respiration. The chronology of the implemented events is represented according to the respiratory motion. After each respiratory trigger, the mechanical excitation is triggered according to the required phase-offset. Then, dummy cycles are played out in order to reach the steady-state. Finally, two images with opposite gradient polarities are acquired.

2.3 Elastogram reconstruction

MRE data processing is the last step to reconstruct an elastogram. Nevertheless, it can be divided in two different stages: the wave enhancement and the inverse problem solving. In this section, the conventional methods are described and the method that we have chosen for our interventional MRE system is presented.

2.3.1 Overview of elastogram reconstruction methods

Wave enhancement

The long duration of the MRE examination essentially arises from the long acquisition time. However, image processing is also a time consuming step. After the acquisition of raw data in the k-space, phase images are reconstructed and preprocessed to enhance the wave image [Li et al., 2014]. First of all, displacements are encoded in the phase of the MRI signal, which is reconstructed within the [-π,π] interval; phase unwrapping methods are therefore applied to recover the true phase (Fig.2.15). This step can be particularly difficult

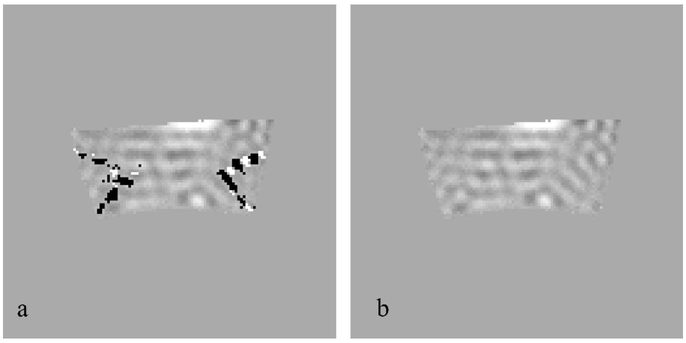

Figure 2.15 – Phase unwrapping on a homogeneous gelatin phantom.Image comparison between without(a) and with (b) phase unwrapping.

because of MRI phase image noise and artifact [Barnhill et al., 2014, Wang et al., 2007, Zebker and Lu, 1998]. Then, as already mentioned, the phase image can be subtracted to a reference phase image acquired without motion encoding gradient in order to remove the constant background. Another solution consists in subtracting two phase images with opposite MEG polarities, which offers the advantage of increasing motion sensitivity by a factor of 2 while removing constant background. If the MRE acquisition is performed with three orthogonal encoding directions, a supplementary mathematical operation can be performed in order to ensure the selection of only the shear component of the wave [Sinkus et al., 2005]. The curl operator is applied to only analyze the shear wave component. The next step consists in applying a temporal Fourier transform on the set of images that were acquired with different delays between the mechanical excitation and the motion encoding. The objective of this processing step is to extract the displacement at the excitation frequency. This step can be completed by the suppression of reflected waves using a directional filter applied in the spatio-temporal frequency domain [Manduca et al., 2003]. Indeed, in this domain, it is possible to distinguish the waves with respect to their propagation orientation but also their propagation direction. Reflected waves can therefore be removed.

Inverse problem solving

The final step consists in computing the spatial distribution of the mechanical properties, often referred to as solving the inverse problem. Direct inversion methods are based on the inversion of the equation (Eq.(1.36)) introduced in the previous chapter. Let us recall the equation under the assumption of a monochromatic sinusoidal excitation.

$$\rho\omega^2\vec{u} = \mu\Delta\vec{u} + (\mu+\lambda)\vec{\nabla}(\vec{\nabla}.\vec{u}) \tag{2.7}$$

The algebraic inversion of the differential equation (AIDE) [Oliphant et al., 2001] is a method to estimate both Lame coefficients. Eq.(2.7) is required to be in a matrix form:

$$A\begin{pmatrix}\lambda+\mu\\ \mu\end{pmatrix} = \rho\omega^2\begin{pmatrix}u_1\\ u_2\\ u_3\end{pmatrix} \tag{2.8}$$

where u_i is the displacement measured in the i-direction.

$$A = \begin{pmatrix} u_{i,i1} & u_{1,ii}\\ u_{i,i2} & u_{2,ii}\\ u_{i,i3} & u_{3,ii}\end{pmatrix}$$

Lame coefficients are given by the inversion of the equation:

$$\begin{pmatrix} \lambda + \mu \\ \mu \end{pmatrix} = \quad \rho\omega^2 (A^* A) \quad {}^1 A^* \begin{pmatrix} u_1 \\ u_2 \\ u_3 \end{pmatrix} \tag{2.9}$$

where A^* is the conjugate transpose of the matrix A. AIDE enables the estimation of both coefficients. Nevertheless, it is difficult to estimate both of them at the same time because of their significant different orders of magnitude. Eliminating λ from the expression is often preferred. The first way to remove λ from consideration is to neglect the term $\lambda(\vec{\nabla}.\vec{u})$ given that displacements due to the longitudinal wave vary slowly. Alternatively, the use of the curl operator to remove the longitudinal component [Sinkus et al., 2005] enables to select only the shear wave component and hence to remove λ from the expression. All these options require the acquisition of the displacement field in the three directions. In order to reduce the acquisition time, the incompressibility of the investigated tissue is often assumed. This assumption allows estimating μ from any single component of motion as described by Eq.(1.41). μ is given by:

$$\mu = \quad \rho\omega^2 \frac{u_i}{\Delta u_i} \tag{2.10}$$

These algorithms involve a division and the calculation of a second derivative. Prior smoothing filters are therefore required to remove the noise and allow a more accurate calculation. A different approach proposed by [Van Houten et al., 1999] is based on an iterative algorithm. In this approach, a solution is iteratively refined by comparing the forward calculations of the displacements from the current solution to the actual measured values. This method avoids the inversion of equations but requires a long computational time. The commercial MRE tool uses another algorithm based on the estimation of the local spatial frequency [Manduca et al., 1996]. By applying the Local Frequency Estimation (LFE) algorithm initially developed in [Knutsson et al., 1994], the local wavelength is computed from the wave image. Under the assumption of incompressibility, local homogeneity and linear elasticity, the shear modulus is then obtained according to the shear wave celerity expression (Eq.(1.42)):

$$C_s = \lambda_s f_e = \sqrt{\frac{\mu}{\rho}}$$

where f_e is the temporal excitation frequency and λ_s is the wavelength. μ is therefore given by:

$$\mu = \rho(\lambda_s f_e)^2 \tag{2.11}$$

The LFE algorithm has proven to be robust and is relatively insensitive to noise. One disadvantage is its limited resolution: at least half of a wavelength must be embedded in the region of interest to accurately measure the local frequency in this region [Manduca et al., 2001]. It is important to highlight that the acquisition of the displacement in only one direction is sufficient to reconstruct one elastogram.

LFE algorithm

In our study, we have chosen to solve inverse problem solver using LFE-based methods. This paragraph is therefore intended to detail the underlying theory behind LFE.

The LFE algorithm relies on estimating the local frequency of an analytic signal. A signal is named analytic if it has no negative frequency component. The analytic signal $f_a(x)$ of any real signal $f(x)$ can be obtained by Hilbert transform. In the frequency domain, the Hilbert transform is defined as follows:

$$F_a(\nu) = \begin{cases} 2F(\nu) & \text{if } \nu \geq 0 \\ 0 & \text{if } \nu < 0 \end{cases} \tag{2.12}$$

with F_a and F are respectively the Fourier transform of f_a and f. The local frequency ν_l of a locally monochromatic signal f is defined as the derivative of the phase of its analytic signal f_a [Boashash, 1992]:

$$\nu_l(x) = \frac{1}{2\pi}\frac{d\phi(x)}{dx}\text{with } f_a(x) = a(x)e^{\phi(x)} \tag{2.13}$$

Fig.2.16 illustrates the local frequency of a signal. The local frequency estimation algorithm is based on the use of lognormal filters R_i described by:

$$R_i(\nu) = e^{\ C_B \ln^2(\frac{\nu}{\nu_i})} \tag{2.14}$$

where ν_i is the central frequency of the filter, $C_B = \frac{4}{B^2 \ln(2)}$ with B the $6dB$ bandwidth of the filter. It can be shown that applying separately two carefully chosen filters to the signal enables to recover the local frequency in every point according to the following expression:

$$\nu_l = \sqrt{\nu_i \nu_j} Re \left(\frac{r_j * f}{r_i * f} \right) \tag{2.15}$$

with r_i and r_j are respectively the inverse Fourier transform of R_i and $R_{referencej}$. Filters must be chosen so that $\nu_j = \nu_i e^{\frac{1}{2C_B}}$. The LFE principle is summarized in Fig.2.17. It must be emphasized that the local frequencies to be estimated must be included in the bandwidth of the filters. The *a priori* knowledge of the local frequencies of the input signal is therefore required. However, the use of several pairs of filters covering a large bandwidth allows circumventing this issue. The final local frequency estimation is a weighted average of all the estimations returned by every pairs according to the spectral density of each output. The method can be extended to 2D data. In this case, filters are the products of

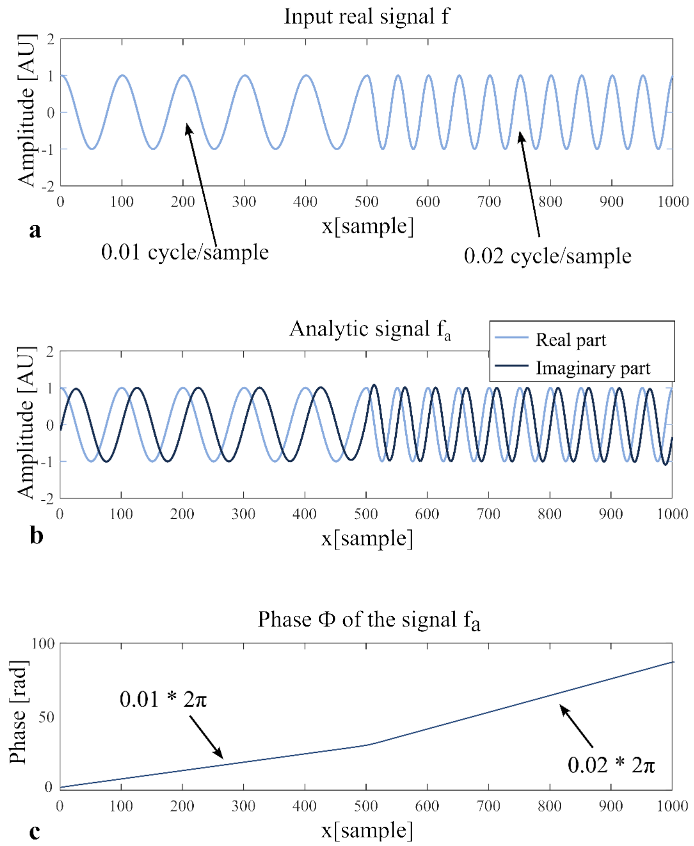

Figure 2.16 – Illustration of the local frequency. A real signal (a)composed of two parts with different frequencies is subjected to the Hilbert transform to obtain the analytic signal (b) with a real and an imaginary part. c)The derivative of the analytic signal phase is related to the local frequencies of the input signal.

a radial component and a directional component. The radial component takes the form described in Eq.(2.14) and the directional component is defined by:

$$D_k(\vec{u}) = \begin{cases} (\vec{u}.\vec{n_k})^2 & \text{if } \vec{u}.\vec{n_k} > 0 \\ 0 & \text{otherwise} \end{cases} \tag{2.16}$$

where $\vec{n_k}$ is the filter directing vector. A complete map of local frequencies is obtained by summing the outputs of orthogonal filters as shown in Fig.2.18.

2.3.2 Interventional MRE data processing

Real-time data processing

Interventional MRE requires a fast data processing in order to provide radiologists with information in real-time. We have implemented the elastogram reconstruction from MR phase images in real-time. Every acquired image are transferred to an external computer in

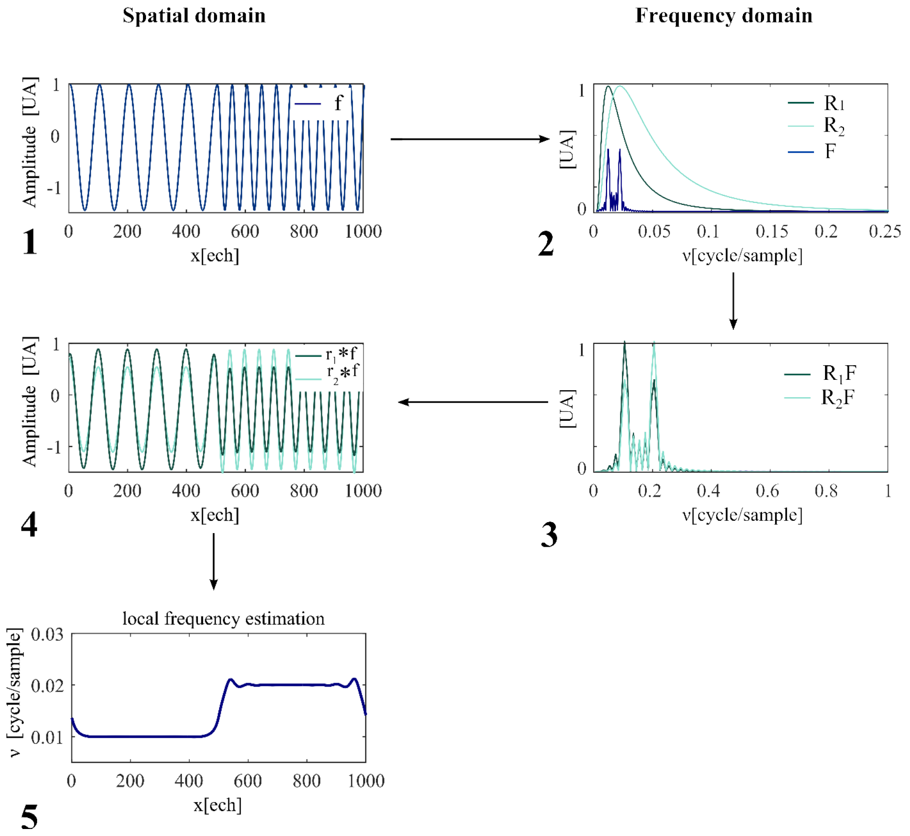

Figure 2.17 – Example of LFE algorithm on theoretic 1D signal. The real input signal (1) is subjected to the Fourier transform (2). Two lognormals filters R_1 and R_2 are adequately chosen to include in their bandwidth the frequencies of the input signal. Both filters are applied separately to the signal in the frequency domain (3). The inverse Fourier transform of the result returns two distinct signals (4) in the spatial domain. The quotient of the outputs allows to recover the local frequencies of the input signal (5).

real-time through TCP/IP connection. Phase images are processed in Matlab (Mathworks Inc., Natick, MA). First, a 2D phase unwrapping algorithm [Goldstein et al., 1988] is applied on phase difference images. A temporal fast discrete Fourier transform is performed on each pixel of a set of unwrapped phase difference images, corresponding to a complete mechanical excitation cycle to select the frequency of interest. Finally, a LFE-based algorithm with 10 lognormal quadrature filter pairs spatially oriented in four directions (two orthogonal directions, two opposite directions) estimates the local wavelength from the complex resulting wave image. Current online processing time is 1.2 s per phase difference image, which allows a real-time display of the elastogram with a constant delay of 1.2 s after the last phase image is reconstructed by the scanner. The image transfer time is negligible compared to image acquisition time.

In order to evaluate the accuracy of the implemented algorithm associated to the designed sequence and the excitation device, we carried out a preliminary study on a gelatin phantom. The validation of the results in MRE is challenging because the ground truth is often

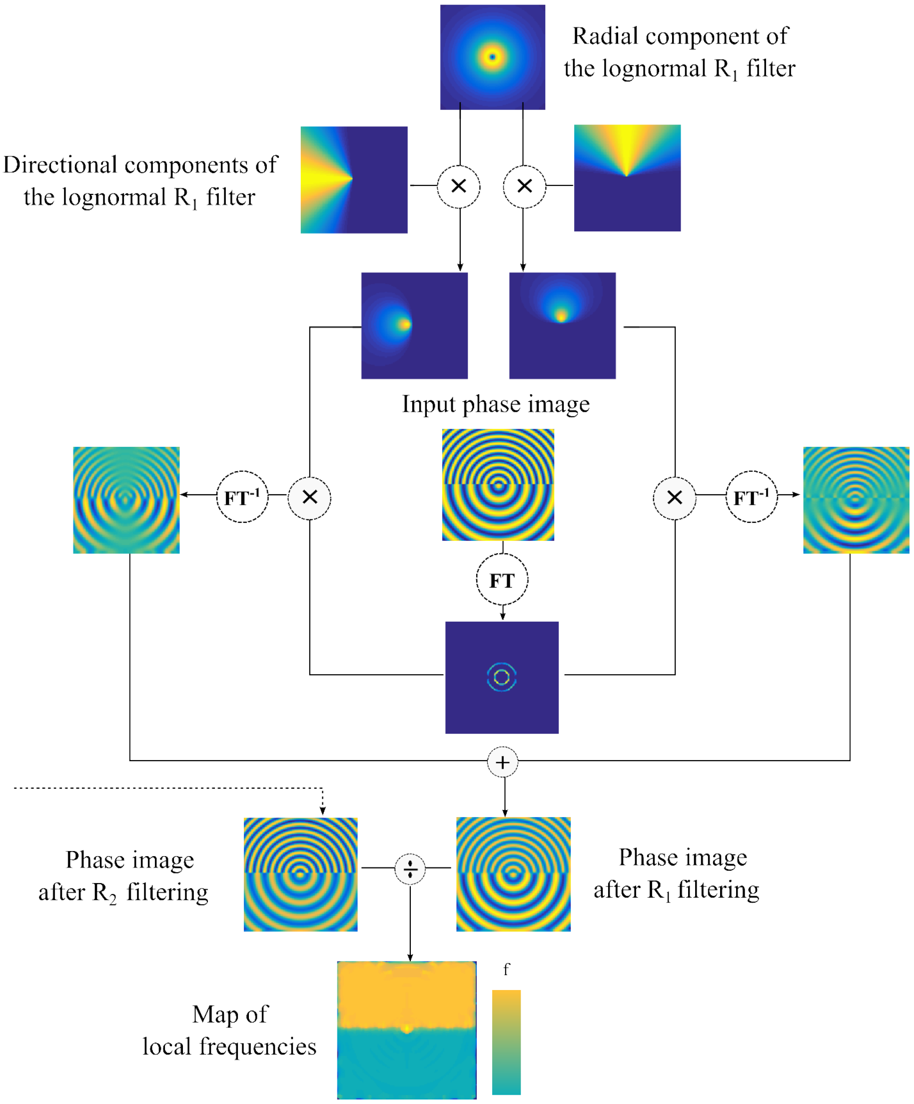

Figure 2.18 – LFE principle in 2D. Orthogonal lognormal filters with a radial component and a directional component are applied to the input signal in the frequency domain. The quotient of the images obtained by each filter R_1 and R_2 yields a map of local frequencies of the input image. In the frequency domain the magnitude of the complex images are shown. In the spatial domain the real part of the images are shown.

unknown. We have chosen to compare the elasticity values obtained with this protocol to those measured by rheometry (Thermo Scientific HAAKE MARS III, Rheology Solutions, Bacchus Marsh, Australia). Small cylindrical samples (20 mm in diameter , 3mm in height) were extracted from the phantom for a shear rotating Dynamic Analysis in parallel-plate configuration under controlled temperature (22.5°). The same phantom was subjected to MRE acquisition with the sequence previously described with 3 phase-offsets and a pair of images with opposite MEG polarities at each phase-offset. Different excitation frequencies were tested in MRE with the first version of the needle MRE driver (60 Hz, 80 Hz and 120

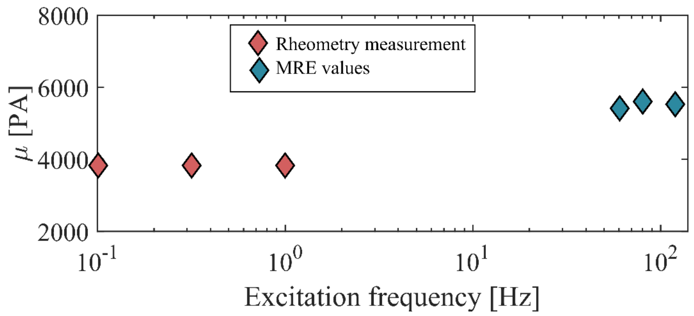

Figure 2.19 – Comparison of elasticity measurements by MRE and rheometry on a gelatin phantom.

Hz) and with the rheometer (0.1 Hz, 0.3 Hz and 1 Hz). Elastograms were computed with the home-made LFE algorithm. Results are shown in Fig. 2.19. Values are in the same order of magnitude. However the difference between rheometry values and MRE values can not be neglected. Nevertheless it must be emphasized that the range of excitation frequencies is totally different between the two measurement techniques, which makes difficult the comparison.

Improvement of the update rate

Using MRE for interventional MRI requires faster flow of information. We have chosen to implement the concept of sliding window to our interventional MRE system. The sliding window allows the reconstruction of an elastogram with every newly acquired pair of images with opposed MEG polarity (Fig.2.20). Let α be the phase shift between the mechanical excitation and the motion sensitizing gradient, $\alpha = \frac{2n\pi}{N}, n = 1...N$ with N the number of phase-offsets. The first elastogram is computed from N phase difference images as in conventional MRE, and then the second one is reconstructed from the $N - 1$ previous phase difference images and the most recent one. Hence, one elastogram is reconstructed with every new available phase difference image. The elastogram update rate is as high as the one obtained with the one-phase-offset acquisition protocol but with the benefit of the temporal Fourier transform. As mentioned before, the pulse sequence used here allows us to interactively change the position and orientation of slices. If such a change occurs, the algorithm is able to detect it and to restart to provide the first elastogram for the new slice (as illustrated by slice $n + 1$ in Fig.2.20). Elastograms are displayed on the external computer after median filtering. Any change of orientation or position of the slice results in a waiting time before the next elastogram display corresponding to the acquisition of 3 phase-offsets, each one with two opposite MEG.

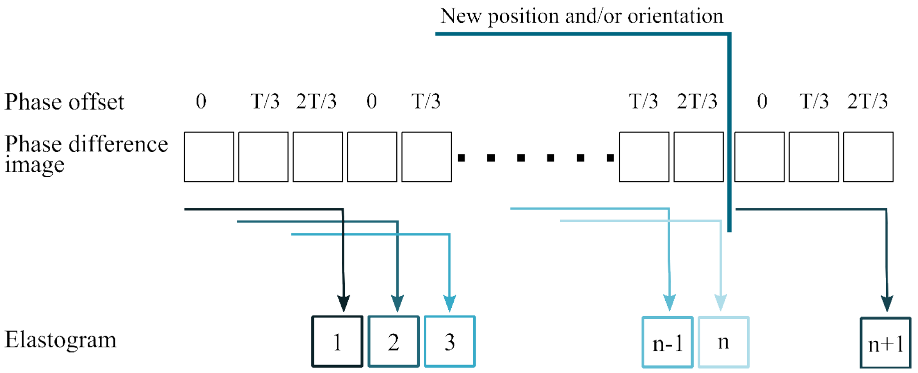

Figure 2.20 – Sliding window scheme for the elastogram reconstruction in interventional MRE, here in the case of 3 phase-offsets. One elastogram is obtained by using two previous phase-difference images and the new one. Hence a refreshed elastogram is provided with every new phase-difference image. If a change in slice position or orientation occurs, three new phase-offset difference images are required to provide the new elastogram.

2.3.3 Simultaneous thermometry and elastography

The more information is provided during the thermal ablation, the more the monitoring is accurate. It has been shown that MR thermometry can be performed with MRE images [Le et al., 2006]. Simultaneous thermometry and elastography is then developed in the interventional MRE data processing algorithm.

In MRE, two phase images with opposite gradient polarities ϕ_+ and ϕ_- are acquired at each phase-offset:

$$\begin{cases} \phi_+ = \phi_T + \phi_M + \phi_0 \\ \phi_- = \phi_T - \phi_M + \phi_0 \end{cases} \tag{2.17}$$

where ϕ_0 is the background phase. Instead of subtracting the two phase images as it is performed in MRE $\phi_M = \frac{\phi_+ - \phi_-}{2}$, the two images are added in order to cancel the phase shift ϕ_M caused by motion. Only the phase shift ϕ_T caused by temperature changes is left.

$$\phi_T + \phi_0 = \frac{\phi_+ + \phi_-}{2} \tag{2.18}$$

A reference temperature map ϕ_{Tr} is acquired before starting the thermal ablation.

$$\phi_{Tr} + \phi_0 = \frac{\phi_+ + \phi_-}{2} \tag{2.19}$$

During the thermal ablation, this reference image is subtracted to every phase images resulting from the addition:

$$\Delta\phi_T = (\phi_T + \phi_0) - (\phi_{Tr} + \phi_0) = \phi_T - \phi_{Tr} \tag{2.20}$$

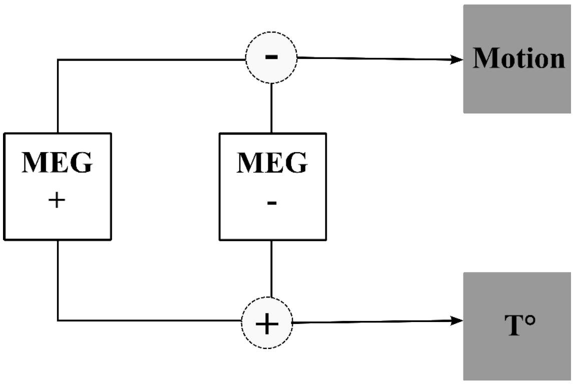

Figure 2.21 – Simultaneous thermometry and elastography. The phase shift due to motion is obtained by subtracting the two phase images with opposite MEG polarities. The phase shift due to temperature changes is obtained by adding them.

Based on the PRF principle (described in 1.2.6), a map of temperature changes ΔT can be computed from the resulting image.

$$\Delta T = \frac{\Delta\phi_T}{\alpha\gamma TEB_0} \tag{2.21}$$

with TE being the echo time. It must be emphasized that no supplementary acquisition is required to compute both temperature and elasticity maps with this method (Fig.2.21). Given that the thermometry will be performed over all the duration of the thermal ablation, another phenomenon must be taken into account: the drift of the external magnetic field. The variation over time of the external magnetic field may arise from the superconductive current, the drift of the shim currents and the radiofrequency and other physical phenomena. In a published study [Depoorter et al., 1994], a phase shift of 800° was reported over a period of 11 hours while no temperature changes occurred. The phase drift occurring during the total duration of the thermal ablation is not negligible and the phase shift due to the drift may result in a wrong temperature measurement. In order to circumvent this issue, the phase shift of a region where the temperature is assumed to be stable is measured. This phase shift is also subtracted to the phase shift obtained in Eq. (2.20). The resulting phase shift only depends on the phase shift due to temperature changes.

2.4 Conclusion

In this chapter, our interventional MRE system dedicated to the monitoring of MRI-guided percutaneous procedures, was described. Ultimately, this method aims at providing a new biomarker for monitoring thermal ablations in real-time. This dedicated MRE protocol consists of 1/ a needle MRE driver that generates a well-defined shear wave directly in the region of interest regardless of its depth, 2/ an interactive real-time motion sensitizing pulse sequence that encodes the displacement on phase images in a short acquisition time, and 3/ online reconstruction that provides an elastogram with every new phase difference image. We have carried out some experiments to validate the complete system. Materials and methods of these experiments are detailed in the next chapter and the results are discussed.

Chapter 3

Real-time monitoring with the interventional MRE system

> " *Je sais pourquoi tant de gens aiment couper du bois. C'est une activité où l'on voit tout de suite le résultat.* "
>
> Albert Einstein

Contents

The previous chapter was dedicated to the description of the developed interventional MRE system. Several experiments were carried out to evaluate the feasibility and the relevance of interventional MRE. This chapter is intended to present the results of the different experiments. All experiments were performed in a wide bore 1.5T MRI scanner (MAGNETOM Aera, Siemens, Germany).

3.1 Monitoring of the gelification of gelatin

3.1.1 Materials and methods

We have designed a first experiment in order to evaluate the capability of observing changes in elasticity in real-time within a region of interest in a gelatin phantom. An approximately 4 cm hole in diameter was scooped out from a homogeneous gelatin phantom (8 %) (Fig.3.1). The needle MRE driver (first version) was inserted vertically in the phantom and held by a Plexiglas structure in order to avoid gel damage during the experiment. A few minutes before the acquisition, a small volume (200 mL) of gelatin (10 %) was prepared and cooled down. Once the temperature reached 22°C, the liquid was poured in the hole of the phantom and its solidification was monitored using real-time MRE during 30 minutes. Relevant imaging parameters include: excitation frequency 100 Hz, MEG frequency 210 Hz, MEG amplitude 20 mT/m, encoding direction: through slice, one slice orthogonal to the needle MRE driver, slice thickness 10 mm, FOV 350 mm×350 mm, acquisition matrix 128×128, TR/TE 10/7 ms, flip angle 15° and bandwidth frequency 380 Hz pixel ^{1}. As described in the previous chapter (Section 2.2.2), 3 phase-offsets each with 2 opposite MEG polarities were used. After initial calculation, a new elastogram was provided every 2.56 s with every new phase-offset pair.

3.1.2 Results

Phase images acquired at different time steps of the experiment are shown in Fig.3.2. It is important to emphasize the circular wave pattern obtained around the needle. The amplitude of the wave fronts can be estimated from the wave images. The first one is estimated to 24 μm in peak-to-peak amplitude. The wave amplitude u_0 decreases with respect to the distance r from the source ($u_0(r) = \frac{u_0(0)}{\sqrt{r}}$, as explained by the geometrical attenuation of cylindrical waves)(Fig.3.3). The wave pattern was visible in the inclusion a few minutes after filling the hole with 10 % gelatin. Changes in the wave pattern could be clearly seen over time within the inclusion, corresponding to the cross-linking process of the gelatin, which could also be seen in the corresponding elastograms. Two circular regions of interest were selected, one inside and one outside the inclusion (12 mm in diameter). Means and standard deviations of the shear modulus in the two regions of every computed elastogram are plotted as a function of time for these two regions of interest (Fig.3.4). As expected, the shear modulus of the surrounding gel was found to

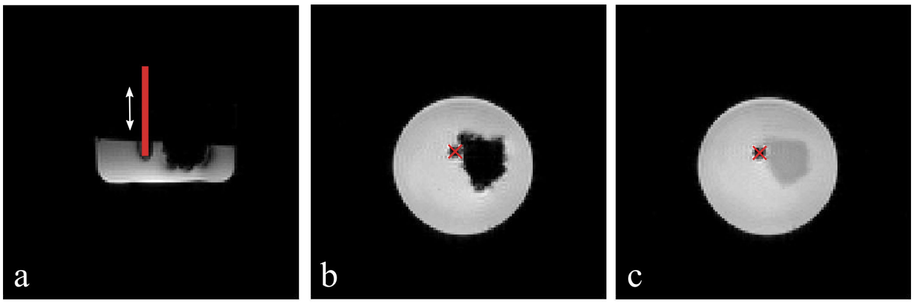

Figure 3.1 – MR images of the gelatin phantom used to monitor the gelification. a-b) Axial and coronal slice of the homogeneous gelatin phantom showing the 4 cm diameter hole. The needle axis is schematically illustrated as a red line or a cross. c) Coronal slice of the phantom just after filling the hole with the liquid 10 % gelatin.

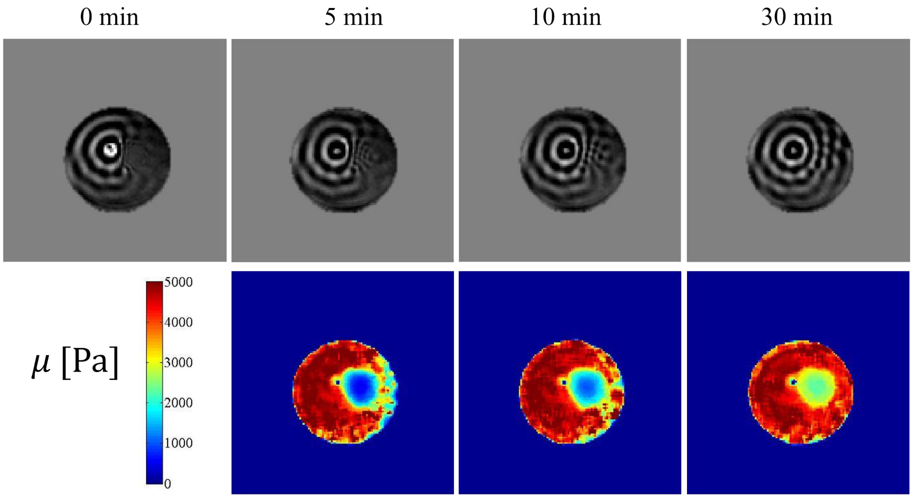

Figure 3.2 – Evolution of the wave propagation (top row) and corresponding elastograms (bottom row) during the solidification of the gelatin in the inclusion. The gelation process can be clearly seen in both wave images and elastograms.

be constant around 5 kPa. For a few minutes, the inclusion was liquid and no wave could propagate through it, as illustrated in Fig.3.4a from 0 to 200 s. Values obtained for the standard deviation were very high and not repeatable during these first 200 s, as it would be expected because of the absence of shear waves. After 200 s, waves with a small wavelength were observed, corresponding to a dramatic decrease of the standard deviation of μ, and reliable values of shear modulus were obtained. Then, the wavelength in the inclusion increased consistently over time and the interventional MRE method was able to evaluate the variation with a mean standard deviation in the inclusion around 2% of the averaged shear modulus. Significant changes in elasticity could be precisely observed as illustrated by the short temporal window of 2 minutes (Fig.3.4b). This experiment shows the capability of interventional MRE to monitor the temporal evolution of the elasticity of a phantom during its gelation with good accuracy and high frame rate. Although the

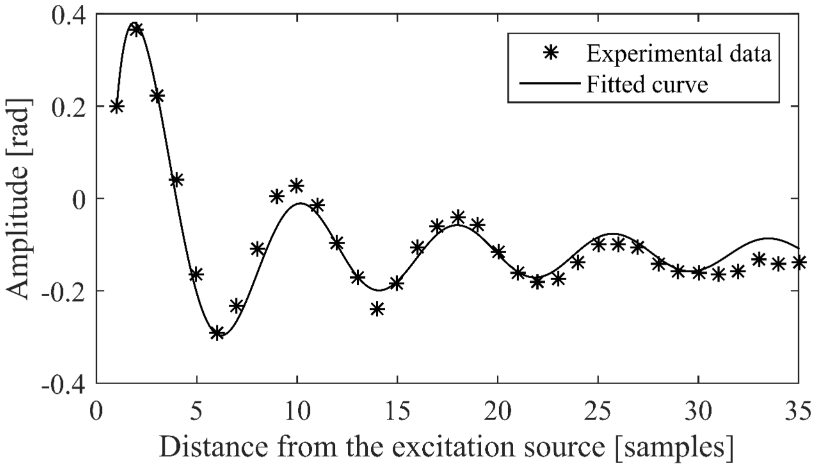

Figure 3.3 – Geometrical attenuation of the wave in gelatin. The solid line, which is described by the expression $f(x) = \frac{a}{\sqrt{(x)}} \sin(bx + c) + d$ with a,b,c,d $\in \mathbb{R}$ is overlaid onto the measured phase profile with a goodness of fit of $R^2 = 0.9533$.

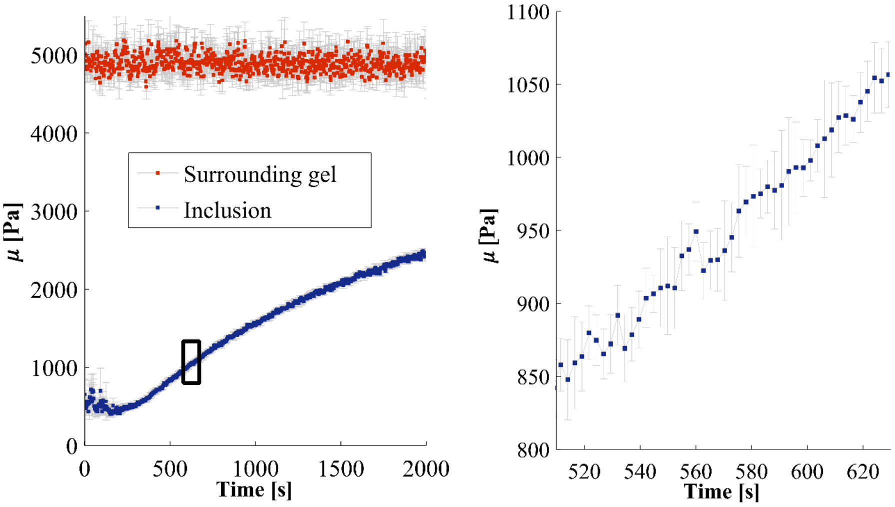

Figure 3.4 – Evolution of the shear modulus in the inclusion of 10 % gelatin during its gelation (in blue) compared to the surrounding gelatin (in red). The graph on the right is obtained by zooming in the time window represented by the black rectangle. Standard deviations in each ROI are drawn in gray.

kinetics involved in this experiment are slow compared to change rate of elasticity expected during thermal ablations, results prove that the method allows to finely monitor elasticity changes.

3.2 Ex vivo monitoring of a laser ablation

3.2.1 Material and method

In order to evaluate our method under more realistic conditions of real thermal ablation, we have performed a laser ablation in an swine liver ex vivo. Elasticity and temperature changes were monitored over time. The laser ablation was performed with a diode laser (DIOMED 25) with a wavelength of 805 nm. Three fibers were inserted in the liver to create a larger lesion. Fibers were approximately spaced of 0.8 cm and were inserted perpendicularly to the needle MRE driver (Fig. 3.5). A total power of 11.25 W was delivered through the three fibers over a period of 10 minutes. The needle MRE driver (first version) was inserted at 2 cm from the tips of the fibers. Relevant imaging parameters are the following: excitation frequency 60 Hz, MEG frequency 130 Hz, MEG amplitude 20 mT/m, encoding direction: through slice, one slice orthogonal to the needle MRE driver, slice thickness 10 mm, FOV 300 mm×300 mm, acquisition matrix 128×128, TR/TE 16.67/9.34 ms, flip angle 15° and bandwidth frequency 795 Hz pixel ^{1}. The total acquisition time for one elastogram was 12.8 s and the update rate was 4.27 s thanks to the sliding window. After the ablation of 10 minutes, the laser was turned off but MRE acquisitions continue for another 10 minutes in order to monitor tissue changes during the cooling process.

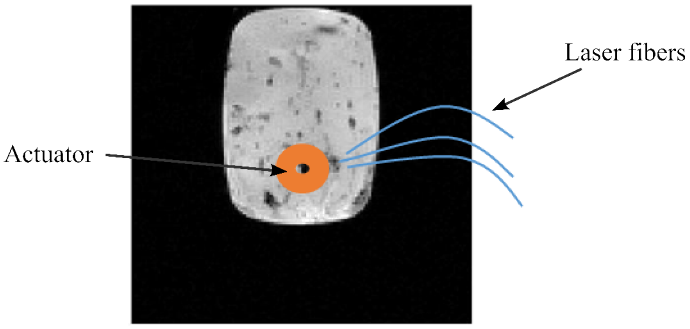

Figure 3.5 – Setup of the ex vivo experiment illustrated on a magnitude MR image. A liver is placed in a bath. The needle MRE driver is placed on the top and laser fibers are inserted close to the actuator.

3.2.2 Results

A circular wave propagating around the needle can be clearly seen. In these conditions, the amplitude of the first wave front was estimated to 18 μm in peak-to-peak amplitude. The second wave front is almost invisible, which is probably due to a high viscosity of the sample. Phase difference images acquired during the ablation are shown in Fig.3.6 with the associated elastograms reconstructed in real-time. The wave pattern is increasingly

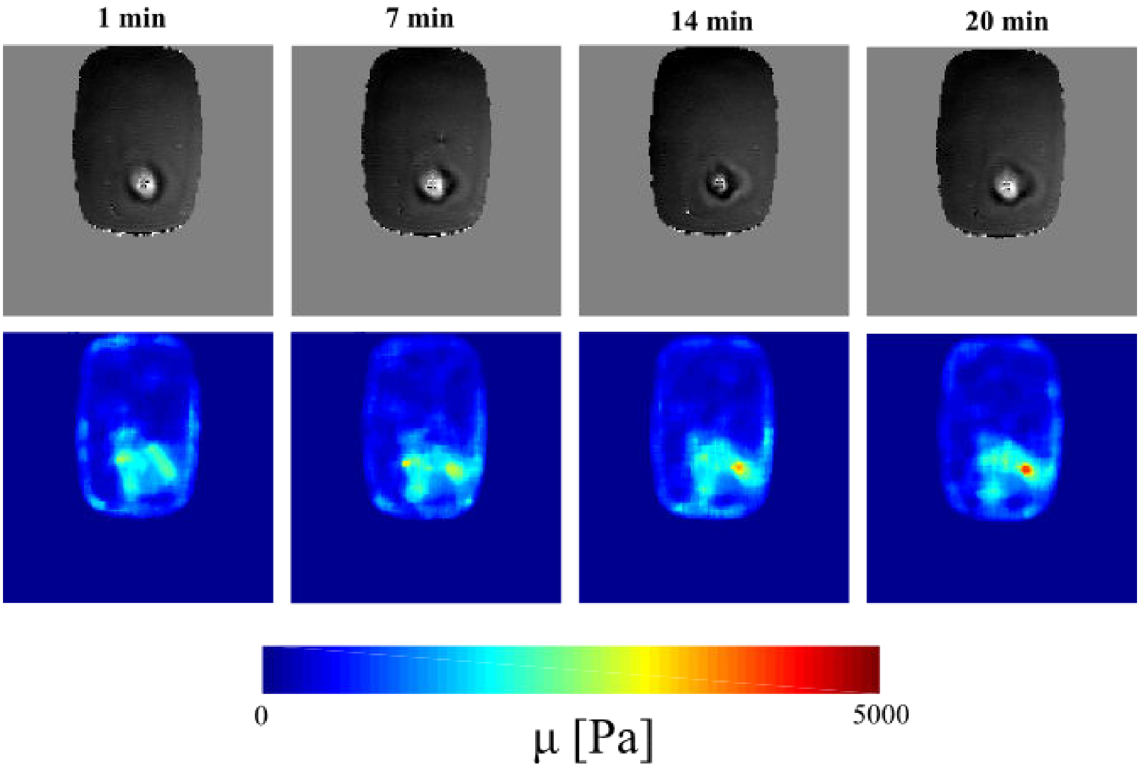

Figure 3.6 – Temporal evolution of the wave propagation (top row) and corresponding shear modulus μ in elastograms (bottom row) during the laser ablation of a swine liver ex vivo.

distorted on the right of the needle MRE driver corresponding to the increase of the shear modulus in the elastograms. The location of the region is consistent with the position of the fiber tips and the lesion observed in Fig.3.7 after the experiment.

The evolution of the shear modulus and the temperature in the lesion are plotted in Fig.3.8. The interval between two measurement points is 4.27 s. At the beginning , a small shear modulus decrease is observed on the graph and then, the shear modulus continuously

Figure 3.7 – Picture of the lesion (white arrow) obtained by laser ablation in a swine liver ex vivo.

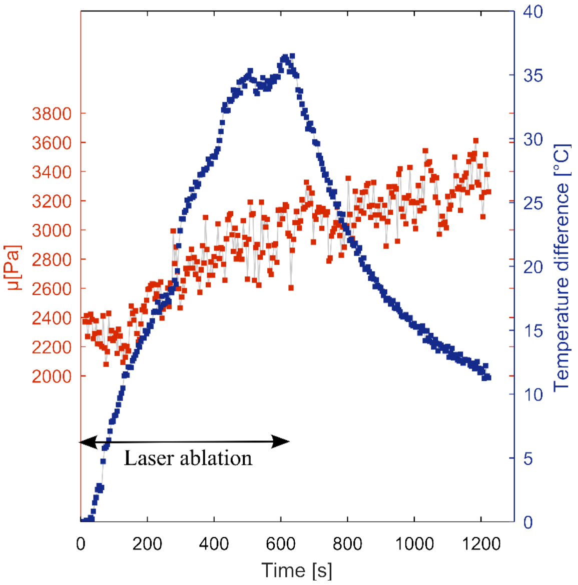

Figure 3.8 – Evolution of the shear modulus (in red) and the temperature (in blue) during a laser ablation in swine liver ex vivo.

increases. It must be emphasized that, in this experiment, the shear modulus still increases after the laser is turned off: the temperature goes down but the shear modulus still increases over the next 10 minutes.

This experiment shows the feasibility of monitoring a thermal ablation with interventional MRE. The results of this experiment highlight the distinction between temperature and elasticity that do not evolve in the same manner during the ablation. This observation attests the relevance of a double monitoring by thermometry and elastography.

3.3 Assessment of in vivo stability and feasibility

3.3.1 Material and method

A feasibility experiment was performed on one porcine subject (35.2 kg) in vivo. Our objective was to demonstrate the feasibility of obtaining elastograms in real-time with interventional MRE in vivo and to evaluate the stability of the method. In a first time, experiments were carried out under one breath-hold. The respiratory triggering is not used in this experiment in order to evaluate the feasibility of interventional MRE in optimal conditions. This experiment was approved by the local ethics committee (ICOMETH C2EA - 38). The animal was anesthetized (propofol 3 mg/kg, pancuronium 0.2 mg/kg and isoflurane 2 %) and placed in the large bore 1.5 T scanner with a 4-channel flex coil on the abdomen and the spine coil. The needle driver (first version) was inserted by an experienced interventional radiologist inside the liver under MRI-guidance and hand-held during the MRE experiment. Relevant parameters of acquisition include: excitation frequency 100 Hz, MEG frequency 160 Hz, MEG amplitude 20 mT/m, encoding direction: through slice, one slice orthogonal to the needle MRE driver (as shown in Fig.3.9a-b), slice thickness 10 mm, FOV 300 mm×300 mm, acquisition matrix 128×128, TR/TE 10/7.9 ms, flip angle 15°, and bandwidth frequency 795 Hz pixel ^{1}. The total acquisition time for one MR-image was equal to 1280 ms. Six images corresponding to 3 phase-offsets each with 2 opposite MEG polarities were used for the reconstruction of one elastogram. The total acquisition time of the complete data set for one elastogram was equal to 7.68 s. Using the sliding window scheme, elastograms were provided in 2.56 s with every new phase difference image obtained. Elastograms showing the shear modulus were displayed in real-time on the external computer after median filtering (kernel of 8×8). In order to evaluate the stability of the proposed method, a single breath-held experiment was performed during 85 s, during which 31 elastograms were reconstructed. For each elastogram, the shear modulus was averaged within a region of interest of 8 mm in diameter.

3.3.2 Results

The needle MRE driver works as a cylindrical source of shear waves: circular wave fronts around the needle shaft were visible on the unwrapped phase difference image (Fig.3.9c). Elastograms at 100 Hz were reconstructed within a circular region around the needle (85 mm in diameter, Fig.3.9d). The amplitude of the first wave front in these conditions was estimated to 30 μm in peak-to-peak amplitude. It can be noticed that the wave is also rapidly attenuated but the elastogram can be reconstructed in the region of interest. Elastogram reconstruction was not performed within the zone corresponding to the needle artifact. The first elastogram was displayed after 7.68 s and refreshed every 2.56 s using the sliding window elastogram calculation method. Fig.3.9e shows the shear modulus for each one of the 31 elastograms. The shear modulus averaged among the 31 elastograms was found equal to 3.5 kPa, and the standard deviation of the mean was equal to 150 Pa. This experiment assesses the stability of the protocol in vivo under breath-hold. A standard deviation of less than 5% of the measured shear modulus was found. Results also allow us to demonstrate the possibility of reaching deep-lying regions with relatively high frequencies (100 Hz).

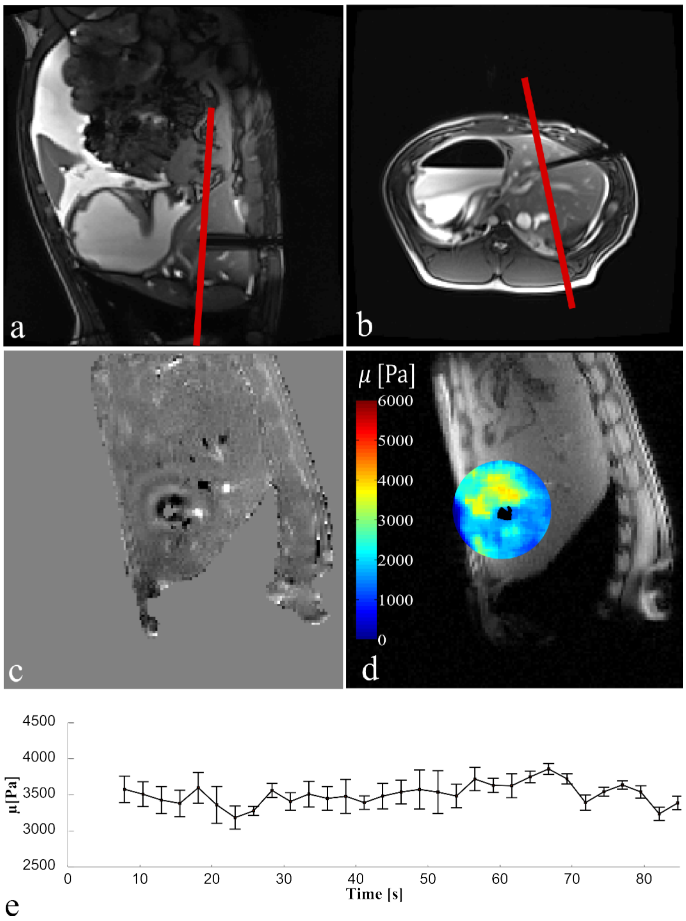

Figure 3.9 – In vivo experiment in the liver of a swine. a) Coronal and b) axial slices aligned to the needle shaft. MRE imaging plane is represented in red. c) Phase difference image acquired with the motion sensitizing pulse sequence. d) Elastogram reconstructed by the algorithm in real-time overlapped on the magnitude image. Elastogram is displayed only in the region located around the needle (85 mm in diameter). e) Stability of in vivo measurements in a region of interest (8 mm in diameter) during one breath-hold of 85 seconds.

3.4 Monitoring of a laser ablation in vivo

3.4.1 Material and method

Experiment A

Since the stability and the robustness of the method were assessed in vivo, we have carried out other experiments to evaluate the capability of the designed system to detect elasticity changes in real-time. A thermal laser ablation was performed on a swine liver in vivo and was monitored in real-time over 20 minutes. This experiment was approved by the local ethics committee (ICOMETH C2EA - 38). The animal was anesthetized (propofol 3 mg/kg, pancuronium 0.2 mg/kg and isoflurane 2 %). The long duration of the procedure prevents to perform it under breath-holding conditions. The animal was continuously ventilated with a respiratory rate of 12 breaths per minute. A respiratory belt was placed on the abdomen in order to monitor the breathing and in order to allow the triggering on the respiratory cycle. The loop coil was added around the second version of the needle MRE driver in order to improve the signal while preserving space for the 4 needles used for the insertion of the fibers. The same laser ablation device as the one used in the ex vivo experiment was used (DIOMED 25). Four optical fibers were inserted in the liver close to the needle MRE driver by an experimented interventional radiologist. A 3D-printed device was used to make the insertion of the four needles easier and ensure the repeatability of the protocol. Thanks to this guiding tool, the fibers were parallel and inclined with 15° to the axis of the excitation needle. A total power of 12 W was delivered through the fibers during 10 minutes. Acquisitions were performed with the interventional MRE sequence triggered on the respiratory cycle (Section 2.2.2). The mechanical excitation frequency was set to 60 Hz, which results in a TR equal to 16.67 ms. According to Eq.(2.6), at the Ernst angle 40 dummy cycles were required to reach the steady-state at 10% at each respiratory cycle. The flip angle was set to 13 °. Each respiratory trigger was therefore followed by a mechanical excitation trigger, 40 dummy cycles and two phase images with opposite gradient polarities. The shift between the respiratory trigger and the mechanical excitation trigger was adjusted so that three phase-offsets covering one mechanical period were acquired every three respiratory cycles. The acquisition matrix was equal to 102 × 128 and parallel imaging was used with a factor 2 which resulted in 1 s for the acquisition of one image. The dummy cycles and the acquisition of the two images were performed in 2.76 s corresponding to 55 % of the respiratory cycle. Other relevant MRI parameters were: MEG frequency 90 Hz, MEG amplitude 20 mT/m, TE/TR 9.34/16.67 ms, through slice encoding, one slice orthogonal to the needle MRE driver.

Experiment B

The same experiment was performed on another animal (Fig.3.10). The protocol was exactly the same except for the fiber orientation. In this case, the fibers were perpendicular to the needle MRE driver (Fig.3.11).

3.4.2 Results

Experiment A: Stability of the protocol

First, the stability of the protocol was assessed by acquiring images during 10 minutes before the insertion of the fibers. The circular wave pattern around the needle was observed. The amplitude of the first wavefront was estimated to 35 μm in peak-to-peak amplitude. Again, less than three wavefronts were visible, which was probably due to the high viscosity of the liver. Elastograms were reconstructed in the region where the wave was propagating and the shear modulus was measured to 1400 Pa ± 70 Pa. A standard deviation less than

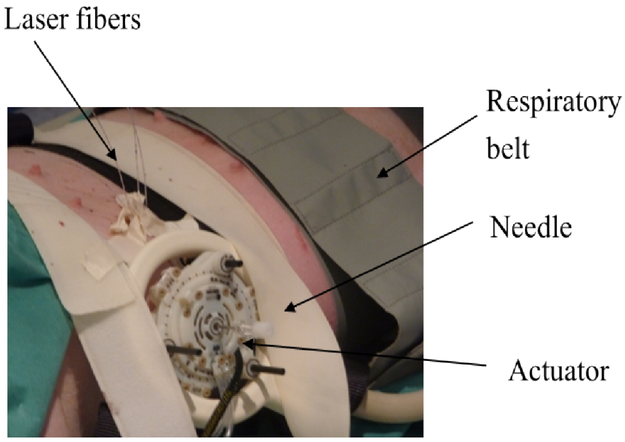

Figure 3.10 – Setup of the in vivo experiment. A respiratory belt is used to synchronize the mechanical excitation and the respiration. A needle is inserted in the center of the mechanical actuator. A loop coil is placed around the actuator. 4 laser fibers are inserted close to the needle MRE driver.

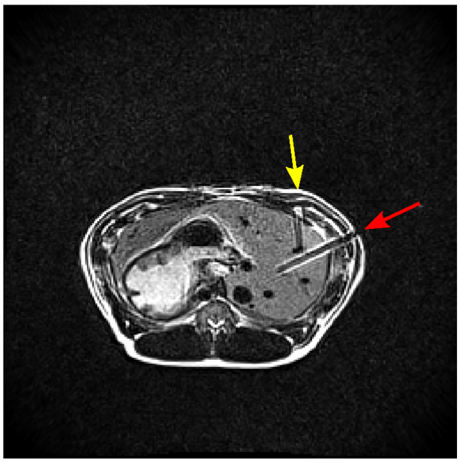

Figure 3.11 – T2w-image of the swine liver before ablation. 4 laser fibers (yellow arrow) are inserted in parallel to create a lesion in the liver. The needle MRE driver (red arrow)is inserted so that the ablated region is covered by the mechanical wave propagation, allowing the measurement of elasticity changes during the ablation.

5% in a region of interest of 10 pixels was observed over the 127 elastograms.

After inserting the fibers, the laser ablation was monitored in temperature and elasticity with the described protocol. Elasticity and temperature were measured from images acquired during 20 minutes including 10 minutes of laser ablation. The evolution of the shear modulus and the temperature is shown in Fig. 3.13. The increase in temperature was successfully measured to 40 ° during the ablation. However, no reliable change in elasticity was observed and too low values of shear modulus (500 Pa) were measured during the experiments.

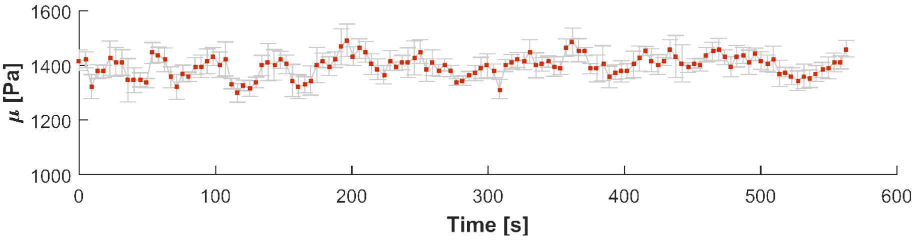

Figure 3.12 – Stability of in vivo measurements with the MRE pulse sequence triggered on the respiration.

However, a mechanical difficulty was encountered during this experiment. A dramatic decrease of the wave amplitude in the region of the fibers was observed (Fig.3.14). During this experiment, fibers were inserted with a small angle of 15° with respect to the needle MRE driver. It is likely that the wave propagation is disturbed by the group of fibers. Numerical simulations tend to corroborate to this assumption. Details of the study are given in Appendix C. In the ex vivo experiment, needles were inserted perpendicular to the needle MRE driver and the wave was correctly propagating in the ablated region. A different orientation of the fibers is expected to solve the problem. Based on this assumption, fibers were perpendicular to the needle MRE driver in Experiment B.

Experiment B: Measurements of elasticity changes

After inserting the needle perpendicularly to the needle MRE driver, the laser ablation was monitored in temperature and elasticity with the same protocol as the one used in Experiment A. With this setup, the wave was propagating in the ablated region, which allowed us to measure elasticity with confidence. Wave images acquired during the ablation are shown in Fig.3.15. The simultaneous evolution of shear modulus and temperature in the lesion are plotted in Fig.3.16. When the laser is turned on, the wavelength continuously increases in the fiber tip zone, corresponding to an increase of the shear modulus in the elastograms. As expected, the target ablation temperature of 60°C is reached after 10 minutes. When the laser is turned off, the temperature decreases while the shear modulus value remains steady in the lesion.

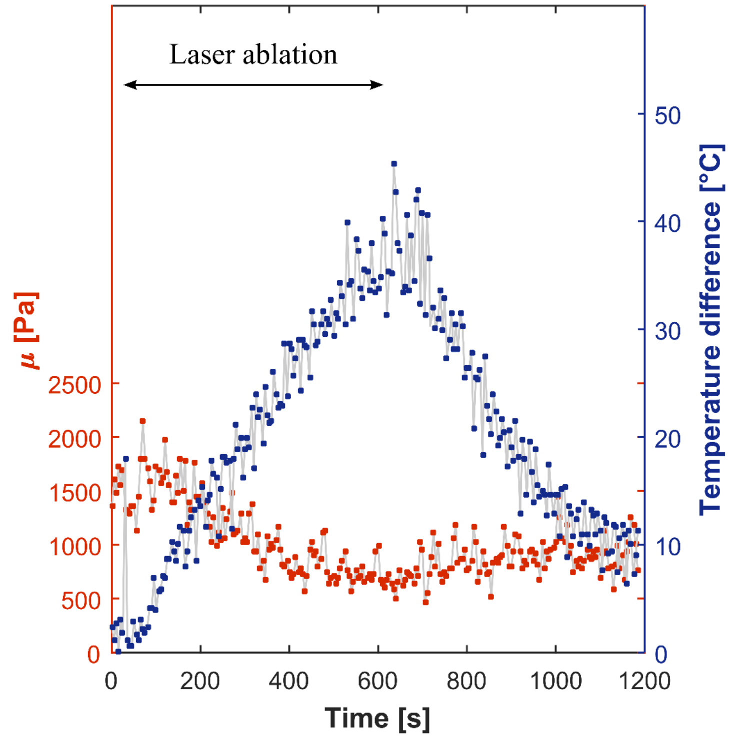

Figure 3.13 – Evolution of the shear modulus(in red)and the temperature (in blue) during a laser ablation in swine liver in vivo (Experiment A).

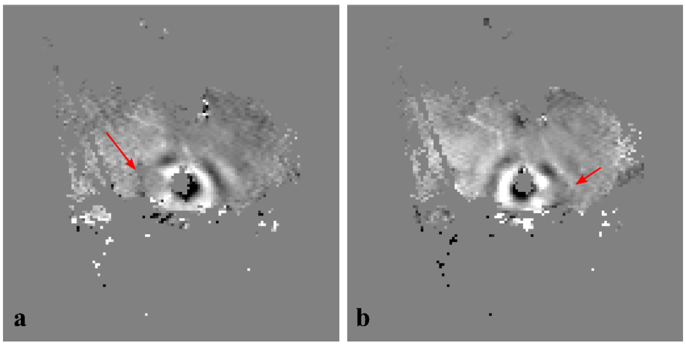

Figure 3.14 – The fibers are parallel and inclined with 15° to the axis of the excitation needle. The slice positions in (a) and (b) are the same. The region of the fiber tips (red arrows) is located on the left (a) and on the right (b) of the needle MRE driver in (b). In both cases, a dramatic decrease of the wave amplitude in the region of the fibers is observed.

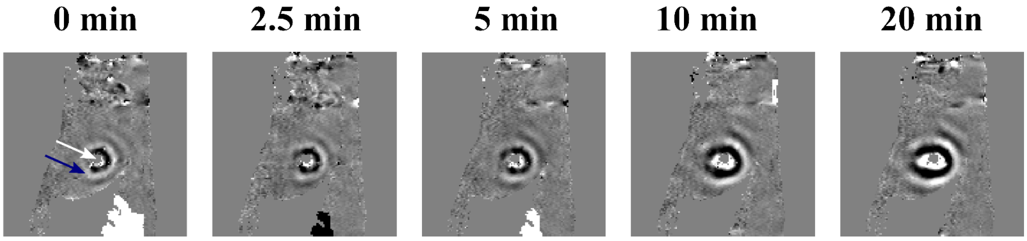

Figure 3.15 – Evolution of the wave pattern during the in vivo laser thermal ablation. The wave propagates circularly around the needle MRE driver (white arrow). The lesion is located below the needle on the left (blue arrow). The wavelength increases gradually in the ablation zone during the first 10 minutes.

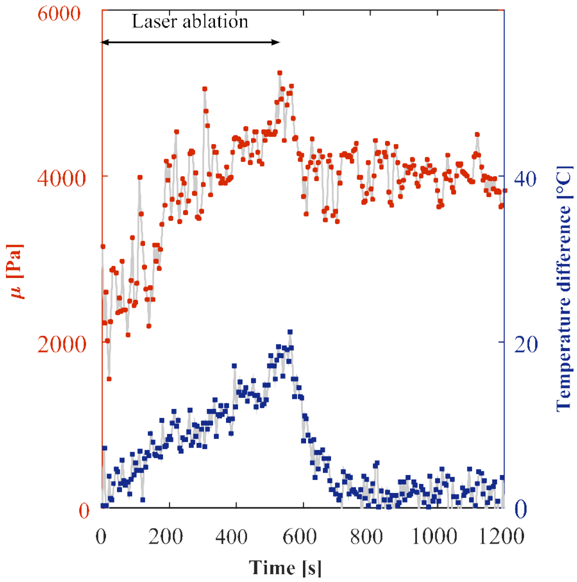

Figure 3.16 – Evolution of the shear modulus(in red)and the temperature (in blue) during a laser ablation in swine liver in vivo (Experiment B).

3.5 Discussion

These experiments were carried out to study the feasibility and the relevance of the proposed interventional MRE protocol. A complete MRE system was designed to fulfill the specific requirements for interventional MRE and was tested in phantoms and in vivo.

The needle MRE driver was inserted by the interventional radiologist as it would be done in a clinical protocol. The advantage of such internal mechanical exciter is the generation of a localized wave source directly in the region of interest. Hence, the problem of wave attenuation through the tissue located between the mechanical driver and the region of interest is circumvented. This implies that deep-lying regions of interest can be investigated, and the use of high frequency excitation becomes possible in spite of higher wave attenuation. Nevertheless, as noticed during the experiments on liver samples, the wave amplitude attenuation remains an issue in viscous tissues. This issue results in limited area around the needle where elastograms can be successfully monitored. The depth of the region of interest is not anymore an issue but the needle MRE driver must be inserted in area close to the investigated region. It is important to note that the excitation frequency can be changed to low values (e.g. 60 Hz) or high values (e.g. 150Hz) depending on the requirements of the application (large coverage or high resolution).

The direction of wave propagation is essentially perpendicular to the needle axis and the displacement is parallel to it, which implies a well-defined cylindrical shear wave pattern. This well-defined shear wave pattern is particularly well-suited to the resolution of the inverse problem. However, the region lying behind the tip of the needle is difficult to investigate because the wave does not propagate correctly further than the needle tip in the needle shaft direction.

Although the two versions of the needle MRE driver have not been tested on the same liver, amplitude wave measurements of the different experiments suggest that the two versions of the needle MRE driver approximately ensure the same motion amplitude. However, the second version of the needle MRE driver is more user-friendly, more adapted to interventional procedures and does not require someone to hold the needle. It is also important to notice the difference in the first wave front amplitude between in vivo liver, ex vivo liver and gelatin. Higher in vivo amplitude may suggest higher adherence between the needle and the tissue in vivo, when compared to ex vivo liver and gelatin phantoms where higher slipping may occur.

Interventional MRE includes a fast and interactive MRE sequence based on a spoiled gradient echo pulse sequence. A major advantage of the proposed MRE sequence is its interactivity, which allows to dynamically change the monitored image plane. This is expected to help to the monitoring of thermal therapy.

It is important to emphasize that the proposed method was developed optimally for the monitoring of elasticity changes in interventional radiology, and not particularly for full 3D quantitative biomechanical characterization. Only one excitation frequency and one slice were therefore used. Moreover, as previously mentioned, the needle MRE driver generates a well-defined shear wave pattern. Additional steps of acquisition and processing aiming at removing the longitudinal component are therefore not expected to improve substantially the result of the inverse problem. Motion is thus encoded in only one direction, parallel to the needle shaft axis.

The sliding window scheme was implemented in order to provide an elastogram with every new phase difference image obtained. Thus, the elastogram update rate is as high as the one obtained with the one-phase-offset acquisition protocol but with the benefit of the temporal Fourier transform. Nevertheless, each elastogram is not a totally independent measurement since each wave image is used for three consecutive elastograms. A smoothing effect might therefore be noticed but the accuracy of the measurements is not affected in a different manner as it would be with a classical MRE reconstruction scheme.

In conventional MRE, at least 4 phase-offsets are used to reconstruct the elastogram. As opposed to diagnostic MRE, interventional MRE requires a short acquisition time: acquisition speed of all images necessary for one elastogram must be high enough compared to typical elasticity rate of change. A tradeoff was proposed here to improve acquisition times while preserving the quality of elastograms. Only 3 phase-offsets were acquired.

The developed MRE system has allowed to demonstrate the feasibility of detecting changes in elasticity in real-time, both in phantom experiments and ex-vivo experiments. The combination of thermometry and elastography is expected to help the monitoring of thermal ablation as shown during the ex vivo experiment. Based on encouraging results, the protocol was refined to meet the requirements of in vivo experiments. Preliminary experiments have shown the feasibility of continuously computing elastograms during a long period thanks to the respiratory triggering.

The stability of the protocol was assessed by Experiment A, a standard deviation inferior to 5% was observed over 127 elastograms, which validates the respiratory-triggered interventional MRE sequence. However, a limitation must be noticed: the total acquisition time of 6 images required to reconstruct one elastogram is increased by a factor of about 2. Indeed, the interval between two phase difference image is equal to one respiratory cycle (5 seconds in the experiments). The elasticity rate of change is poorly known but it could be of the same order of magnitude in some cases.

Limitations of the current interventional MRE method are raised by the last in vivo experiments. First of all, it must be noticed that the temperature evolution curve is noisier in these last experiments. The respiratory triggering may be the cause of this supplementary noise. Although the acquisition window is adjusted in order to reduce physiological motion during this period and each pair of images are acquired at the same time of the cycle, some phase images are probably shifted of one pixel and affect the temperature measurements. The interview motion between phase images might affect the phase addition required to remove the phase due to the motion. If pixels are shifted from one image to the second one, the temperature measurement is inaccurate. Minimizing the acquisition window by reducing the acquisition matrix might solve this issue.

The difficulties encountered during the monitoring of the laser ablation deserve to be detailed in order to improve the system. First, the needle MRE driver is placed on the skin and the needle is inserted. Then, needles used to guide the laser fibers are inserted in the region of interest. A home-made guiding tool is used in the Experiment A to make this task easier. The needle tips must be in a small region of approximately 1 cm of diameter. It is very difficult to evaluate precisely the position of the needle tips because of the needle artifacts. The MRE acquisition slice is placed so that the slice is perpendicular to the needle MRE driver and includes the expected ablated region. The next step consists in inserting the fibers in the needles and then pulling out the needles. It is very challenging to keep the fibers immobile during this step. Given that fibers are almost invisible in MRI, the fiber positions can not be checked after removing the needles. The current MRE pulse sequence enables the acquisition of only one slice. If the position of fibers has changed, the planned slice will not include the ablated region and the monitoring will be useless. Refinements of the sequence will be necessary to enable the acquisition of several slices.

A mechanical difficulty was also encountered. During the Experiment A, a dramatic decrease of the wave amplitude in the region of the fibers was observed. Experiments A and B have shown that the orientation of the laser fibers has an impact of the results, which is a limitation of this system. However, when the fibers are perpendicular to the needle MRE driver, the wave propagation in the lesion is ensured.

Shear modulus estimates of Experiment A are probably not reliable due to aforementioned artifacts in shear wave propagation. However, it is impossible to evaluate the accuracy of the results because the ground truth is not known. Besides, the current MRE protocol does not offer the possibility of returning a confidence map. This map would evaluate the reliability of the results returned by the LFE algorithm. Ideally, this map would be computed from phase images by evaluating the wave amplitude of the propagating wave in every pixel. Under an adequately chosen threshold, the result would be considered as unreliable. Further investigations are needed to implement it. This tool should be implemented in the next version of the interventional MRE system.

Regarding the results of the in vivo monitoring of Experiment B, consistent increase in elasticity of 2000 kPa was observed during the ablation and this value stabilizes when the laser is turned off. For the first time, in vivo thermal ablation was monitored by simultaneous MR elastography and MR thermometry with a refresh rate of one elastogram with every breathing cycle, i.e. every 5 seconds. This experiment highlights the complementarity of simultaneous temperature and elasticity monitoring during the thermal ablation and demonstrates the feasibility and the relevance of interventional MRE for the monitoring of percutaneous thermal ablations.

Chapter 4

An alternative to conventional MRE data processing based on raw data

> " *L'esprit qui invente est toujours mécontent de ses progrès, parce qu'il voit au-delà.* "
>
> Jean Le Rond d'Alembert

Contents

Previous chapters were dedicated to the description and the evaluation of an all-in-one interventional MRE system for the real-time monitoring of percutaneous procedures. In this chapter, we propose an innovative method for MRE data processing. The method called "raw MRE method" is intended to circumvent several challenging steps of the MRE data processing. Specifically, while conventional MRE relies on phase images to estimate elasticity, the proposed raw MRE method allows to estimate the elasticity map, and eventually a wave pattern image, without reconstructing any phase image. This is expected to accelerate the protocol and decrease the sources of variability in results. A variation of the "raw MRE method" is also proposed for the specific case of real-time monitoring of thermal ablations.

4.1 Introduction

Computing an elasticity map from MRI data is a long and complex process. A substantial number of steps is involved in MRE data processing. Moreover, different algorithms may exist for a single step, which may cause variability in the results reported by different groups. After the acquisition of raw data in the k-space, phase images are first reconstructed and preprocessed to enhance the wave image. Let us remind the steps of wave enhancement already detailed in Section 2.3.1. First, phase images are reconstructed within the range $[-\pi, \pi]$. This limited interval may result in phase wrapping, i.e. steep variations in the resulting phase image, which may cause errors during the inverse problem solving. A phase unwrapping algorithm is therefore needed to recover the true phase. Then, harmonic analysis is performed on the resulting phase image series to select only the displacement component at the temporal frequency of interest. Finally, the inverse problem solver is applied on the resulting image to compute an elasticity map. The objective of this chapter is to present a new approach for MRE data processing aiming at reducing the source of variability and errors by removing some complex and long steps. The "raw MRE method" relies on processing directly raw MRE data without any reconstruction of phase images. The underlying theory behind the raw MRE method is developed in the next section and two distinct applications are detailed thereafter.

4.2 Theoretical background

The approach that we propose here consists in directly processing the raw data without reconstructing phase images. Removing the phase image reconstruction allows to avoid the delicate step of phase unwrapping. Finally, instead of filtering in the frequency domain of the phase image after spatial Fourier transform, the new method consists in applying the filters directly in the k-space of the acquired complex signal. A schematized comparison of the conventional process and the proposed process is given in Fig.4.1. This chapter introduces the theoretical background of the proposed method, which is tested both on

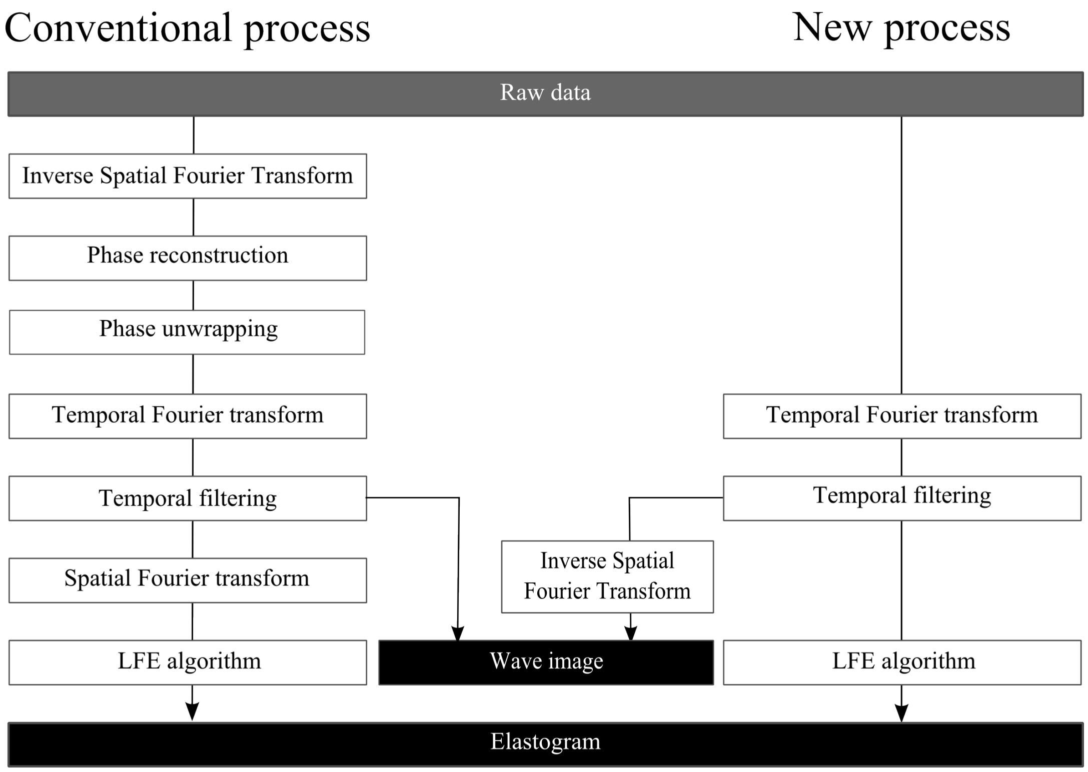

Figure 4.1 – Description of the conventional method (with or without phase unwrapping) and the new proposed method.

phantoms and in vivo. Results are compared with those obtained using a conventional MRE framework.

4.2.1 Conventional MRE

As detailed in previous sections, MRE relies on the encoding of tissue motion in the phase Φ of the complex MRI signal. Let us consider a harmonic oscillation of one isochromat with maximum amplitude u_0 at a given temporal frequency f_e, where $\vec{u}$ is the position vector:

$$\vec{u}(t) = \vec{u_m} + \vec{u_0} \sin\left(2\pi f_e t \quad \vec{k}.\vec{u} + \alpha\right) \tag{4.1}$$

where k is the wave number, u_m is the mean position and α is the initial phase offset. A number N_p of periods of a sinusoidal motion sensitizing gradient G with maximum amplitude G_0 is implemented in the MR-pulse sequence and its polarity is switched with respect to the mechanical excitation frequency f_e.

$$G(t) = \begin{cases} G_0 \sin(2\pi f_e t) & t \in [0, \frac{N_p}{f_e}] \\ 0 & otherwise \end{cases} \tag{4.2}$$

It has been shown that the observed MRI phase shift Φ_s acquired with a gradient echo sequence including the described MEG is proportional to the scalar product of the position vector and the gradient vector.

$$\Phi_s = \frac{\gamma N_p(\vec{G_0}.\vec{u_0})}{2f_e}\cos(\vec{k}.\vec{u} - \alpha) \tag{4.3}$$

A similar equation can be written when the MEG frequency f_g and the mechanical excitation frequency f_e are not equal (fractional encoding [Rump et al., 2007]):

$$\Phi_s = \frac{\gamma f_g(\vec{G_0}.\vec{u_0})}{\pi(f_g^2 - f_e^2)}\sin(\frac{\pi f_e}{f_g})\cos(\frac{\pi f_e}{f_g} - \vec{k}.\vec{u} + \alpha) \tag{4.4}$$

More generally, the observed MRE phase shift can simply be written as:

$$\Phi_s = C_1\cos(-\vec{k}.\vec{u} + C_2) \tag{4.5}$$

The same expression can be obtained for spin echo sequences with different expressions for C_1 and C_2. MRE relies on estimating the wave number k from the phase of the acquired MRI signal. The conventional protocol involves the reconstruction of the phase image within the range [-π,π], the use of a phase unwrapping algorithm, the harmonic analysis on a set of images with different initial phase offsets α and finally the application of image processing filters in the spatial frequency domain of the phase image. The objective of this study is to propose a new approach that circumvents several of the aforementioned steps. By directly processing the raw data, we propose here to derive the elasticity value without prior reconstruction of any phase image.

4.2.2 MRE using raw data

The proposed theoretical framework will be developed in 1-D for clarity. It can be easily extended to 2D images. The raw MRI signal S acquired in the k-space can be defined with respect to the transverse magnetization I as :

$$S(\nu_x) = \sum_{x=0}^{N_x-1} I(x)e^{-j2\pi\frac{\nu_x x}{N_x}} \tag{4.6}$$

where x is the arbitrary discrete spatial dimension considered in the example, N_x is the total number of points, ν_x is the discrete spatial frequency and I is the transverse magnetization $I(x) = M(x)e^{j\Phi(x)}$, M being its magnitude and Φ being its phase. In the specific case of MRE, Φ is given by:

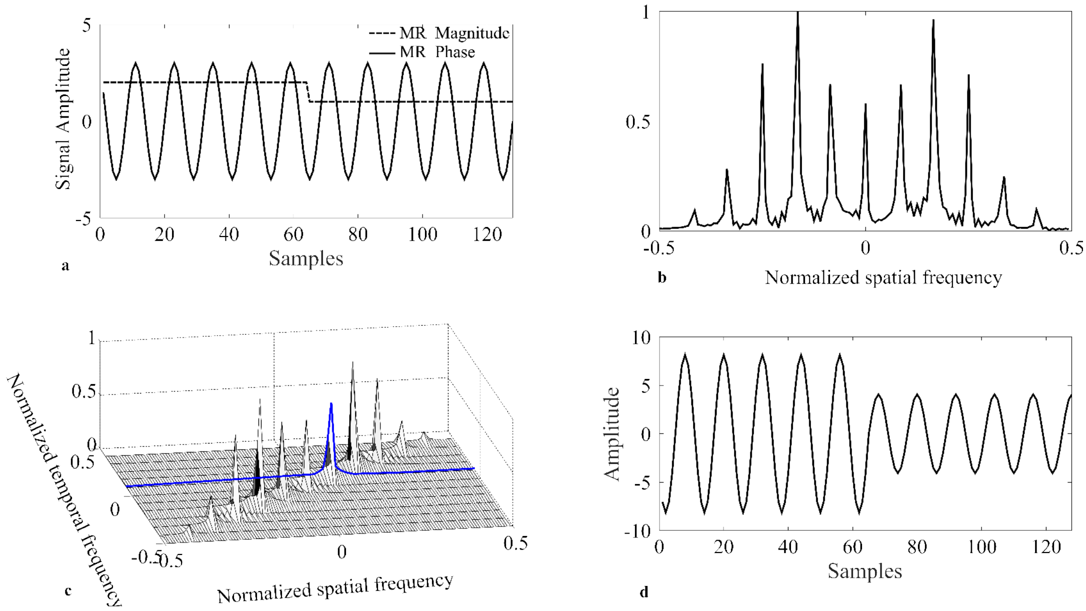

Figure 4.2 – a) Simulated 1D MR signal with heterogeneous magnitude and sinusoidal phase b) Simulated raw data of the simulated 1D MR signal c) Plot of the temporal Fourier transform of a simulated data set with 12 varying delays between excitation and MEG. Selection of the component of interest of the spatial frequency in blue and d) Plot of the wave signal obtained with the proposed method. All ordinates are in arbitrary units.

$$\Phi(x) = \Phi_0(x) + \Phi_s(x) \tag{4.7}$$

where Φ_0 is the background phase, i.e. the constant phase obtained without motion encoding, and Φ_s is the phase shift related to the encoded displacement as described in Eq.(4.3). The k-space acquired in MRE experiments can therefore be written as follows:

$$S(\nu_x) = \sum_{x=0}^{N_x \;\; 1} M(x) e^{j\Phi_0(x)+jC_1(x)\cos(\;\;\frac{k_x x}{N_x}+C_2)} e^{\;\;j2\pi\frac{\nu_x x}{N_x}} \tag{4.8}$$

where $\frac{k_x}{N_x}$ corresponds to the normalized discrete wave number. Eq.(4.8) includes an exponential of a cosine function that can be rewritten using the Jacobi-Anger expansion [Colton and Kress, 1998]:

$$S(\nu_x) = \sum_{x=0}^{N_x \;\; 1} M(x) e^{j\Phi_0(x)} e^{\;\;j2\pi\frac{\nu_x x}{N_x}} \sum_{n=\;\;\infty}^{\infty} j^n J_n(C_1(x)) e^{\;\;\frac{n k_x x}{N_x}+nC_2} \tag{4.9}$$

where J_n is the nth Bessel function. This equation highlights the presence of an infinite number of harmonics of the spatial frequency of interest in the k-space due to the presence

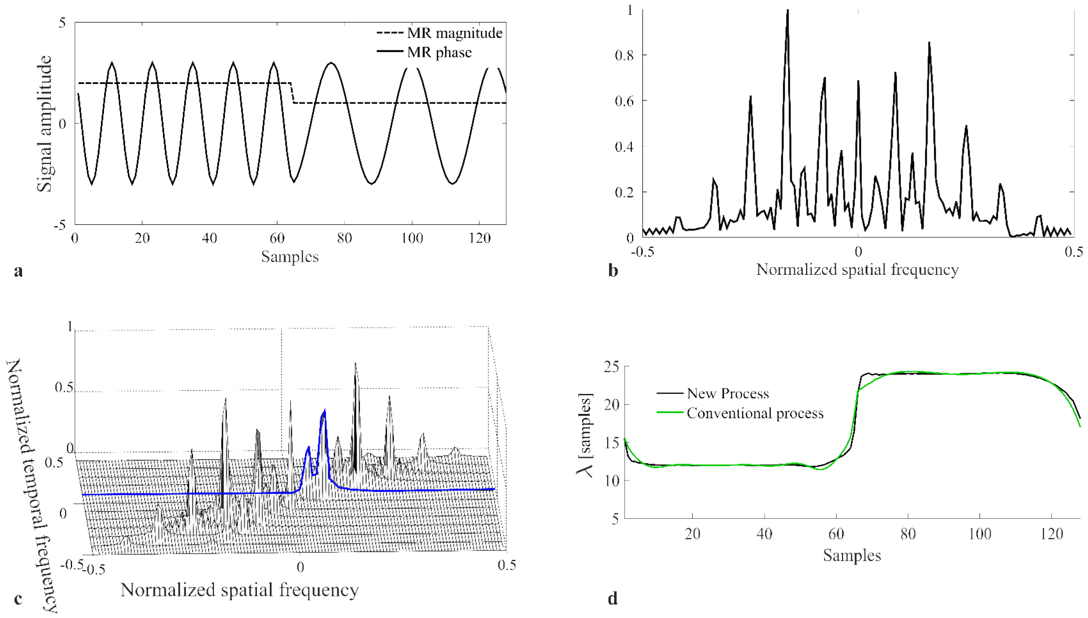

Figure 4.3 – a) Simulated 1D MR signal with heterogeneous magnitude and a signal composed of two frequencies. b) Simulated raw data of the simulated 1D MR signal c) Plot of the temporal Fourier transform of a simulated data set with 12 varying delays between excitation and MEG. Selection of the component of interest of the spatial frequency in blue and d) Local frequencies returned by the LFE-algorithm performed on the filtered k-space (black) compared to the conventional result obtained with the same filters (green)applied to phase signal.

of a cosine pattern in the phase signal. A similar phenomenon has already been described in a previously published work [Riek et al., 1993] in the framework of motion compensation in MRI.

In order to illustrate this phenomenon, a simulated 1D MRE signal is represented in Fig.4.2a, Fig.4.2b showing the simulated spectrum of the resulting MRE 1D-signal. In this figure and the following, only the modulus of complex signals are represented in the frequency domain. The spectrum is not composed of only one component but of an infinite number of harmonics as predicted by the previous Eq.(4.9). The objective of this work is to avoid the reconstruction of the phase image and directly process raw data. A solution is needed to remove all harmonics and select only the component of interest. Although this could be performed by using a simple low pass filter (as suggested by Fig.4.2b), such a solution would not be applicable in real tissue, because of its intrinsic heterogeneity that results in the presence of several spatial frequencies of interest (Fig.4.3b). Distinguishing the component of interest of one frequency from the harmonic of another one is impossible.

The proposed solution is inspired from the harmonic analysis used in conventional MRE. As previously mentioned, several images are acquired with varying phase shifts between mechanical excitation and motion encoding gradients. A temporal Fourier transform is subsequently performed on phase images in order to select only the displacement induced by the generated mechanical wave at a specific excitation frequency. The following paragraph aims at demonstrating that a similar analysis directly performed on the k-space data allows identifying and extracting the components of interest. Let us consider N_t acquisitions with varying phase offsets evenly spaced around the mechanical excitation cycle (i.e; sampling frequency f_s equal to $N_t f_e$). The temporal discrete Fourier transform of the series yields:

$$S(\nu_x,\nu_t)=\sum_{t=0}^{N_t-1} e^{-j2\pi\frac{\nu_t t}{N_t}}\sum_{x=0}^{N_x-1} M(x)e^{j\Phi_0(x)+jC_1(x)\cos\left(-\frac{k_x x}{N_x}+C_2+\frac{2\pi t}{N_t}\right)}e^{-j2\pi\left(\frac{\nu_x x}{N_x}\right)} \tag{4.10}$$

The Jacobi-Anger expansion is applied in the same way:

$$S(\nu_x,\nu_t)=\sum_{t=0}^{N_t-1} e^{-j2\pi\frac{\nu_t t}{N_t}}\sum_{x=0}^{N_x-1} M(x)e^{j\Phi_0(x)}e^{-j2\pi\frac{\nu_x x}{N_x}}\sum_{n=-\infty}^{\infty} j^n J_n(C_1(x))e^{j\left(-n\frac{k_x x}{N_x}+nC_2+n\frac{2\pi t}{N_t}\right)} \tag{4.11}$$

$$=\sum_{x=0}^{N_x-1} M(x)e^{j\Phi_0(x)}e^{-j2\pi\frac{\nu_x x}{N_x}}\sum_{n=-\infty}^{\infty} j^n J_n(C_1(x))e^{j\left(-n\frac{k_x x}{N_x}+nC_2\right)}\sum_{t=0}^{N_t-1} e^{-j2\pi\frac{\nu_t t}{N_t}}e^{jn\frac{2\pi t}{N_t}} \tag{4.12}$$

Fig.4.2c illustrates the effects of the temporal Fourier transform on the previously simulated signal with 12 varying phase-offsets evenly spaced around the mechanical excitation. Spatial harmonics are thus separated over the temporal frequency range. The spatial component of interest is now distinguishable since this component is now associated to the temporal frequency of interest.

Let us consider the previous expression Eq.(4.12) at the temporal excitation frequency f_e (with $f_e=\frac{f_s}{N_t}$ which corresponds to $\nu_t=1$):

$$S(\nu_x,1)=\sum_{x=0}^{N_x-1} M(x)e^{j\Phi_0(x)}e^{-j2\pi\frac{\nu_x x}{N_x}}\sum_{n=-\infty}^{\infty} j^n J_n(C_1(x))e^{-jn\frac{k_x x}{N_x}+jnC_2}\sum_{t=0}^{N_t-1} e^{-j2\pi\frac{t}{N_t}}e^{jn2\pi\frac{t}{N_t}} \tag{4.13}$$

The sum over N_t is non null and equal to N_t only if $n=1mod(N_t)$, therefore the Eq.(4.13) reduces to:

$$S(\nu_x,1)=\sum_{n\in U}\sum_{x=0}^{N_x-1} M(x)e^{j\phi_0(x)}e^{-j2\pi\frac{\nu_x x}{N_x}}j^n N_t J_n(C_1(x))e^{jn\left(-\frac{k_x x}{N_x}+C_2\right)} \tag{4.14}$$

$$U=n|n=kN_t+1,k\in\mathbb{Z}^*$$

Let us assume that the number of phase-offsets is sufficient to satisfy the following condition.

$$\log \frac{|J_1(C_1(x)|)}{|J_{kN+1}(C_1(x))|} > 1, k \in \mathbb{Z}^* \tag{4.15}$$

Details of this condition will be provided later in this chapter (Section 4.2.3). Eq.(4.13) then simplifies to:

$$S(\nu_x, 1) = \sum_{x=0}^{N_x \ \ 1} M(x) e^{j\phi_0(x)} e^{\ \ j2\pi\left(\frac{\nu_x x}{N_x}\right)} j N_t J_1(C_1(x)) e^{j\left(\ \ \frac{k_x x}{N_x} + C_2\right)} \tag{4.16}$$

The component of interest is separated from the harmonics and selected (blue line in Fig.4.2c). At this stage, there are three possibilities quickly introduced here and detailed further in this chapter:

1. It is possible to directly obtain the spatial distribution of the wavelength, and hence to reconstruct elastograms without prior phase image reconstruction. For that purpose, classic image filters of the LFE algorithm, conventionally used in the frequency domain of the phase signal, are applied to the k-space raw data. Indeed, image processing filters can be directly applied in the k-space obtained after temporal Fourier transform (Eq.(4.16)) without reconstructing any phase image.
   The LFE-algorithm aims at estimating the local wavelength in every pixel. As explained in Section 2.3.1, the local frequency of a real signal is defined as the derivative of the phase of its analytic signal. A pair of two lognormal quadrature filters R_1 and R_2 are classically applied on the frequency domain of the enhanced wave image and the local frequency f_l is given by:

   $$f_l = \sqrt{f_1 f_2} Re \left(\frac{\mathcal{F}^{\ \ 1}(R_2 S)}{\mathcal{F}^{\ \ 1}(R_1 S)} \right) \tag{4.17}$$

   where f_1 and f_2 are the central frequencies of R_1 and R_2, respectively. $\mathcal{F}^{\ \ 1}$ is the inverse Fourier transform. Usually, S is the signal in the spatial frequency domain of the enhanced wave image resulting from phase reconstruction, phase unwrapping, temporal frequency filtering and finally spatial Fourier transform. In this work, it is proposed to apply the same algorithm on k-space data obtained after temporal frequency filtering. In this case, S is described by Eq.(4.16). This complete process is illustrated in Fig.4.3 on a 1D simulated MRI signal (Fig.4.3a), yielding the local frequency for each sample (Fig.4.3d).

2. Other inverse problem solvers that work in the spatial domain, such as direct inversion of Helmholtz equation, may be preferred. In this case, a wave pattern image may be recovered by applying the inverse spatial Fourier transform yielding a complex signal:

$$s(x) = \frac{N_t}{N_x} M(x) e^{j\Phi_0(x)} j J_1(C_1(x)) e^{j\left(\frac{k_x x}{N_x} + C_2\right)} \tag{4.18}$$

The imaginary part of Eq.(4.18) simplifies to:

$$Im(s(x)) = \frac{N_t}{N_x} M(x) J_1(C_1(x)) \cos\left(\frac{k_x x}{N_x} + C_2 + \phi_0(x)\right) \tag{4.19}$$

The obtained wave is weighted by the magnitude and Bessel coefficients that depend on the wave amplitude (Fig.4.2d). Besides, a phase shift related to the background phase is introduced. Nevertheless, it must be emphasized that the information of interest in MRE, i.e. the spatial frequency, is preserved. Besides, we will show later in this chapter that this wave pattern image is not corrupted by phase wrapping. The wave pattern image is reconstructed without reconstructing any phase image nor applying phase unwrapping algorithms.

3. In the framework of the monitoring of thermal ablations by MRE, it is proposed here to directly evaluate elasticity changes in the k-space raw data. Based on the fact that elasticity is directly related to the spatial frequency, this component is directly tracked in the k-space raw data. This would not be possible without the proposed temporal Fourier transform because too many components are present. Thanks to the temporal filtering, only the component of interest is highlighted which makes possible its tracking. This option will be the scope of the Section 4.4.

The following sections focus on the first two possible outputs of the method: wave pattern and elastogram.

4.2.3 Relationship between C_1 and N_t

The previously developed theory and 1D examples suggest that this method could provide wave pattern and elasticity estimation without reconstructing any phase image. Nevertheless, a condition relying on the relationship between N_t and C_1 must be fulfilled to obtain the expected result.

A temporal Fourier transform is applied on a set of N_t k-space raw data acquired with varying delays between mechanical excitation and motion encoding gradients. By selecting only the temporal frequency of interest, most of the harmonics of the spatial frequency are

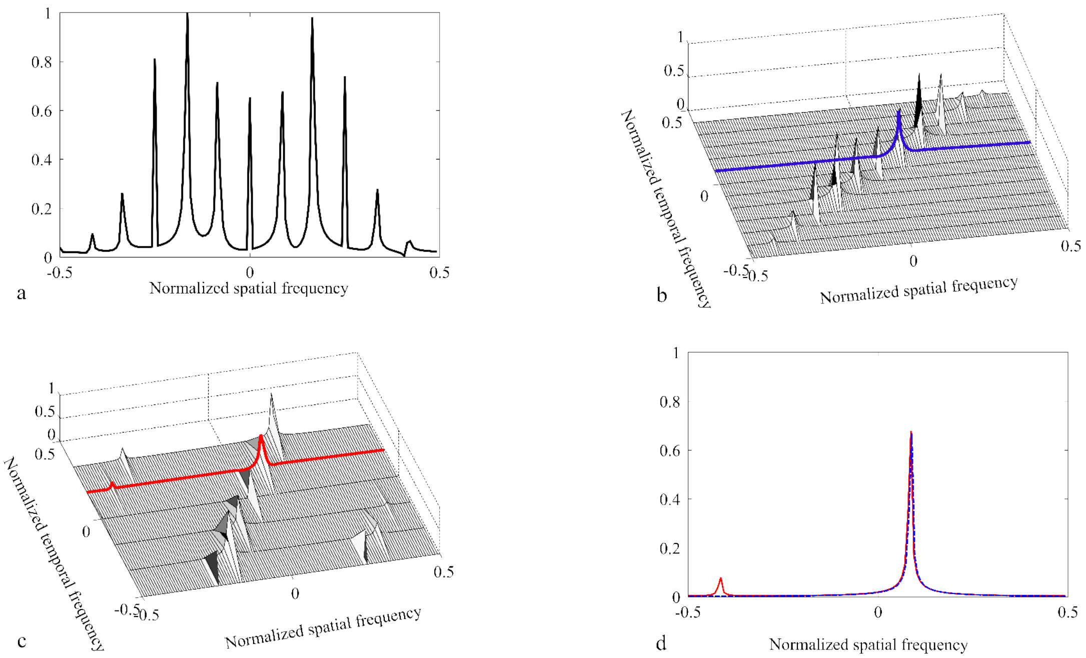

Figure 4.4 – a) Plot of the k-space for a 1D signal with a homogeneous magnitude and a sinusoidal phase. b) Plot of the temporal Fourier transform of the previous k-space performed from the data set simulating 12 varying delays between motion encoding gradients and mechanical excitation. c) Plot of the temporal Fourier transform performed from the data set simulating 6 varying delays between motion encoding gradients and mechanical excitation and d) Plot of the filtering at the temporal frequency of interest in blue for the case with 12 phase-offsets and in red for the case with 6 phase-offsets.

removed. The result is described by the following equation:

$$S(\nu_x, 1) = \sum_{n \in U} \sum_{x=0}^{N_x - 1} M(x) e^{j\phi_0(x)} e^{-j2\pi\left(\frac{\nu_x x}{N_x}\right)} j^n N_t J_n(C_1(x)) e^{jn\left(-\frac{k_x x}{N_x} + C_2\right)} \tag{4.20}$$

$$U = n | n = kN_t + 1, k \in \mathbb{Z}^* \tag{4.21}$$

As described by the set U, the component $(n = 1)$ is not the only one component selected by this filtering because of aliasing. In most cases, the other components are negligible compared to the first one (blue signal in Fig.4.4.b), nevertheless the selection of non negligible components remains possible when the number N_t of phase-offsets is poorly chosen as illustrated in Fig.4.4c-d (red signal). It is therefore relevant to assess conditions that favor an optimal ratio between the amplitude of the 1^{st} and the $(kN + 1)^{th}, k \in \mathbb{Z}^*$ components of the spectrum that are susceptible to being associated to the same temporal frequency. The ratio R is deduced from Eq.(4.20):

$$R = \log \left| \frac{J_1(C_1)}{J_{kN+1}(C_1)} \right| \forall k \in \mathbb{Z}^* \tag{4.22}$$

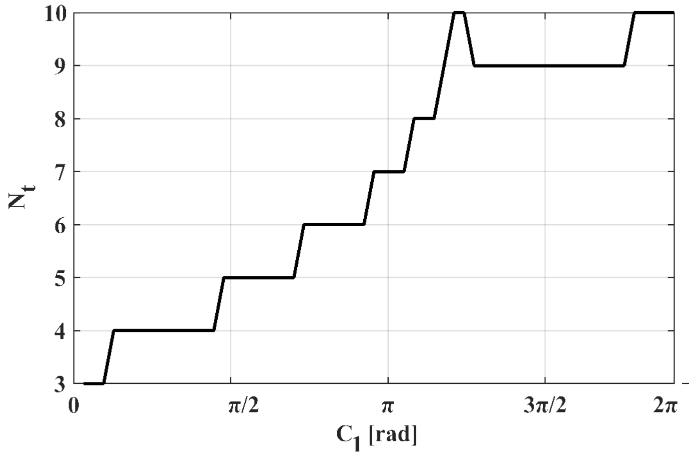

Figure 4.5 – Assessment of the minimal number of phase-offsets N_t required to satisfy the condition $R > 1$ with respect to the amplitude of the encoded wave C_1.

Let us consider that a component is negligible compared to another one when its amplitude is at least 10 times inferior to another one, i.e. when $R > 1$. The number of phase-offsets N_t required to satisfy this condition is plotted in Fig.4.5 with respect to the C_1 parameter. Under the assumption that $R > 1$, Eq.(4.20) simplifies to:

$$S(\nu_x, 1) = \sum_{x=0}^{N_x \quad 1} M(x) e^{j\phi_0(x)} e^{\quad j2\pi\left(\frac{\nu_x x}{N_x}\right)} j N_t J_1(C_1(x)) e^{j\left(\quad \frac{k_x x}{N_x} + C_2\right)} \tag{4.23}$$

The number of phase-offsets N_t is a critical point of this method. A minimal number is required to select only the component of interest. Nevertheless, when the peak amplitude C_1 of the phase variation is inferior to $\pi/4$ rad, only 3 or 4 phase-offsets enable the selection of the component of interest. More phase-offsets are required for a higher C_1.

Under the assumption of a spatially uniform motion amplitude, the parameter C_1 can be considered as spatially uniform. In this case, the amplitude of the wave returned by the proposed method is multiplied by a Bessel coefficient $J_1(C_1)$ and the amplitude of spatial frequency components of interest are weighted by the same factor. Nevertheless, the amplitude of the wave may vary with respect to tissue interfaces. Motion amplitude also decreases with respect to distance from the excitation source. In this more general case, the resulting wave is weighted by Bessel coefficients that are spatially dependent. Fig.4.6 shows an example of a signal with a non-uniform motion amplitude and its corresponding wave pattern image obtained with the proposed method. It it important to notice that the spatial frequency is preserved. As a result, only the amplitude of the wave is changed in the wave pattern image and the shear modulus calculated from the wave pattern image or directly from the processed raw data will not be affected.

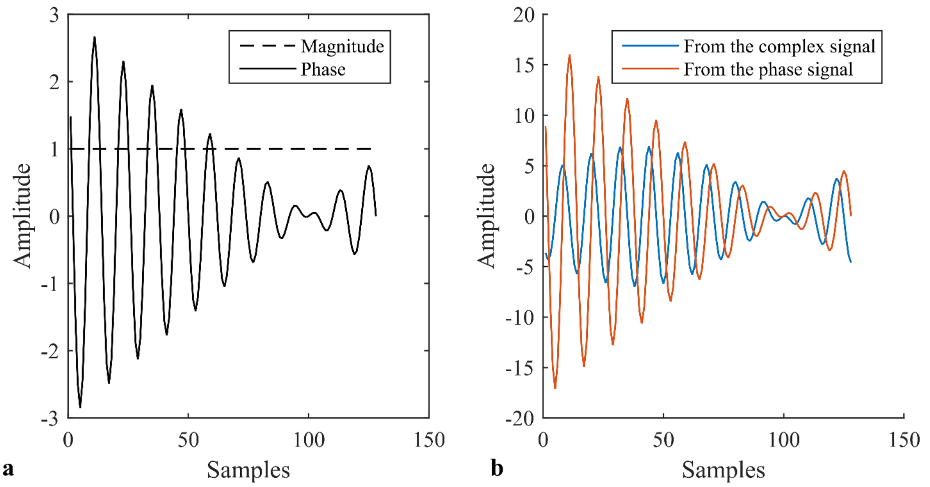

Figure 4.6 – Impact of a non-uniform motion amplitude. a)Input signal b) Signal returned by the conventional method (in red) and the proposed method (in blue).

In conventional MRE, a high amplitude of the wave can be an issue when it results in phase wrapping. Most of the time, conventional MRE processing methods require phase unwrapping algorithm to unwrap the signal computed in the range $[-\pi, \pi]$. Without unwrapping, wave propagation is not continuous, making the inverse problem very difficult to solve. The raw MRE method allows us to circumvent this issue. First, it must be emphasized that the Fourier transform of a complex signal with a phase signal out of the range $[-\pi, \pi]$ and the same signal with a phase wrapped in the range $[-\pi, \pi]$ are exactly the same. As a consequence, the developed theory is independent to the potential presence of phase wrapping. As long as the aforementioned condition is met ($R > 1$), the reconstructed wave pattern image is unwrapped and the spatial frequency components of interest are preserved. Let us take the example of a signal with a zero-mean phase and a peak-to-peak amplitude of 2 rad (Fig.4.7a-b) and the same signal with a phase that oscillates around 0 rad with a peak-to-peak amplitude of 8 rad (Fig.4.7c-d). It is important to notice that the frequency spectrum of phase signal without (Fig.4.7b) or with (Fig.4.7.d) wrapping is totally different. Obviously, the presence of phase wrapping in the phase signal adds some frequency components to the phase signal. On the contrary, only the amplitude of the frequency components of the complex signal are modified because C_1 changed. There are no additional frequency components, but the required minimal number of phase-offsets N_t is different because amplitudes of the harmonics changed. Indeed, the condition is more difficult to satisfy because the amplitude of the harmonics out of interest are higher than in the previous case and the frequency component of interest is lower (Fig.4.7d). In this example (Fig.4.8), 10 phase-offsets are used ($C_1 = 4$). Let us highlight that $N_t = 10$ is sufficient to reconstruct an unwrapped signal with the raw MRE method. On the contrary, the wave reconstructed by the conventional MRE without unwrapping algorithm is not the

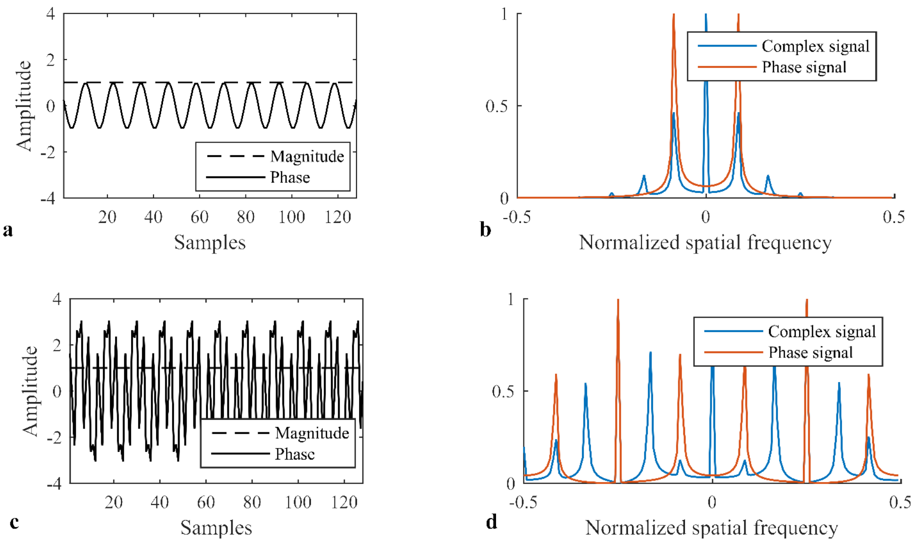

Figure 4.7 – Comparison of signals in the spatial and frequency domains (left and right columns respectively). a.b) Reference signal without phase wrapping, c.d) Signal with phase wrapping due to a high MRE wave amplitude C_1. Additional frequency components are present in the phase ignal (in red), the amplitude of the frequency components of the complex signal are modified (in blue).

one expected.

4.2.4 Impact of the background phase ϕ_0

Although the signal obtained with the raw MRE method preserves the spatial frequency of interest, the resulting signal is not exactly the same as the phase input signal (Eq.(4.19)). As previously demonstrated, the output wave pattern is weighted by the magnitude signal (Fig.4.2d) and the Bessel coefficients related to C_1 (Fig.4.6). This section is intended to evaluate the impact of the background phase Φ_0.

Theoretically, the background phase is null. Obviously, in practice this is not the case due to magnetic field variations. As demonstrated in the developed theory, the presence of a background phase has a minimal impact: it results in the introduction of a phase shift in the reconstructed wave pattern image. Two types of background phase are investigated: locally homogeneous background phase and continuous varying background phase. Fig.4.9a-b is an illustration of a signal with a locally homogeneous background phase and its corresponding image after application of the conventional and the proposed method. The spatial frequency is preserved.

However, a continuous variation of the background phase can also be present. In this case, the background phase is an issue because the phase shift will occur in every pixel and will introduce an error in the wavelength. Fig.4.9c-d illustrates this issue. The signal returned

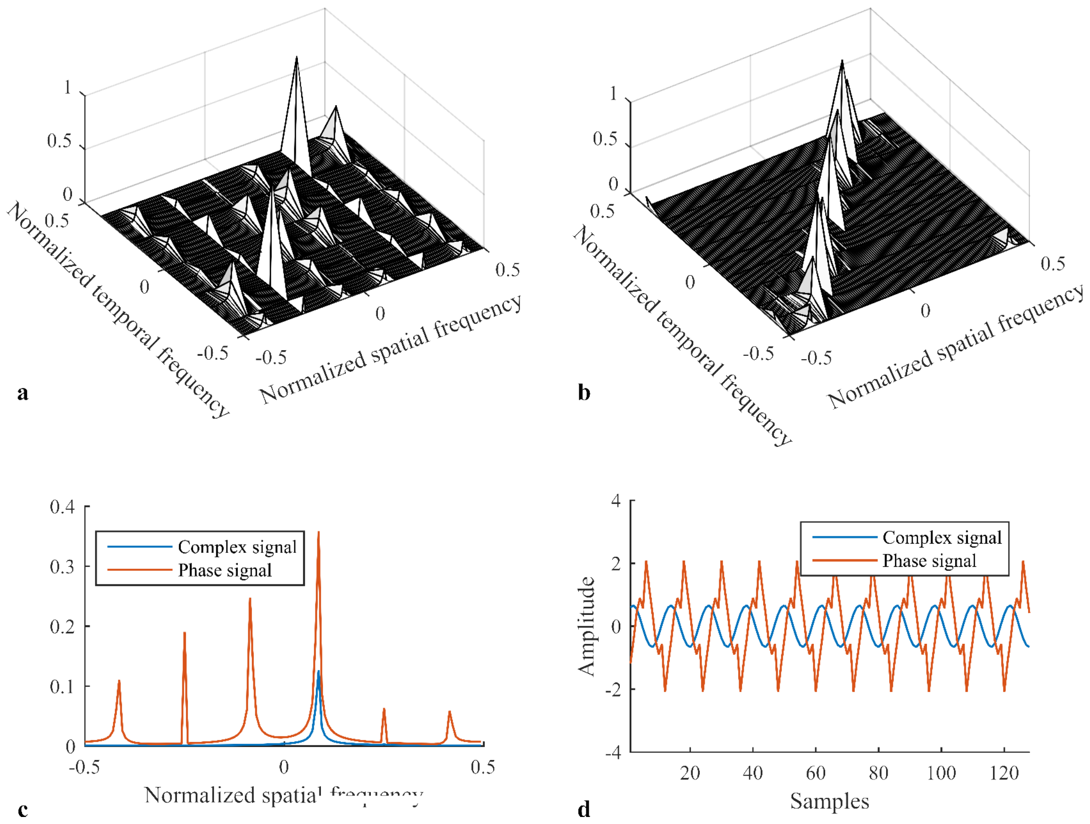

Figure 4.8 – Comparison of the efficiency of the conventional and the proposed methods applied to signals with phase wrapping due to a high motion amplitude. In this example, the number of phase-offsets N_t is equal to 10. a) Phase signal in the spatio-temporal frequency domain. The selected frequency component is shown in red. b) Complex signal in the spatio-temporal frequency domain. The selected frequency component is shown in blue. c) Phase signal (in red) and complex signal (in blue) in the spatial frequency domain after temporal filtering. d) Signal returned by the conventional method (in red) and the proposed method (in blue).

by the proposed method accumulates phase shifts, which results in incorrect wavelength estimation.

In this particular case, it is required to perform the difference of two images ($I_1 = M_1 e^{i\phi_1}$ and $I_2 = M_2 e^{i\phi_2}$) acquired with opposite polarity of motion encoding gradients as it would be done in conventional MRE. However, no phase image is reconstructed, the phase difference must therefore be performed on the raw data. Note that the theoretical background has been developed in the k-space raw data. However, if we are focus on the wave pattern image, it is equivalent to apply the temporal Fourier transform on the complex data after inverse spatial Fourier transform, or vice versa. In this case, the difference can then be performed in the complex domain: $I_1 I_2^* = M_1 M_2 e^{i(\phi_1 \quad \phi_2)}$. In the case of direct reconstruction from k-space raw data, the expression $\mathcal{F}(I_1 I_2^*) = \mathcal{F}(I_1) * \mathcal{F}(I_2)^*(\quad k)$ can be used to perform the difference in the frequency domain. Similarly to conventional MRE methods, this difference removes all constant background phase offsets and can be used as

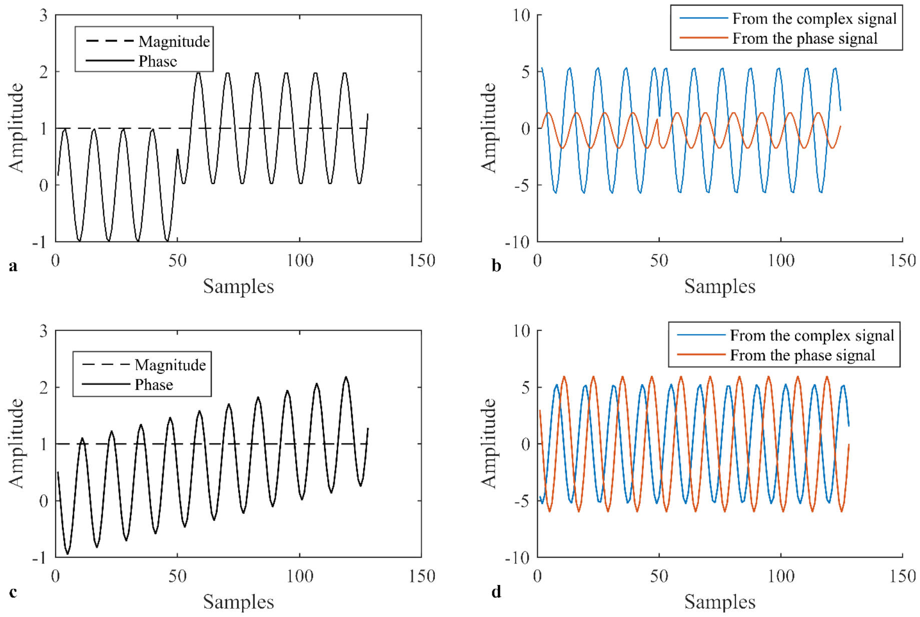

Figure 4.9 – Impact of the background phase. a) Input signal with a localized background phase variation and locally homogeneous background phase. b) Corresponding signal returned by the conventional method (in red) and the proposed method (in blue). c)Input signal with locally linear variation of the background phase. d) Corresponding signal returned by the conventional method (in red) and the proposed method (in blue).

an alternative processing requiring twice more images.

We previously mentioned that a high amplitude of the wave can be the cause of phase wrapping. High background phase can also result in phase wrapping. Let us take again the example of the signal with a zero-mean phase and a peak-to-peak amplitude of 2 rad (Fig.4.10a) and another signal with the phase that oscillates around 2.5 rad (Fig.4.10c). It is important to notice that the frequency spectrum of phase signal without (Fig.4.10b) or with (Fig.4.10.d) wrapping is totally different. Obviously, the presence of phase wrapping in the phase signal adds some frequency components to the phase signal. On the contrary, the frequency spectrum of the complex signal with a wrapped phase is identical to the complex signal without wrapped phase. In the conventional method, the temporal Fourier transform is applied on the phase image series. In the raw MRE method, the temporal Fourier transform is applied on the complex raw data. To compare the sensitivity of the two methods to phase wrapping due to background phase, both of them are applied on the described simulated signal (2 rad in peak-to-peak amplitude, 2.5 rad in average). In both cases, no phase unwrapping algorithm is applied. Results are shown in Fig.4.11. With the conventional method (in red), some of the components added by the presence of phase wrapping are removed by the temporal filtering but some of them remain if the number of dynamics N_t is not sufficient. With the raw MRE method (in blue), only the previously mentioned condition $R > 1$ must be satisfied and this condition is totally independent of

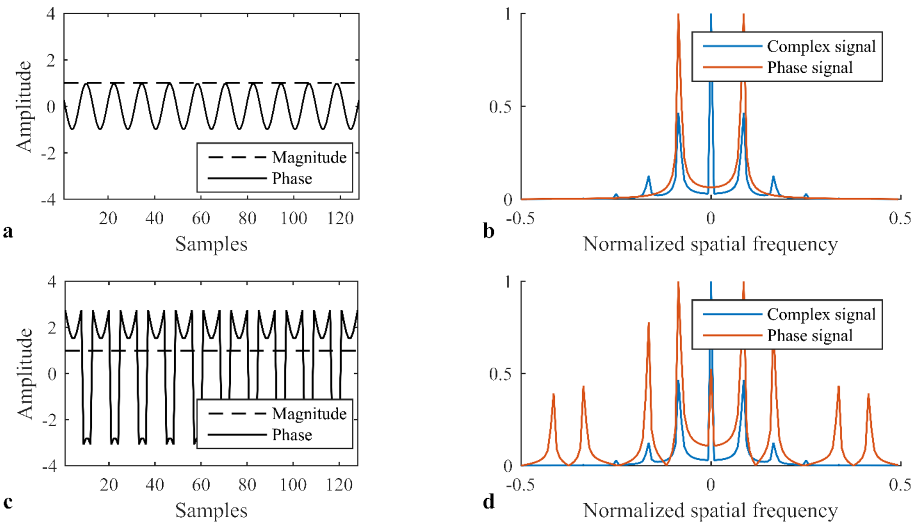

Figure 4.10 – Comparison of signals in the spatial and frequency domains (left and right columns respectively). a.b) Reference signal without phase wrapping, c.d) Signal with phase wrapping due to a Signal with phase wrapping due to a background phase Φ_0.

the potential background phase that is the source of the wrapping in this case. In this example, N_t is equal to 8, which is adequate enough to satisfy the condition $R > 1$ and the phase wrapping is removed.

4.2.5 Sensitivity to noise

This section is intended to evaluate the sensitivity to noise of the raw MRE method. The objective is to model the noise Ψ^{out} of the signal returned by the proposed method with respect to the characteristics of the noise Ψ of the acquired signal.
The acquired signal is defined as:

$$I(x,t) = I_0(x,t) + \psi(x,t) \tag{4.24}$$

with I_0 being the signal in the absence of noise. The resulting signal is described by:

$$w(x) = w_0(x) + \psi^{out}(x) \tag{4.25}$$

with w_0 being the signal returned by the proposed method in the absence of noise. The real and the imaginary parts of the noise in MRI have been shown to follow normal distributions with equal variances σ^2 and null averages. The random variables $\Psi^t_{re} = \{\psi_{re}(1,t), \psi_{re}(2,t), ...\}$ and $\Psi^t_{Im} = \{\psi_{Im}(1,t), \psi_{Im}(2,t), ...\}$ with $t \in [0, N_t \quad 1]$ refer to the real and imaginary parts of the noise Ψ acquired at each phase-offset t. Every Ψ^t_{re} and Ψ^t_{Im} are assumed to be uncorrelated. In the proposed method, a temporal Fourier

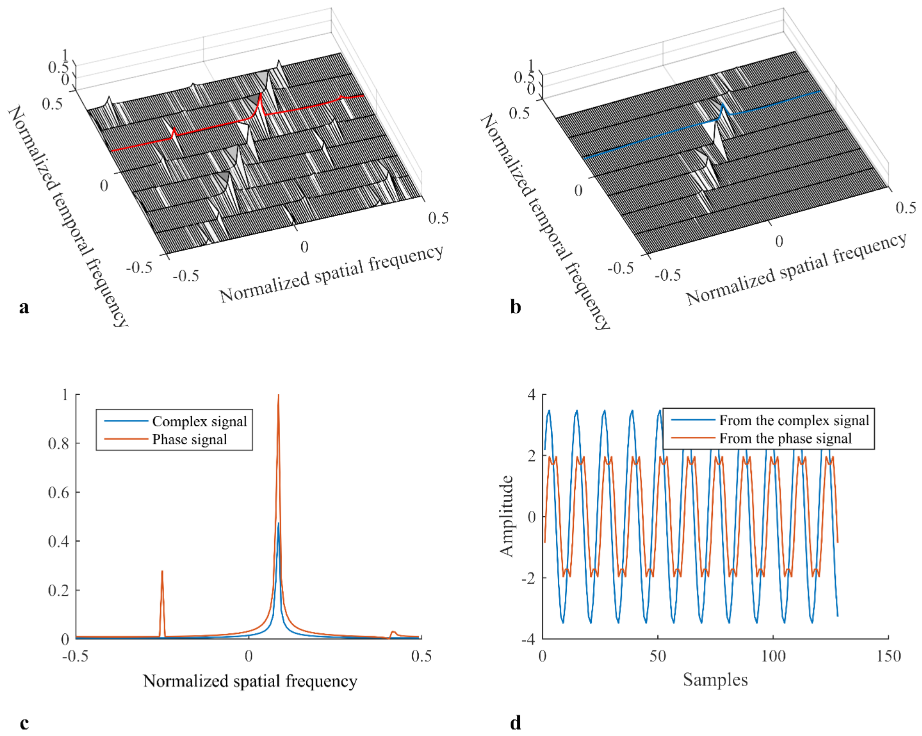

Figure 4.11 – Comparison of the efficiency of the conventional and the proposed methods applied to signals with phase wrapping due to a background phase. a) Phase signal in the spatio-temporal frequency domain. The selected frequency component is shown in red. b) Complex signal in the spatio-temporal frequency domain. The selected frequency component is shown in blue. c) Phase signal (in red) and complex signal (in blue) in the spatial frequency domain after temporal filtering. d) Signal returned y the conventional method (in red) and the proposed method (in blue).

transform is applied to the signal, as follows:

$$S(x,\nu_t) = \sum_{t=0}^{N_t-1} I_0(x,t)e^{-j2\pi\frac{\nu_t t}{N_t}} + \sum_{t=0}^{N_t-1} \psi_{re}(x,t)e^{-j2\pi\frac{\nu_t t}{N_t}} + i\sum_{t=0}^{N_t-1} \psi_{Im}(x,t)e^{-j2\pi\frac{\nu_t t}{N_t}} \tag{4.26}$$

Then, the imaginary part of the component at the temporal frequency of interest f_e (i.e $\nu_t = 1$) is observed:

$$w(x) = Im(S(x,1)) \tag{4.27}$$

$$= w_0(x) + \sum_{t=0}^{N_t-1} \psi_{re}(x,t)\sin(\frac{2\pi t}{N_t}) + \sum_{t=0}^{N_t-1} \psi_{Im}(x,t)\cos(\frac{2\pi t}{N_t}) \tag{4.28}$$

$$= w_0(x) + \psi^{out}(x) \tag{4.29}$$

It is well known that the linear combination of two independent variables normally distributed is a normal distribution:

Theorem 1. If $X_1 \sim \mathcal{N}(m_1, \sigma_1^2)$ and $X_2 \sim \mathcal{N}(m_2, \sigma_2^2)$ are independent, then $aX_1 +$

$bX_2 \sim \mathcal{N}(am_1 + bm_2, a^2\sigma_1^2 + b^2\sigma_2^2) \quad a, b \in \mathbf{R}$

The noise Ψ^{out} is therefore a zero-mean Gaussian noise with a variance σ_w related to the variance σ of the input noise:

$$\sigma_w^2 = \sum_{t=0}^{N_t\;\;1} \sigma^2 \sin^2(\frac{2\pi t}{N_t}) + \sum_{t=0}^{N_t\;\;1} \sigma^2 \cos^2(\frac{2\pi t}{N_t}) \tag{4.30}$$

$$= \sigma^2 \sum_{t=0}^{N_t\;\;1} (\sin^2(\frac{2\pi t}{N_t}) + \cos^2(\frac{2\pi t}{N_t})) \tag{4.31}$$

$$= \sigma^2 \sum_{t=0}^{N_t\;\;1} 1 \tag{4.32}$$

$$= \sigma^2 N_t \tag{4.33}$$

The noise resulting from the new method can be modeled as a gaussian distribution $\Psi^{out} \sim \mathcal{N}(0, \sigma^2 N_t)$.

We have run simulations with Matlab to confirm these results. The new method was applied on a simple 1D complex signal with a uniform magnitude:

$$I(x,t) = Me^{iC_1 cos(\;\frac{2\pi k_x x}{N_x} + \frac{2\pi t}{N_t})} + \psi(x,t) \tag{4.34}$$

with ψ being the gaussian noise with a variance σ^2. The variance σ_w of the noise included in the signal returned by the proposed method is computed. Simulations are repeated for increasing σ values ($\sigma \in [0.01, 0.5]$) and two numbers of phase-offsets N_t are tested ($N_t = 8$ and $N_t = 12$). Other parameters are fixed: $M = 1$AU,$C_1 = 3$ rad,$\frac{k_x}{N_x} = 1/12$. Fig.4.12 shows the relationship between the variances of the input noise σ and the output noise σ_w. As expected, the constant factor N_t is observed between the variances.

Other simulations were carried out to compare the sensitivity to noise of the proposed method to the conventional method. Let us remind that the conventional method refers to the method that consists in applying the temporal Fourier transform on phase images and select the real part of the frequency component of interest. In order to make the comparison relevant, the ratios between the standard deviation σ_w of the output noises and the amplitudes A of each resulting signal are investigated. Several cases were investigated:

- $N_t = 8$ and $M = 1$ (Fig.4.13a);
- $N_t = 8$ and $M = 3$ (Fig.4.13b);
- $N_t = 12$ and $M = 1$ (Fig.4.13c);
- $N_t = 12$ and $M = 3$ (Fig.4.13d);

Based on these simulations, several aspects must be discussed.

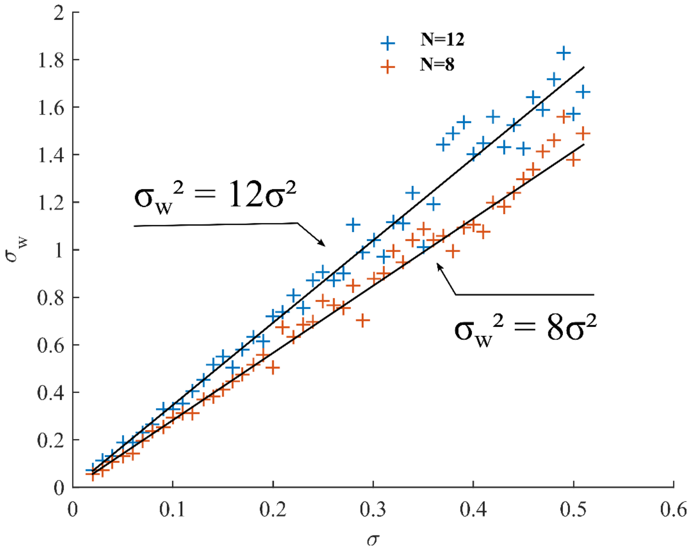

Figure 4.12 – Relationship between the standard deviation of the noise of the input signal, σ and the standard deviation of the noise of the signal returned by the proposed method, σ_w. Results come from simulated 1D signals described in Eq.(4.34).

- As opposed to the the proposed method, the conventional method does not allow to observe a linear relationship between the output noise and the input noise.
- The higher the magnitude of the input signal is, the smaller the ratio $\frac{\sigma_w}{A}$ obtained with the proposed method is. However, it has been previously shown that σ_w is independent of the magnitude of the input signal. However, the output signal is weighted by the magnitude, that is why the ratio $\frac{\sigma_w}{A}$ decreases.
- The relationship between the output noise and the input noise in the conventional method seems linear when the ratio $\frac{\sigma}{M}$ is high. In this region, the signal returned by the conventional method is less noisy than with the proposed method. In the others regions, the quality of the two signals are equivalent.

As detailed in [Gudbjartsson and Patz, 1995], the phase noise is not characterized by a gaussian distribution, which explains the non linear relationship between the output noise and the input noise in the conventional method. However, when the signal to noise ratio is high enough ($M >> \sigma$), the noise distribution can be considered as a zero mean Gaussian distribution with a variance equal to $\frac{\sigma}{M}$. The linear relationship observed on the previous simulations corresponds to this region.

4.2.6 Discussion

The raw MRE method offers the possibility of reconstructing wave pattern images and estimating elasticity without phase image reconstruction. The spatial frequencies of the

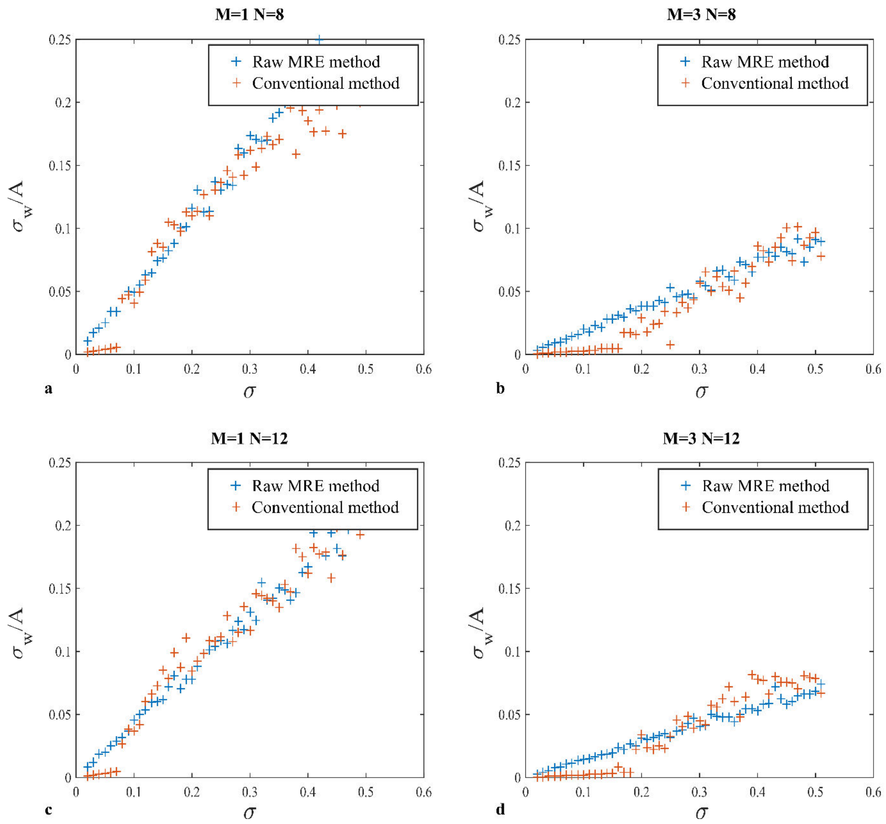

Figure 4.13 – Analysis of the ratios $\frac{\sigma_w}{A}$ obtained with the conventional method and the proposed method. Results come from simulated 1D signals described in Eq.(4.34). a)$N_t = 8$ and $M = 1$ b)$N_t = 8$ and $M = 3$ c) $N_t = 12$ and $M = 1$ d)$N_t = 12$ and $M = 3$

resulting signal are preserved, which allows estimating the shear modulus. Nevertheless, a fundamental condition is required. The number of phase-offsets N_t must be high enough to ensure the selection of the spatial frequency components of interest. The amplitude of all the harmonics out of interest that can be selected must be negligible. The number N_t only depends on the MRE wave amplitude C_1. As a result, as long as this condition is met, the wave pattern image can be reconstructed.

It must be emphasized that the wave pattern image is not exactly the signal that would be obtained with the conventional method. The amplitude of the wave pattern is weighted by the magnitude signal and also depends on the MRE wave amplitude C_1. However, this weighting does not modify the spatial frequencies, which are preserved.

The signal obtained by the raw MRE method also depends on the background phase, which includes a phase shift. This additional phase shift may be an issue when the variation is continuous. In this case, the background phase must be removed by a phase difference in the complex domain and data processing must be performed in the resulting data.

In conventional MRE, several phase unwrapping algorithms are used to unwrap phase images but most of them are not robust to noise [Wang et al., 2011]. More advanced algorithms suffer from long computation times. Phase wrapping in conventional MRE affects the wave images used for the final elastogram calculation. We have shown that the raw MRE method offers the possibility of reconstructing unwrapped wave pattern images without the need of phase unwrapping algorithm. Indeed, since the minimal number of phase-offsets N_t only depends on the C_1 parameter, the wave pattern image can be reconstructed as long as the condition $R > 1$ is met. The resulting wave pattern image is not corrupted by phase wrapping.

We have also shown in this section that the noise of the wave pattern image reconstructed with the raw MRE method only depends on the noise of the input raw data. On the contrary of the conventional method, the output noise does not depend on the magnitude of raw data.

4.3 Wave and elastogram reconstruction from MR images

4.3.1 Phantom experiments

We have evaluated the proposed method on a gelatin phantom (17 cm in diameter) made of two parts with different concentrations (4% and 8%). The commercial pneumatic surface exciter (Resoundant ®, Rochester, MN) was placed on the top of the phantom in order to generate shear waves. The experiment was performed in a 1.5 T MRI scanner (MAGNETOM Aera, Siemens, Germany) and bipolar motion encoding gradients were implemented in a spoiled gradient echo sequence. The body antenna was used to obtain a single channel data set. The excitation and the encoding frequencies were set to 120 Hz and 220 Hz respectively. The motion encoding direction was set through slice and the slice is parallel to the surface of the pneumatic exciter. 4 phase-offsets evenly spaced across a mechanical period were acquired. Main imaging parameters are the following: TE/TR 6.13 / 8.33 ms, FOV 340 mm × 340 mm, acquisition matrix 128 × 128, slice thickness 10 mm, MEG amplitude 20 mT/m. In order to compare the raw MRE method with the conventional one, raw data are processed in two different manners to reconstruct both the wave pattern image and the elastogram. The proposed raw MRE method is used as described previously to reconstruct the wave pattern image and the elastogram, both directly from the raw data without reconstructing nor the phase nor the amplitude image. The results obtained by the raw MRE method are compared to those obtained using 2 different versions of the conventional MRE processing method:

- **Method 1** A temporal Fourier transform is applied on the phase image series, the frequency component of interest is selected
- **Method 2** In addition to the process of the Method 1, a phase unwrapping algorithm is applied on the resulting image.

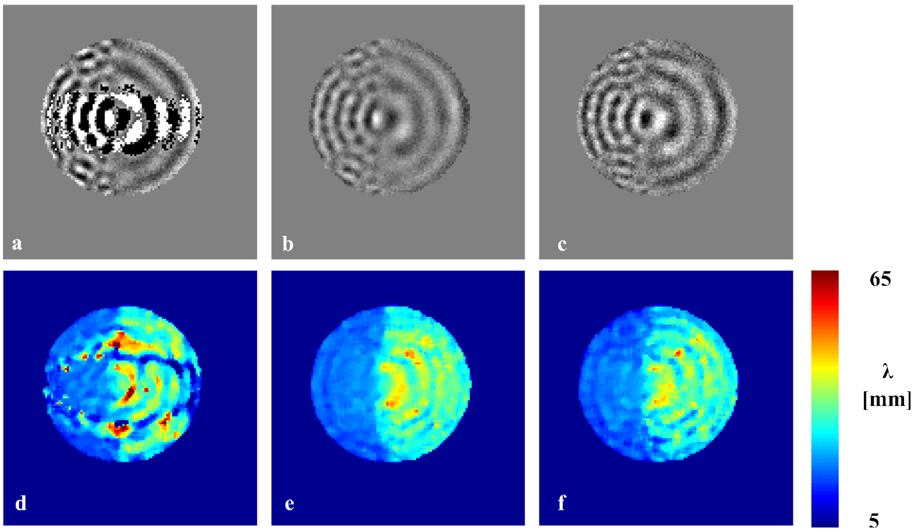

Figure 4.14 – (At the top) Wave images reconstructed by the conventional methods without (a) and with (b) phase unwrapping compared to the wave pattern image returned by the raw MRE method (c). (At the bottom) Elastograms reconstructed by the conventional methods without (d) and with (e) phase unwrapping compared to the one returned by the raw MRE method (f).

Please note that both methods are compared using the same number of phase-offsets images and that no phase difference image are used here.

4.3.2 In vivo experiments

In vivo experiments were performed on swine liver and were approved by the local ethics committee (ICOMETH C2EA - 38). The animal was anesthetized (propofol 3 mg kg ^{1}, pancuronium 0.2 mg kg ^{1} and isoflurane 2 %) and placed in the large bore 1.5 T scanner. The body antenna was used. The surface pneumatic exciter was strapped around the chest and one slice perpendicular to the surface exciter was acquired. Relevant parameters of acquisition include: excitation/encoding frequencies 40/90 Hz, encoding direction: through slice, slice thickness 10 mm, FOV 320 mm × 320 mm , acquisition matrix 128× 128, MEG amplitude 20 mT/m, TE/TR 12.7/25 ms. 4 images with different phase-offsets were acquired. The raw MRE method was compared to the Methods 1 and 2 in the same manner as in the phantom experiment.

4.3.3 Results

A comparison between the wave images obtained with the two conventional methods and the new approach based only on raw data is shown in Fig.4.14. Note that an amplitude image based mask is applied to select the phantom and facilitate comparisons. The proposed method allows reconstructing the wave pattern image without prior reconstruction of the phase image, circumventing thereby the challenging process of phase unwrapping. The

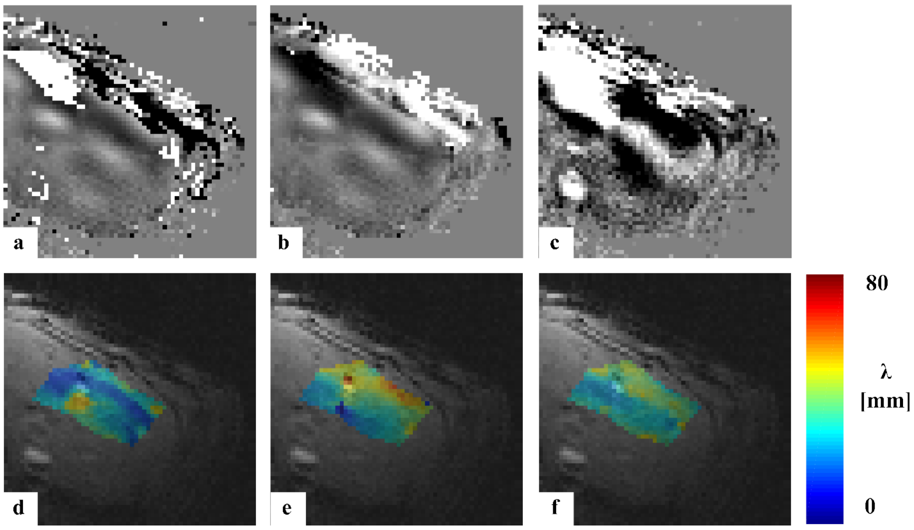

Figure 4.15 – (At the top) wave images reconstructed by the conventional methods without (a) and (b) with phase unwrapping compared to the wave pattern image returned by the raw MRE method (c). (At the bottom) Elastograms reconstructed by the conventional methods without (d) and (e) with phase unwrapping compared to the wave pattern image returned by the raw MRE method (f).

wave pattern image returned by the raw MRE method (Fig.4.14c) was found to be similar to the one returned by the conventional method with phase unwrapping (Fig.4.14b). It is important to highlight that the scale of the wave pattern reconstructed from the raw MRE data is different from the ones of conventional wave images because visualized data is not an angle value anymore but involves many parameters (Eq.(4.19)). The elastogram reconstructed from raw data is compared to the ones returned by the classic methods (Fig.4.14d-e-f). The elastogram reconstructed without phase unwrapping is strongly affected by the presence of phase wrapping while the elastograms resulting from the new method and the conventional method with phase unwrapping are equivalent. Mean values and standard deviations of the local wavelength estimation obtained with the raw MRE method and the conventional method with phase unwrapping are respectively 20.9 ± 10.9 mm, and 19.81 ± 10.7 mm in the left softer half and 30.7 ± 4.8 mm and 32.7 ± 3.8 mm in the right stiffer half.

Fig.4.15a-b-c shows results of the wave pattern images obtained in vivo by the different methods and Fig.4.15d-e-f shows the elastograms, similarly to what was observed in phantom experiments. The elastograms returned by method 1 is dramatically affected by phase wrapping. Local wavelength obtained by the raw MRE method and method 2 in the liver are equal to 36.3 ± 9.5 mm and 37.8 ± 10.8 mm, respectively. In both phantom and in vivo experiments, mean values and standard deviation of the local wavelength are equivalent for the proposed method and the conventional one on phase unwrapped MRE images.

4.3.4 Discussion

This study shows an alternative to the conventional processing protocol used in MRE. The phase reconstruction, the phase unwrapping and the spatial 2D transforms are circumvented limiting thereby potential sources of errors, sources of variability and saving computational and processing time. The raw data obtained during an MRE acquisition is not easily readable because of the infinite number of harmonics induced by the presence of one sinusoidal pattern in the phase signal. The solution proposed here to overcome this problem is to perform the harmonic analysis directly on raw data. Two independent outputs of our method were investigated in this section: the reconstruction of a wave pattern image and the direct reconstruction of elastograms, both without prior phase image reconstruction. Compared to conventional MRE process, this approach avoids MR phase reconstruction and phase unwrapping, and does not involve any additional processing steps (Fig.4.1). The method was assessed experimentally in gelatin phantoms and in vivo and results were found to be equivalent to those obtained with the conventional process with phase unwrapping.

Some aspects of the approach need to be discussed. As previously highlighted, this method is more sensitive to the choice of the number of phase-offsets. This number must be high enough to allow the selection of only one frequency component. However, in most cases, this condition is satisfied, as demonstrated in Section 4.2.3.

The second point that deserves to be mentioned is the assumption concerning the phase Φ_0 accumulated without motion encoding gradient. The present theory relies on the assumption that Φ_0 is locally homogeneous. Otherwise, the phase offset must be removed as also required in the conventional methods. In this case, the phase difference image must be performed in the complex domain (after or before the inverse spatial Fourier transform)(see Section 4.2.4).

Another difference between the conventional wave image and the wave pattern image returned by the proposed method is its weighting by the magnitude image. The shear modulus estimation will not be affected by this property because the spatial frequencies are preserved. However, it will not be possible to evaluate other parameters such as viscosity because the amplitude of the resulting wave is not the true wave amplitude.

The noise sensitivity analysis of the raw MRE method has shown that the output noise is easily related to the the input noise. When the signal to noise ratio is high, the benefit of the proposed method is reduced because the noise of the resulting wave is higher than the output noise of the conventional method. Contrary to the conventional method, the output noise of the wave pattern image does not depend on the magnitude of raw data but on the input noise.

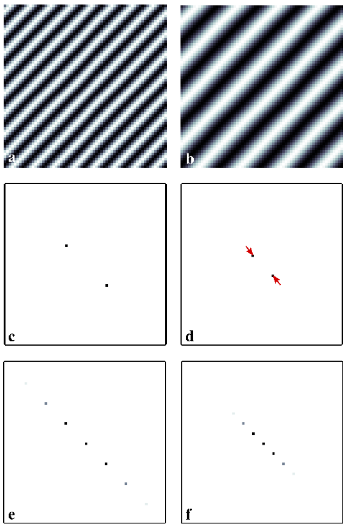

Figure 4.16 – Illustration of change in elasticity in the k-space. a)Wave pattern with a spatial frequency ν_a. b)Wave pattern with a spatial frequency ν_b. c-d) Frequency domains of real images respectively represented by (a) and (b). The frequency peaks are shifted along a radius (red arrows) when the spatial frequency varies. e-f) Frequency domain of complex images where the magnitudes are unitary matrix and the phases are respectively represented by (a) and (b). The wave pattern in the phase part of the image yields an infinity of harmonics in the frequency domain. All the components are shifted along the radius when the spatial frequency varies. In the frequency domain, only the magnitudes of the images are shown.

4.4 Variation of the raw MRE method for thermal ablation monitoring

The raw MRE method offers the possibility to reconstruct wave pattern images and elastograms from raw data without reconstructing any phase image. MRE is based on the analysis of elasticity map. A totally different approach based on the theory of the raw MRE method is proposed here to evaluate elasticity changes during a thermal ablation. No elastogram or wave pattern image is reconstructed , only the frequency domain is investigated. Two principles are involved: 1/ A change in elasticity is related to a change in the spatial frequency observed in the images because the wavelength depends on mechanical properties. 2/ The raw MR data contain all the information about spatial frequencies included in the MR image. The proposed method aims at observing peak changes in the raw data to evaluate temporal changes in elasticity during the thermal ablation. Each spatial frequency is associated to a location in the k-space. Intuitively, a change in elasticity would be related to the displacement of a frequency peak along a radius of the k-space (Fig.4.16c-d). The estimation of the frequency peak location is expected to provide quantitative information about the shear modulus μ according to the following expression $\mu = \rho(\frac{f_e}{k})^2$ with f_e being the excitation frequency and k being the spatial frequency. However, the spatial frequencies of interest are located in the phase of the MR image. As previously

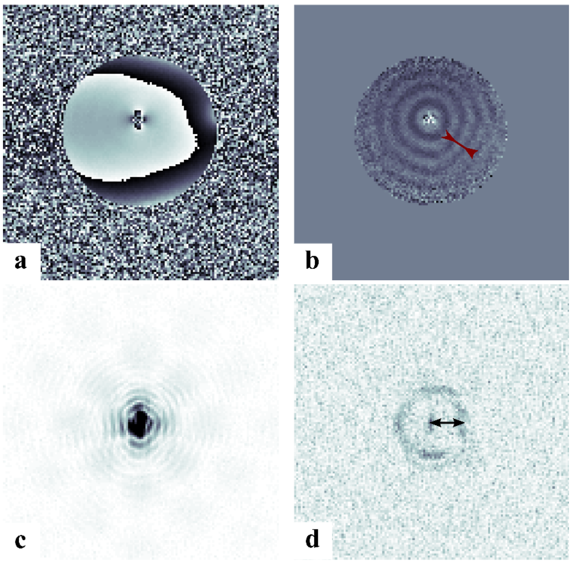

Figure 4.17 – Enhancement of the frequency of interest in the k-space. a)One MRE phase image of a gelatin phantom. b)Phase difference image reconstructed with the conventional method. c) Acquired MRE k-space raw data (in modulus) of one acquisition. d) k-space raw data (in modulus) after temporal Fourier transform and selection of the frequency of interest. This process makes a ring appear, which radius (black arrow in (d)) corresponds to the spatial frequency of the wave (inverse of the wavelength (red arrow in (b))).

demonstrated, sinusoidal patterns in the phase make an infinity of harmonics appear in the frequency domain (Fig.4.16e-f). As previously proposed, a temporal Fourier transform over a set of images with different phase-offsets can be applied to select only the components of interest. The displacements of the frequency peaks of interest can be measured in the resulting image. As shown in Fig.4.17, the spatial frequency components of the phase images are highlighted in the k-space raw data thanks to the temporal Fourier transform proposed by the raw MRE method. Given that spatial frequencies and shear modulus are closely linked, analyzing the spatial frequencies on raw data over time is expected to provide real-time elasticity information during a thermal ablation without reconstructing any wave image or using an inverse problem solver.

In order to assess the feasibility of the proposed method, the monitoring of the gelification of the gelatin was carried out.

4.4.1 Cartesian k-space filling

As previously described (Section 3.1), an approximately 4 cm hole in diameter was scooped out from a homogeneous gelatin phantom (8 %). The needle was inserted vertically in the phantom and held by a Plexiglas structure. A few minutes before the acquisition, a small volume (200 mL) of gelatin (15 %) was prepared and cooled down. The liquid was poured in the hole of the phantom and its solidification was monitored during 50 minutes. MRE images were acquired with the sequence described in section 2.2.2 (Beat-IRT with motion

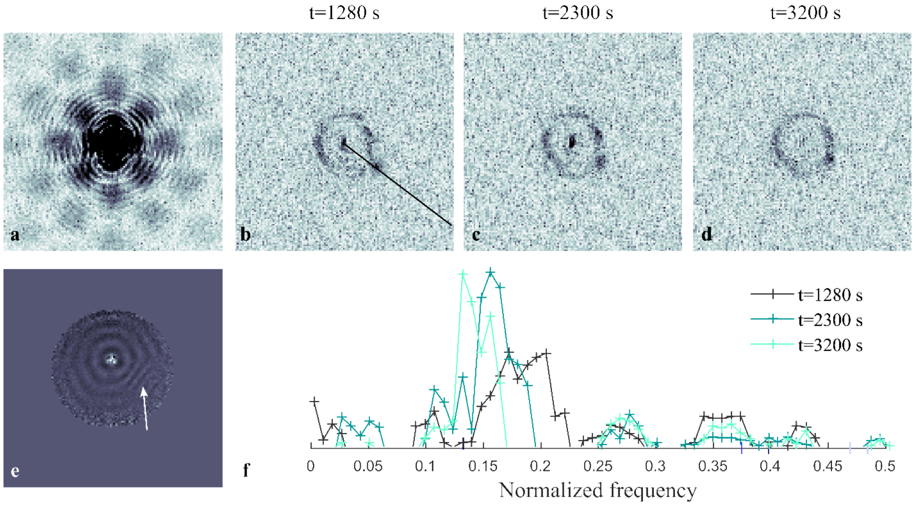

Figure 4.18 – Raw data processing for the monitoring of the gelification (cartesian k-space filling). a) Magnitude of the raw data of one acquisition. b-c-d)Magnitudes of the data after temporal filtering. Each image corresponds to a different time of the gelification. f)A 1D analysis was performed on the radius described by the black line in (b). The resulting profiles of the three images are plotted in (f). The tracking of the frequency peak is performed on these curves. e) Typical conventional wave image of the experiment. The wavelength in the gelifying inclusion (white arrow) increases over time.

encoding). Relevant imaging parameters include: excitation frequency 120 Hz, MEG frequency 290 Hz, MEG amplitude 20 mT/m, encoding direction: through slice, one slice orthogonal to the needle MRE driver, slice thickness 10 mm, FOV 300 mm×300 mm, acquisition matrix 128×128, TR/TE 8.34/5.62 ms, flip angle 15° and bandwidth frequency 380 Hz pixel ^{1}. 3 phase-offsets each with 2 opposite MEG polarities were acquired. However, the phase difference was not used for the raw data processing proposed here. The coil loop was used to obtain raw data arising from a single channel for simplicity. The temporal Fourier transform was applied to each raw data set of three consecutive acquisitions. Fig.4.18a shows the magnitude of raw data corresponding to one acquisition. Each group of three acquisitions (without taking into account the acquisition with opposite MEG polarity) yielded one image in the frequency domain after the selection of the excitation frequency. The spatial frequencies included in the conventional wave image (Fig.4.18e) become visible in the resulting k-space images (Fig.4.18b-c-d). A 1D-analysis was performed in this experiment to measure the displacement of the frequency peak corresponding to the varying wavelength in the gelifying inclusion. The barycentre of points around the maximum is assumed to be the location of the spatial frequency component observed in the wave pattern image. In order to evaluate the accuracy of the results, the more conventional process proposed in Chapter 2 was also applied to the data in the spatial domain and results of both methods were compared. The shear modulus estimates arise from a region of interest (10 pixels) of median filtered elastograms (4×4 kernel).

Wave images and elastograms obtained with the conventional method are similar to those

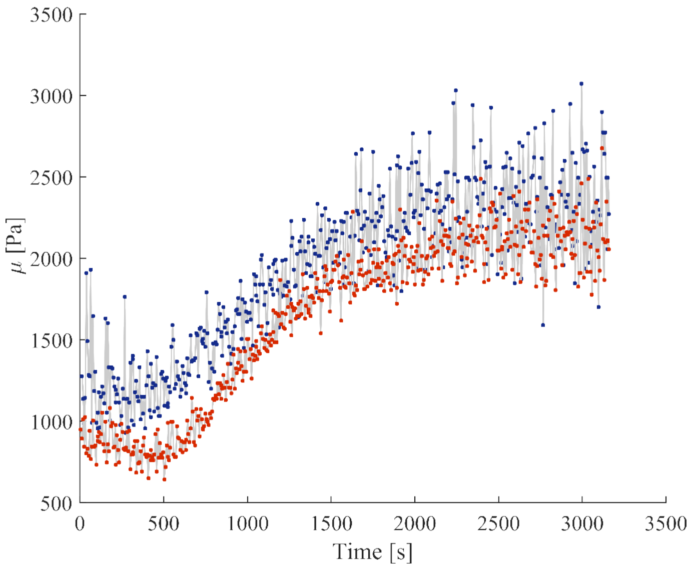

Figure 4.19 – Evolution of the shear modulus in the inclusion of 15% gelatin during its gelation observed with the proposed processing (in blue) and the interventional MRE method proposed in Chapter 2 (in red) (cartesian k-space filling).

obtained in the experiment described in Chapter 3. The wave propagates around the needle. The wavelength in the inclusion appears after some time and increases over time. The variation of the shear modulus obtained with both methods is plotted in Fig.4.19. The evolution of the shear modulus measured by the two methods are equivalent, whereas no inverse problem solver was required to obtain the variation of the shear modulus over the gelification duration. Only raw data were needed and two times less acquisitions were used (the acquisition with opposite MEG polarity is not used in this case). A small shift between the curves is observed. This shift can arise because the LFE algorithm underestimates the shear modulus due to the use of median filters and/or because the location of the peak in the raw MRE method is unprecise due to its spread. This possibility is developed in the discussion (Section 4.4.3).

4.4.2 Radial k-space filling

Given that all the data processing is performed in the frequency domain, optimizing the k-space filling is expected to increase the performance of the method. When a change in elasticity occurs, the displacement of the frequency peak is observed along one radius (assuming the wave propagation direction does not change). An interpolation over a radius is therefore required when a cartesian k-space filling is employed.

Hence, the radial acquisition seems the most appropriate for this method because radii are directly acquired. Furthermore, for the same acquisition duration as for the cartesian k-space filling, radial k space filling leads to a better sampling of low frequencies, which may result in a better accuracy in elasticity estimation. The same experiment was carried

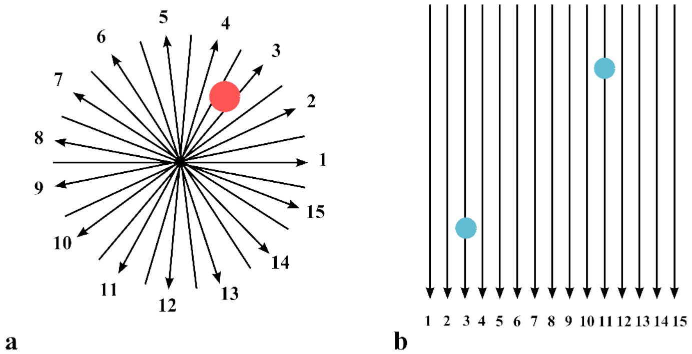

Figure 4.20 – Data collection scheme of the radial k-space filling. a) The k-space is filled with a series of diagonal lines traversing the center. b)The collected lines are arranged according to this scheme. As an example, frequency peaks located in a region (red) in the k-space will be observed in two parts (blue)in the frame of the collected data.

out with a radial k-space filling to evaluate the relevance of this alternative.
The experimental setup was equivalent to the one used for the experiment with cartesian k-space filling. The same MRE pulse sequence and MRE parameters were used. Data were collected using the loop coil. Radial acquisition was performed with 129 radii that were acquired according to the diagram in Fig.4.20. The parameters TR/TE were equal to 8.34/5 ms. Three phase-offsets were acquired in order to apply the temporal Fourier transform and enhance the frequency peak due to the mechanical excitation.

Typical raw data collected after the selection of the component of interest of the excitation frequency are represented in the images in Fig.4.21, each column representing a diameter of the frequency domain. The two symmetric horizontal lines are associated to the wavelength of the wave propagating in the stable gelatin. The region corresponding to the wavelength of the hardening inclusion moves towards the center along a column. Contrary to data acquired with a cartesian k-space filling, let us notice that two distinct regions corresponding to the wavelength in the inclusion are visible due to the manner in which the k-space is filled as explained in Fig.4.20. By analogy with the experiment carried out in the cartesian k-space, the frequency peak tracking over time is directly performed along one half column. A similar 1D analysis is performed and results are compared to the conventional MRE data processing.

Evolution of the shear modulus is shown in Fig.4.22. Results obtained from the previously described analysis are overlaid to the conventional results. Mean of μ in a region of interest in the inclusion is computed over time from reconstructed elastograms. This measurement is compared to the location of the moving frequency peak tracked over time.

Elasticity changes measured by the two methods are equivalent. The same shift as the

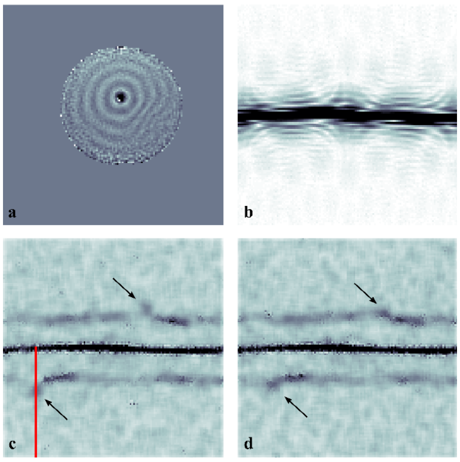

Figure 4.21 – Raw data processing for the monitoring of the gelification (radial k-space filling). a) Conventional phase difference image of the gelatin phantom. b) Magnitude of the raw data of one acquisition. c-d)Magnitudes of the data resulting from the temporal filtering. Each image corresponds to a different time of the gelification. A 1D analysis was performed on the half-column represented by the red line in (c).

one observed with the cartesian k-space filling is observed. Compared to the processing of data arising from cartesian acquisition, the data processing of radial acquisition is easier because the analysis is directly performed on a column and no interpolation is required.

4.4.3 Discussion

A new manner of recovering elasticity information is proposed here. It must be emphasized that this method is designed specifically for the monitoring of thermal ablations and is not suited for diagnostic MRE because it focuses on temporal evolution. Interventional MRE based on raw data has the advantage of minimizing the data processing for real-time monitoring. The main, substantial advantage of the proposed method is that no phase reconstruction, phase unwrapping, wave enhancement and even inverse problem solving is required. Radial k-space filling makes the data processing easier. Nevertheless, some limitations of this method must be discussed. First of all, spatial information is put aside and attention is only drawn to temporal elasticity changes. Then, let us recall that data analysis is performed here on acquisition arising from only one channel for this proof of concept. Further investigation is needed to extend this method to multi-channel acquisitions.

The fact that the resulting signal is weighted by the magnitude results in a limitation. In the previous experiments, the barycenter was assumed to be the location of the frequency component of interest. Let us remind that the image in the k-space resulting from the harmonic analysis is not only the phase image in the frequency domain but the frequency components of the product of the phase and the magnitude images. In the frequency domain, this product is associated to a convolution between the frequency components

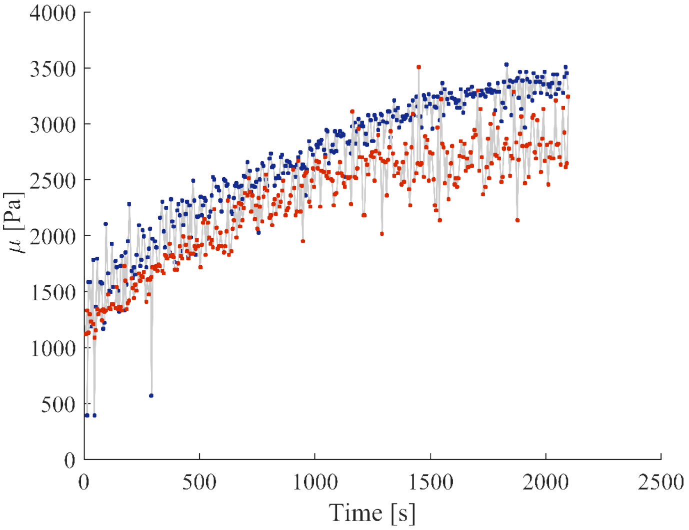

Figure 4.22 – Evolution of the shear modulus in the inclusion of 15% gelatin during its gelation observed with the proposed processing (in blue) and the interventional MRE method proposed in Chapter 2 (in red) (radial k-space filling).

of the magnitude and the phase. As a result, the tracked region is the spectrum of the magnitude shifted at the frequency peak of interest. The difficulty of determining the location of the frequency peak is illustrated in Fig.4.23. The phase of the simplified signal is the same in the two cases and associated to only one frequency component. In the first case, (Fig.4.23.a) the spectrum of the magnitude signal is assumed to be a small focal point at the center of the k-space. The image resulting from the temporal frequency filtering will be the convolution of the two images. In this case, the location of the frequency component of interest is easily estimated. However, in a more realistic case (Fig.4.23.b), the spectrum of the magnitude is more diffuse. In fact, the difficulty is the delineation of the region in which a barycenter will be calculated. It was proposed here to calculate the barycenter of a disk of a given diameter around a local maximum. This difficulty may be the cause of the shift observed between the curves obtained with the two methods.

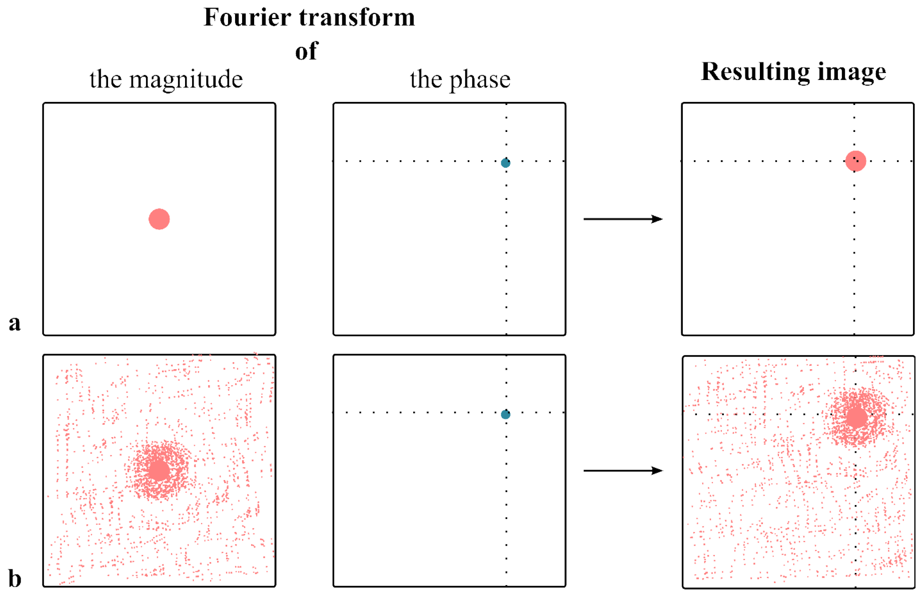

Figure 4.23 – Illustration of the influence of the magnitude signal in the frequency peak tracking. The data resulting from the temporal frequency filtering is the convolution between the frequency domains of the magnitude and phase signal in the frequency domain. a) The magnitude spectrum is focused in a well defined region. b) The magnitude spectrum is diffuse.

4.5 Conclusion

In summary, we have presented a new alternative to the standard MRE data processing. The raw MRE method allows reconstructing both elastograms and wave pattern images from raw MRI data. It circumvents several processing steps compared to conventional MRE. The feasibility of reconstructing elastograms and wave pattern images without computing any phase image was assessed in gelatin phantoms and in vivo. The modified version of the raw MRE method allows the monitoring of thermal ablation without reconstructing elastogram, based on the fact that all the information is included in the raw data. The method showed promising results in phantoms. Circumventing all the conventional steps of MRE data processing is expected to save time and gain in robustness and stability.

Conclusion

Today, many diseases that once required surgery can be treated less invasively by interventional radiologists. The patient comfort is improved and the complication rate is reduced. Nevertheless, it is challenging to replace the eyes and the hands of the physician. Conventional MR images are provided in real-time for visual guidance. Replacing the sense of touch is more challenging. For now, percutaneous thermal ablations used to destroy a cancerous tissue are controlled by analyzing changes in magnitude images and ensuring a sufficient increase in temperature. When a tissue is burned, the tissue is intuitively expected to be more rigid. Indeed, the increase in elasticity of ablated tissue has been demonstrated in the literature. MRI offers the possibility of non invasively measuring elasticity and hence providing this information in rigidity, conventionally obtained by palpation. Providing this information in real-time is expected to help the interventional radiologist to monitor the procedure with more accuracy. Nevertheless, measuring elasticity with MRI is not trivial and current systems do not allow for measuring elasticity in real-time during a thermal ablation.

This doctoral work aimed at investigating more-in-depth the feasibility of measuring elasticity in real-time by Magnetic Resonance Elastography. Current MRE systems are too slow and bulky to be used in interventional radiology. The first part of this work aimed at addressing this issue by developing an all-in-one MRE system dedicated to the monitoring of percutaneous thermal ablations. This system is composed of a needle MRE driver, a fast and interactive MR pulse sequence with motion encoding and a home-made inverse problem solver that reconstructs elasticity maps in real-time. Conventional MRE phase-offset number and reconstruction scheme were optimized for real-time elastogram reconstruction. The elastogram refresh rate obtained is one elastogram every 2 seconds ex vivo and 5 seconds in vivo. The feasibility of interventional MRE has been tested with the designed system. Changes in elasticity during the solidification of the gelatin were successfully measured in real-time. The laser ablation of a swine liver sample was monitored with the designed system. Elastograms reconstructed in real-time have offered the possibility of visualizing an increase in elasticity in the ablated region during the procedure. The monitoring of in vivo ablations was more challenging, especially because of the respiratory motion. Refinements of the system in terms of motion compensation have allow us to successfully monitor laser thermal ablations of the liver in vivo. For the first time, in vivo thermal ablation was monitored by simultaneous MR elastography and MR thermometry with a refresh rate of one elastogram with every breathing cycle, i.e. every 5 seconds. However, the evaluation of the confidence in the results was one of the main difficulties of this work because of the lack of ground truth. It was extremely difficult to validate the results obtained during the experiments because the true value could not be known.

The second part of the thesis aimed at investigating a new method of MRE data processing. Conventional MRE relies on the reconstruction and processing of phase images. MRE data processing requires several steps, each of which can be addressed in various ways, hence creating a variability in conventional MRE results. An alternative method for MRE data processing has been developed during this doctoral work. Preliminary work has shown the capability of the method to reconstruct wave pattern images and elastograms from raw data while avoiding phase image reconstruction and unwrapping. Limitations of the method were also investigated in details. The use of this MRE method free of phase image was investigated for real-time MRE. The process is pushed further and no elastogram is reconstructed here, the time evolution of elasticity alone is monitored. The monitoring of the solidification of the gelatin was directly performed on raw data without reconstructing any images. Similar results were returned while avoiding numerous steps of data processing. Although the method is not mature yet, the developed theory and the preliminary results encourage to look deeper into this alternative.

Bibliography

[Arnal et al., 2011] Arnal, B., Pernot, M., and Tanter, M. (2011). Monitoring of thermal therapy based on shear modulus changes: II. Shear wave imaging of thermal lesions. *IEEE Transactions on Ultrasonics, Ferroelectrics, and Frequency Control*, 58(8):1603–1611. (page 37), (page 38)

[Asbach et al., 2008] Asbach, P., Klatt, D., Hamhaber, U., Braun, J., Somasundaram, R., Hamm, B., and Sack, I. (2008). Assessment of liver viscoelasticity using multifrequency MR elastography. *Magnetic Resonance in Medicine*, 60(2):373–379. (page 51)

[Asbach et al., 2010] Asbach, P., Klatt, D., Schlosser, B., Biermer, M., Muche, M., Rieger, A., Loddenkemper, C., Somasundaram, R., Berg, T., Hamm, B., Braun, J., and Sack, I. (2010). Viscoelasticity-based staging of hepatic fibrosis with multifrequency MR elastography. *Radiology*, 257(1):80–86. (page 35), (page 48)

[Barnhill et al., 2014] Barnhill, E., Kennedy, P., Johnson, C. L., Mada, M., and Roberts, N. (2014). Real-time 4d phase unwrapping applied to magnetic resonance elastography. *Magnetic Resonance in Medicine*, 73(6):2321–2331. (page 60)

[Bensamoun et al., 2015] Bensamoun, S., Charleux, F., Debernard, L., Themar-Noel, C., and Voit, T. (2015). Elastic properties of skeletal muscle and subcutaneous tissues in Duchenne muscular dystrophy by magnetic resonance elastography (MRE): A feasibility study. *IRBM*, (1):4–9. (page 36)

[Bensamoun et al., 2006] Bensamoun, S., Ringleb, S., Littrell, L., Chen, Q., Brennan, M., Ehman, R., and An, K.-N. (2006). Determination of thigh muscle stiffness using magnetic resonance elastography. *Journal of Magnetic Resonance Imaging*, 23(2):242–247. (page 42)

[Bercoff et al., 2004] Bercoff, J., Pernot, M., Tanter, M., and Fink, M. (2004). Monitoring Thermally-Induced Lesions with Supersonic Shear Imaging. *Ultrasonic Imaging*, 26(2):71–84. (page 37)

[Bernstein et al., 2004] Bernstein, M. A., King, K. F., and Zhou, X. J. (2004). *Handbook of MRI Pulse Sequences*. Elsevier. (page 24), (page 56)

[Bieri et al., 2006] Bieri, O., Maderwald, S., Ladd, M., and Scheffler, K. (2006). Balanced alternating steady-state elastography. *Magnetic Resonance in Medicine*, 55(2):233–241. (page 51)

[Boashash, 1992] Boashash, B. (1992). Estimating and interpreting the instantaneous frequency of a signal. I. Fundamentals. *Proceedings of the IEEE*, 80(4):520–538. (page 62)

[Brace et al., 2011] Brace, C., Hinshaw, J., and Lubner, M. (2011). Thermal ablation for the treatment of abdominal tumors. *Journal of visualized experiments : JoVE*, (49). (page 6)

[Brace, 2010] Brace, C. L. (2010). Microwave Tissue Ablation: Biophysics, Technology and Applications. *Critical reviews in biomedical engineering*, 38(1):65–78. (page 7)

[Braun et al., 2003] Braun, J., Braun, K., and Sack, I. (2003). Electromagnetic actuator for generating variably oriented shear waves in MR elastography. *Magnetic Resonance in Medicine*, 50(1):220–222. (page 42)

[Braun et al., 2015] Braun, J., Hirsch, S., Heinze, T., and Sack, I. (2015). Feasibility of a new actuator type for magnetic resonance elastography based on transient air pressure impulses. In *Proc. Intl. Soc. Mag. Reson. Med. 23Proc.* (page 42)

[Brown et al., 2014] Brown, R. W., Cheng, Y.-C. N., Haacke, E. M., Thompson, M. R., and Venkatesan, R. (2014). *Magnetic Resonance Imaging: Physical Principles and Sequence Design*. John Wiley & Sons. (page 15), (page 58)

[Busch et al., 1998] Busch, M., Bornstedt, A., Wendt, M., Duerk, J., Lewin, J., and Grönemeyer, D. (1998). Fast 'real time' imaging with different k-space update strategies for interventional procedures. *Journal of Magnetic Resonance Imaging*, 8(4):944–954. (page 24)

[Chan et al., 2006] Chan, Q., Li, G., Ehman, R., Grimm, R., Li, R., and Yang, E. (2006). Needle shear wave driver for magnetic resonance elastography. *Magnetic Resonance in Medicine*, 55(5):1175–1179. (page 44), (page 45), (page XIII)

[Chen et al., 2013] Chen, J., Woodrum, D. A., Glaser, K. J., Murphy, M. C., Gorny, K., and Ehman, R. (2013). Assessment of in vivo laser ablation using MR elastography with an inertial driver. *Magnetic Resonance in Medicine*, pages 72:59–67. (page 37), (page 39), (page 45)

[Chen et al., 2010] Chen, M., Li, S.-Y., Wang, W.-C., Zhao, W.-F., Yang, Z.-H., Liu, M., and Zhou, C. (2010). The clinical value of MR elastography in the diagnosis of prostate cancer. *Chinese Journal of Radiology*, 44(8):816–818. (page 35)

[Cheng et al., 2011] Cheng, S., Gandevia, S., Green, M., Sinkus, R., and Bilston, L. (2011). Viscoelastic properties of the tongue and soft palate using MR elastography. *Journal of Biomechanics*, 44(3):450–454. (page 36)

[Chopra et al., 2009] Chopra, R., Arani, A., Huang, Y., Musquera, M., Wachsmuth, J., Bronskill, M., and Plewes, D. (2009). In vivo MR elastography of the prostate gland using a transurethral actuator. *Magnetic Resonance in Medicine*, 62(3):665–671. (page 44)

[Clasen and Pereira, 2008] Clasen, S. and Pereira, P. (2008). Magnetic resonance guidance for radiofrequency ablation of liver tumors. *Journal of Magnetic Resonance Imaging*, 27(2):421–433. (page 6)

[Colton and Kress, 1998] Colton, D. and Kress, R. (1998). *Inverse Acoustic and Electromagnetic Scattering Theory*. Springer Science & Business Media. (page 94)

[de Bazelaire et al., 2004] de Bazelaire, C. M. J., Duhamel, G. D., Rofsky, N. M., and Alsop, D. C. (2004). MR imaging relaxation times of abdominal and pelvic tissues measured in vivo at 3.0 T: preliminary results. *Radiology*, 230(3):652–659. (page 58)

[Depoorter et al., 1994] Depoorter, J., Dewagter, C., Dedeene, Y., Thomsen, C., Stahlberg, F., and Achten, E. (1994). The Proton-Resonance-Frequency-Shift Method Compared with Molecular Diffusion for Quantitative Measurement of Two-Dimensional Time-Dependent Temperature Distribution in a Phantom. *Journal of Magnetic Resonance, Series B*, 103(3):234–241. (page 68)

[Deshmane et al., 2012] Deshmane, A., Gulani, V., Griswold, M., and Seiberlich, N. (2012). Parallel MR imaging. *Journal of Magnetic Resonance Imaging*, 36(1):55–72. (page 24)

[Dick et al., 2003] Dick, E. A., Joarder, R., de Jode, M., Taylor-Robinson, S. D., Thomas, H. C., Foster, G. R., and Gedroyc, W. M. W. (2003). MR-guided Laser Thermal Ablation of Primary and Secondary Liver Tumours. *Clinical Radiology*, 58(2):112–120. (page 7)

[Dresner et al., 2004] Dresner, M. A., Fidler, J. L., and Ehman, R. L. (2004). MR elastography of in vivo human liver. In *Proceedings of the 12th Annual Meeting of the International Society for Magnetic Resonance in Medicine, Kyoto, Japan*, page 502. (page 42)

[Duerk et al., 1996] Duerk, J., Lewin, J., and Wu, D. (1996). Application of keyhole imaging to interventional MRI: A simulation study to predict sequence requirements. *Journal of Magnetic Resonance Imaging*, 6(6):918–924. (page 24)

[Elgeti et al., 2010a] Elgeti, T., Beling, M., Hamm, B., Braun, J., and Sack, I. (2010a). Cardiac magnetic resonance elastography: Toward the diagnosis of abnormal myocardial relaxation. *Investigative Radiology*, 45(12):782–787. (page 36)

[Elgeti et al., 2010b] Elgeti, T., Beling, M., Hamm, B., Braun, J., and Sack, I. (2010b). Elasticity-based determination of isovolumetric phases in the human heart. *Journal of Cardiovascular Magnetic Resonance*, 12(1). (page 50)

[Gallichan et al., 2009] Gallichan, D., Robson, M., Bartsch, A., and Miller, K. (2009). TREMR: Table-resonance elastography with MR. *Magnetic Resonance in Medicine*, 62(3):815–821. (page 43)

[Garteiser et al., 2012] Garteiser, P., Doblas, S., Daire, J.-L., Wagner, M., Leitao, H., Vilgrain, V., Sinkus, R., and Van Beers, B. (2012). MR elastography of liver tumours: Value of viscoelastic properties for tumour characterisation. *European Radiology*, 22(10):2169–2177. (page 35)

[Goldberg et al., 2009] Goldberg, S. N., Grassi, C. J., Cardella, J. F., Charboneau, J. W., Dodd, 3rd, G. D., Dupuy, D. E., Gervais, D. A., Gillams, A. R., Kane, R. A., Lee, Jr, F. T., Livraghi, T., McGahan, J., Phillips, D. A., Rhim, H., Silverman, S. G., Solbiati, L., Vogl, T. J., Wood, B. J., Vedantham, S., Sacks, D., and Society of Interventional Radiology Technology Assessment Committee and the International Working Group on Image-guided Tumor Ablation (2009). Image-guided tumor ablation: standardization of terminology and reporting criteria. *Journal of vascular and interventional radiology: JVIR*, 20(7 Suppl):S377–390. (page 9)

[Goldstein et al., 1988] Goldstein, R. M., Zebker, H. A., and Werner, C. L. (1988). Satellite radar interferometry: two-dimensional phase unwrapping. *Radio Science*, 23(4):713–720. (page 64)

[Gough-Palmer and Gedroyc, 2008] Gough-Palmer, A. L. and Gedroyc, W. M. W. (2008). Laser ablation of hepatocellular carcinoma-A review. *World Journal of Gastroenterology : WJG*, 14(47):7170–7174. (page 7)

[Gudbjartsson and Patz, 1995] Gudbjartsson, H. and Patz, S. (1995). The Rician Distribution of Noisy MRI Data. *Magnetic resonance in medicine : official journal of the Society of Magnetic Resonance in Medicine / Society of Magnetic Resonance in Medicine*, 34(6):910–914. (page 108)

[Herzka et al., 2009] Herzka, D., Kotys, M., Sinkus, R., Pettigrew, R., and Gharib, A. (2009). Magnetic resonance elastography in the liver at 3 Tesla using a second harmonic approach. *Magnetic Resonance in Medicine*, 62(2):284–291. (page 50)

[Hildebrandt et al., 2002] Hildebrandt, B., Wust, P., Ahlers, O., Dieing, A., Sreenivasa, G., Kerner, T., Felix, R., and Riess, H. (2002). The cellular and molecular basis of hyperthermia. *Critical Reviews in Oncology/Hematology*, 43(1):33–56. (page 5), (page 7)

[Holm and Skjoldbye, 1996] Holm, H. H. and Skjoldbye, B. (1996). Interventional ultrasound. *Ultrasound in Medicine & Biology*, 22(7):773–789. (page 10), (page 11)

[Huwart et al., 2006] Huwart, L., Peeters, F., Sinkus, R., Annet, L., Salameh, N., ter Beek, L., Horsmans, Y., and Van Beers, B. (2006). Liver fibrosis: Non-invasive assessment with MR elastography. *NMR in Biomedicine*, 19(2):173–179. (page 35)

[Huwart et al., 2008] Huwart, L., Salameh, N., ter Beek, L., Vicaut, E., Peeters, F., Sinkus, R., and Van Beers, B. (2008). MR elastography of liver fibrosis: Preliminary results comparing spin-echo and echo-planar imaging. *European Radiology*, 18(11):2535–2541. (page 48)

[Kahn and Busse, 2012] Kahn, T. and Busse, H. (2012). *Interventional Magnetic Resonance Imaging*. Springer. (page XI)

[Kearney et al., 2015] Kearney, S., Brinker, S., Burns, D., Royston, T., and Klatt, D. (2015). Slim-mre without prolonged echo time for the simultaneous acquisition of the 3d displacement vector applied to in vivo mouse brain. In *Proc. Intl. Soc. Mag. Reson. Med*, volume 23, page 1054. (page 51)

[Kim et al., 2008] Kim, Y.-s., Rhim, H., Choi, M. J., Lim, H. K., and Choi, D. (2008). High-Intensity Focused Ultrasound Therapy: an Overview for Radiologists. *Korean Journal of Radiology*, 9(4):291–302. (page 8)

[Klatt et al., 2013] Klatt, D., Yasar, T., Royston, T., and Magin, R. (2013). Sample interval modulation for the simultaneous acquisition of displacement vector data in magnetic resonance elastography: Theory and application. *Physics in Medicine and Biology*, 58(24):8663–8675. (page 51)

[Knutsson et al., 1994] Knutsson, H., Westin, C. F., and Granlund, G. (1994). Local multiscale frequency and bandwidth estimation. In *Image Processing, 1994. Proceedings. ICIP-94., IEEE International Conference*, volume 1, pages 36–40 vol.1. (page 61), (page XIV)

[Kolipaka et al., 2012] Kolipaka, A., Aggarwal, S., McGee, K., Anavekar, N., Manduca, A., Ehman, R., and Araoz, P. (2012). Magnetic resonance elastography as a method to estimate myocardial contractility. *Journal of Magnetic Resonance Imaging*, 36(1):120–127. (page 50)

[Larrat et al., 2010] Larrat, B., Pernot, M., Aubry, J.-F., Dervishi, E., Sinkus, R., Seilhean, D., Marie, Y., Boch, A.-L., Fink, M., and Tanter, M. (2010). MR-guided transcranial brain HIFU in small animal models. *Physics in Medicine and Biology*, 55(2):365–388. (page 37)

[Le et al., 2006] Le, Y., Glaser, K., Rouviere, O., Ehman, R., and Felmlee, J. P. (2006). Feasibility of simultaneous temperature and tissue stiffness detection by MRE. *Magnetic Resonance in Medicine*, 55(3):700–705. (page 67), (page XIV)

[Lee et al., 2012] Lee, C., Glockner, J., Glaser, K., Yin, M., Chen, J., Kawashima, A., Kim, B., Kremers, W., Ehman, R., and Gloor, J. (2012). MR Elastography in Renal Transplant Patients and Correlation with Renal Allograft Biopsy. A Feasibility Study. *Academic Radiology*, 19(7):834–841. (page 48)

[Lewa et al., 2000] Lewa, C. J., Roth, M., Nicol, L., Franconi, J. M., and de Certaines, J. D. (2000). A new fast and unsynchronized method for MRI of viscoelastic properties of soft tissues. *Journal of magnetic resonance imaging: JMRI*, 12(5):784–789. (page 42)

[Li et al., 2014] Li, B. N., Shan, X., Xiang, K., An, N., Xu, J., Huang, W., and Kobayashi, E. (2014). Evaluation of robust wave image processing methods for magnetic resonance elastography. *Computers in Biology and Medicine*, 54:100–108. (page 59)

[Li and Wu, 2013] Li, S. and Wu, P.-H. (2013). Magnetic resonance image-guided versus ultrasound-guided high-intensity focused ultrasound in the treatment of breast cancer. *Chinese Journal of Cancer*, 32(8):441–452. (page 11)

[Litwiller et al., 2010] Litwiller, D., Lee, S., Kolipaka, A., Mariappan, Y., Glaser, K., Pulido, J., and Ehman, R. (2010). MR elastography of the ex vivo bovine globe. *Journal of Magnetic Resonance Imaging*, 32(1):44–51. (page 36)

[Madersbacher et al., 1995] Madersbacher, S., Pedevilla, M., Vingers, L., Susani, M., and Marberger, M. (1995). Effect of high-intensity focused ultrasound on human prostate cancer in vivo. *Cancer Research*, 55(15):3346–3351. (page 8)

[Manduca et al., 2003] Manduca, A., Lake, D., Kruse, S., and Ehman, R. (2003). Spatio-temporal directional filtering for improved inversion of MR elastography images. *Medical Image Analysis*, 7(4):465–473. (page 60)

[Manduca et al., 1996] Manduca, A., Muthupillai, R., Rossman, P., Greenleaf, J., and Ehman, R. (1996). Local wavelength estimation for magnetic resonance elastography. In *, International Conference on Image Processing, 1996. Proceedings*, volume 3, pages 527–530 vol.3. (page 61)

[Manduca et al., 2001] Manduca, A., Oliphant, T., Dresner, M., Mahowald, J., Kruse, S., Amromin, E., Felmlee, J., Greenleaf, J., and Ehman, R. (2001). Magnetic resonance elastography: Non-invasive mapping of tissue elasticity. *Medical Image Analysis*, 5(4):237–254. (page 62), (page XIV)

[Mariani et al., 2014] Mariani, A., Kwiecinski, W., Pernot, M., Balvay, D., Tanter, M., Clement, O., Cuenod, C. A., and Zinzindohoue, F. (2014). Real time shear waves elastography monitoring of thermal ablation: in vivo evaluation in pig livers. *Journal of Surgical Research*, 188(1):37–43. (page 37)

[Mertyna et al., 2009] Mertyna, P., Goldberg, W., Yang, W., and Goldberg, S. N. (2009). Thermal Ablation: A Comparison of Thermal Dose Required for Radiofrequency-, Microwave- and Laser-induced Coagulation in an Ex-vivo Bovine Liver Model. *Academic radiology*, 16(12):1539–1548. (page 29)

[Morikawa et al., 2002] Morikawa, S., Inubushi, T., Kurumi, Y., Naka, S., Sato, K., Tani, T., Yamamoto, I., and Fujimura, M. (2002). MR-guided microwave thermocoagulation therapy of liver tumors: Initial clinical experiences using a 0.5 T open MR system. *Journal of Magnetic Resonance Imaging*, 16(5):576–583. (page 11)

[Morrison et al., 2008] Morrison, P. R., Silverman, S. G., Tuncali, K., and Tatli, S. (2008). MRI-guided cryotherapy. *Journal of Magnetic Resonance Imaging*, 27(2):410–420. (page 12)

[Murphy et al., 2012] Murphy, M., Curran, G., Glaser, K., Rossman, P., Huston, J., Poduslo, J., Jack, C., Felmlee, J., and Ehman, R. (2012). Magnetic resonance elastography of the brain in a mouse model of Alzheimer's disease: Initial results. *Magnetic Resonance Imaging*, 30(4):535–539. (page 36)

[Murphy et al., 2010] Murphy, M., Glaser, K., Manduca, A., Felmlee, J., Huston, J., and Ehman, R. (2010). Analysis of time reduction methods for magnetic resonance elastography of the brain. *Magnetic Resonance Imaging*, 28(10):1514–1524. (page 51)

[Muthupillai et al., 1995] Muthupillai, R., Lomas, D., Rossman, P., Greenleaf, J., Manduca, A., and Ehman, R. (1995). Magnetic resonance elastography by direct visualization of propagating acoustic strain waves. *Science*, 269(5232):1854–1857. (page XI)

[Muthupillai et al., 1996] Muthupillai, R., Rossman, P. J., Lomas, D. J., Greenleaf, J. F., Riederer, S. J., and Ehman, R. L. (1996). Magnetic resonance imaging of transverse acoustic strain waves. *Magnetic Resonance in Medicine*, pages 266–274. (page 35), (page 47)

[Nolsøe et al., 1993] Nolsøe, C. P., Torp-Pedersen, S., Burcharth, F., Horn, T., Pedersen, S., Christensen, N. E., Olldag, E. S., Andersen, P. H., Karstrup, S., and Lorentzen, T.

(1993). Interstitial hyperthermia of colorectal liver metastases with a US-guided Nd-YAG laser with a diffuser tip: a pilot clinical study. *Radiology*, 187(2):333–337. (page 11)

[Numano et al., 2015] Numano, T., Mizuhara, K., Hata, J., Washio, T., and Homma, K. (2015). A simple method for MR elastography: a gradient-echo type multi-echo sequence. *Magnetic Resonance Imaging*, 33(1):31–37. (page 51)

[Oliphant et al., 2001] Oliphant, T. E., Manduca, A., Ehman, R. L., and Greenleaf, J. F. (2001). Complex-valued stiffness reconstruction for magnetic resonance elastography by algebraic inversion of the differential equation. *Magnetic Resonance in Medicine*, pages 299–310. (page 60)

[Ozenne et al., 2015] Ozenne, V., Toupin, S., Denis de Senneville, D., Bour, P., Vaillant, F., Lepetit-Coiffé, M., Jaïs, P., and Quesson, B. (2015). Motion correction strategies for cardiac MR thermometry during RF-ablation. In *ISMRM, Toronto*, page 0042. (page 58)

[Pan et al., 2011] Pan, L., Barbot, J., Shea, S. M., Patil, S., Kirchberg, K. J., Meredith, G., Meng, T., Kholmovski, E. G., Vijayakumar, S., and Vij, K. (2011). An integrated system for catheter tracking and visualization in MR-guided cardiovascular interventions. In *Proc. Intl. Soc. Mag. Reson. Med*, volume 19, page 195. (page 27), (page XIII)

[Parker et al., 1983] Parker, D. L., Smith, V., Sheldon, P., Crooks, L. E., and Fussell, L. (1983). Temperature distribution measurements in two-dimensional NMR imaging. *Medical Physics*, 10(3):321–325. (page 27)

[Quesson et al., 2000] Quesson, B., de Zwart, J. A., and Moonen, C. T. (2000). Magnetic resonance temperature imaging for guidance of thermotherapy. *Journal of Magnetic Resonance Imaging*, 12(4):525–533. (page 11), (page 27)

[Riek et al., 1993] Riek, J. K., Tekalp, A., and Smith, W. E. (1993). Effect of z-motion in the phase of the k-space MRI data and identification of periodic z-motion kernels. volume 5, pages V–511–V–514. (page 95)

[Rossi et al., 1993] Rossi, S., Fornari, F., and Buscarini, L. (1993). Percutaneous ultrasound-guided radiofrequency electrocautery for the treatment of small hepatocellular carcinoma. *Journal of Interventional Radiology*, 8(3):97–103. (page 11)

[Rossman et al., 1999] Rossman, P. J., Muthupillai, R., and Ehman, R. (1999). Driver device for MR elastography. Classification aux États-Unis 324/318; Classification internationale G01R33/28, G01R33/563, A61B5/055; Classification coopérative G01R33/563, A61B5/0048, G01R33/28, A61B5/055, G01R33/56358; Classification européenne A61B5/00M, G01R33/28, A61B5/055, G01R33/563M. (page 42)

[Rump et al., 2007] Rump, J., Klatt, D., Braun, J., Warmuth, C., and Sack, I. (2007). Fractional encoding of harmonic motions in MR elastography. *Magnetic Resonance in Medicine*, 57(2):388–395. (page 48), (page 93), (page XIII)

[Sack et al., 2008] Sack, I., Beierbach, B., Hamhaber, U., Klatt, D., and Braun, J. (2008). Non-invasive measurement of brain viscoelasticity using magnetic resonance elastography. *NMR in Biomedicine*, 21(3):265–271. (page 42), (page 43), (page 48)

[Sack et al., 2009] Sack, I., Rump, J., Elgeti, T., Samani, A., and Braun, J. (2009). MR elastography of the human heart: Noninvasive assessment of myocardial elasticity changes by shear wave amplitude variations. *Magnetic Resonance in Medicine*, 61(3):668–677. (page 50)

[Sapareto and Dewey, 1984] Sapareto, S. A. and Dewey, W. C. (1984). Thermal dose determination in cancer therapy. *International Journal of Radiation Oncology*Biology*Physics*, 10(6):787–800. (page 29), (page 37)

[Sapin-de Brosses et al., 2010] Sapin-de Brosses, E., Gennisson, J.-L., Pernot, M., Fink, M., and Tanter, M. (2010). Temperature dependence of the shear modulus of soft tissues assessed by ultrasound. *Physics in medicine and biology*, 55(6):1701–1718. (page 37)

[Schlesinger et al., 2013] Schlesinger, D., Benedict, S., Diederich, C., Gedroyc, W., Klibanov, A., and Larner, J. (2013). MR-guided focused ultrasound surgery, present and future. *Medical Physics*, 40(8). (page 12)

[Schregel et al., 2012] Schregel, K., Née Tysiak, E., Garteiser, P., Gemeinhardt, I., Prozorovski, T., Aktas, O., Merz, H., Petersen, D., Wuerfel, J., and Sinkus, R. (2012). Demyelination reduces brain parenchymal stiffness quantified in vivo by magnetic resonance elastography. *Proceedings of the National Academy of Sciences of the United States of America*, 109(17):6650–6655. (page 36)

[Seki et al., 1994] Seki, T., Wakabayashi, M., Nakagawa, T., Itho, T., Shiro, T., Kunieda, K., Sato, M., Uchiyama, S., and Inoue, K. (1994). Ultrasonically guided percutaneous microwave coagulation therapy for small hepatocellular carcinoma. *Cancer*, 74(3):817–825. (page 11)

[Seror et al., 2008] Seror, O., Lepetit-Coiffé, M., Bail, B., Senneville, B., Trillaud, H., Moonen, C., and Quesson, B. (2008). Real time monitoring of radiofrequency ablation based on MR thermometry and thermal dose in the pig liver in vivo. *European Radiology*, 18(2):408–416. (page 29)

[Silverman et al., 1999] Silverman, S. G., Tuncali, K., Adams, D. F., Nawfel, R. D., Zou, K. H., and Judy, P. F. (1999). CT fluoroscopy-guided abdominal interventions: techniques, results, and radiation exposure. *Radiology*, 212(3):673–681. (page 11)

[Sinkus et al., 2000] Sinkus, R., Lorenzen, J., Schrader, D., Lorenzen, M., Dargatz, M., and Holz, D. (2000). High-resolution tensor MR elastography for breast tumour detection. *Physics in Medicine and Biology*, 45(6):1649–1664. (page 35)

[Sinkus et al., 2005] Sinkus, R., Tanter, M., Xydeas, T., Catheline, S., Bercoff, J., and Fink, M. (2005). Viscoelastic shear properties of in vivo breast lesions measured by MR elastography. *Magnetic resonance imaging*, 23(2):159–165. (page 51), (page 60), (page 61)

[Souchon et al., 2003] Souchon, R., Rouvière, O., Gelet, A., Detti, V., Srinivasan, S., Ophir, J., and Chapelon, J.-Y. (2003). Visualisation of HIFU lesions using elastography of the human prostate in vivo: preliminary results. *Ultrasound in Medicine & Biology*, 29(7):1007–1015. (page 37)

[Stafford et al., 1998] Stafford, R. J., Kallel, F., Price, R. E., Cromeens, D. M., Krouskop, T. A., Hazle, J. D., and Ophir, J. (1998). Elastographic imaging of thermal lesions in soft tissue: a preliminary study in vitro. *Ultrasound in Medicine & Biology*, 24(9):1449–1458. (page 36), (page 37)

[Streitberger et al., 2012] Streitberger, K.-J., Sack, I., Krefting, D., Pfüller, C., Braun, J., Paul, F., and Wuerfel, J. (2012). Brain viscoelasticity alteration in chronic-progressive multiple sclerosis. *PLoS ONE*, 7(1). (page 36)

[Tacke et al., 1999] Tacke, J., Speetzen, R., Heschel, I., Hunter, D. W., Rau, G., and Günther, R. W. (1999). Imaging of Interstitial Cryotherapy—Anin VitroComparison of Ultrasound, Computed Tomography, and Magnetic Resonance Imaging. *Cryobiology*, 38(3):250–259. (page 12)

[Talwalkar et al., 2008] Talwalkar, J. A., Yin, M., Fidler, J. L., Sanderson, S. O., Kamath, P. S., and Ehman, R. L. (2008). Magnetic resonance imaging of hepatic fibrosis: Emerging clinical applications. *Hepatology*, 47(1):332–342. (page 42), (page 43)

[Tatli et al., 2010] Tatli, S., Acar, M., Tuncali, K., Morrison, P. R., and Silverman, S. (2010). Percutaneous cryoablation techniques and clinical applications. *Diagnostic and Interventional Radiology (Ankara, Turkey)*, 16(1):90–95. (page 8)

[Thörmer et al., 2013] Thörmer, G., Reiss-Zimmermann, M., Otto, J., Hoffmann, K.-T., Moche, M., Garnov, N., Kahn, T., and Busse, H. (2013). Novel technique for MR elastography of the prostate using a modified standard endorectal coil as actuator. *Journal of Magnetic Resonance Imaging*, 37(6):1480–1485. (page 44)

[Tsao and Kozerke, 2012] Tsao, J. and Kozerke, S. (2012). MRI temporal acceleration techniques. *Journal of Magnetic Resonance Imaging*, 36(3):543–560. (page 24)

[Tse et al., 2011] Tse, Z., Chan, Y., Janssen, H., Hamed, A., Young, I., and Lamperth, M. (2011). Piezoelectric actuator design for MR elastography: Implementation and vibration issues. *International Journal of Medical Robotics and Computer Assisted Surgery*, 7(3):353–360. (page 42)

[Uchida et al., 1995] Uchida, M., Imaide, Y., Sugimoto, K., Uehara, H., and Watanabe, H. (1995). Percutaneous cryosurgery for renal tumours. *British Journal of Urology*, 75(2):132–137. (page 11)

[Uffmann et al., 2002] Uffmann, K., Abicht, C., Grote, W., Quick, H., and Ladd, M. (2002). Design of an MR-compatible piezoelectric actuator for MR elastography. *Concepts in Magnetic Resonance Part B: Magnetic Resonance Engineering*, 15(4):239–254. (page 42), (page 44)

[Unger et al., 1988] Unger, E., Littlefield, J., and Gado, M. (1988). Water content and water structure in CT and MR signal changes: possible influence in detection of early stroke. *American Journal of Neuroradiology*, 9(4):687–691. (page 58)

[Van Houten et al., 1999] Van Houten, E., Paulsen, K., Miga, M., Kennedy, F., and Weaver, J. (1999). An overlapping subzone technique for MR-based elastic property reconstruction. *Magnetic Resonance in Medicine*, 42(4):779–786. (page 61)

[Vappou et al., 2009] Vappou, J., Maleke, C., and Konofagou, E. E. (2009). Quantitative viscoelastic parameters measured by harmonic motion imaging. *Physics in Medicine and Biology*, pages 3579–3594. (page 33)

[Varghese et al., 2002] Varghese, T., Zagzebski, J. A., and Lee Jr., F. T. (2002). Elastographic imaging of thermal lesions in the liver in vivo following radiofrequency ablation: preliminary results. *Ultrasound in Medicine & Biology*, 28(11–12):1467–1473. (page 36)

[Wang et al., 2007] Wang, H., Weaver, J. B., Doyley, M. M., Kennedy, F. E., and Paulsen, K. D. (2007). A phase unwrapping method for large-motion phase data in MR elastography. *Proc. SPIE 6511*, pages 65111S–65111S. (page 60)

[Wang et al., 2011] Wang, H., Weaver, J. B., Perreard, I. I., Doyley, M. M., and Paulsen, K. D. (2011). A three-dimensional quality-guided phase unwrapping method for MR elastography. *Physics in Medicine and Biology*, 56(13):3935. (page 109)

[Weaver et al., 1999] Weaver, J., Van Houten, E., Miga, M., Kennedy, F., Hartov, A., Poplack, S., Nagy, H., and Paulsen, K. (1999). Measurement of harmonic motion for MR elastography. In *Proc. ISMRM, 7th Meeting (Philadelphia, PA)*, page 1617. (page 42)

[Weaver et al., 2012] Weaver, J. B., Pattison, A. J., McGarry, M. D., Perreard, I. M., Swienckowski, J. G., Eskey, C. J., Lollis, S. S., and Paulsen, K. D. (2012). Brain mechanical property measurement using MRE with intrinsic activation. *Physics in Medicine and Biology*, 57(22):7275. (page 43)

[Webb et al., 2011] Webb, H., Lubner, M., and Hinshaw, J. (2011). Thermal Ablation. *Seminars in Roentgenology*, 46(2):133–141. (page XI)

[Wu et al., 2001] Wu, T., Felmlee, J., Greenleaf, J., Riederer, S., and Ehman, R. (2001). Assessment of thermal tissue ablation with MR elastography. *Magnetic Resonance in Medicine*, 45(1):80–87. (page 37), (page 38)

[Wu et al., 2000] Wu, T., Felmlee, J. P., Greenleaf, J. F., Riederer, S. J., and Ehman, R. L. (2000). MR imaging of shear waves generated by focused ultrasound. *Magnetic Resonance in Medicine*, 43(1):111–115. (page 43)

[Wust and Gellermann, 2007] Wust, P. and Gellermann, J. (2007). Regional Thermotherapy. In MD, P. M. S., Stein, U., and MD, A. M. M. E., editors, *Regional Cancer Therapy*, Cancer Drug Discovery and Development, pages 73–90. Humana Press. (page 5)

[Yin et al., 2007] Yin, M., Talwalkar, J., Glaser, K., Manduca, A., Grimm, R., Rossman, P., Fidler, J., and Ehman, R. (2007). Assessment of Hepatic Fibrosis With Magnetic Resonance Elastography. *Clinical Gastroenterology and Hepatology*, 5(10):1207–1213.e2. (page 36)

[Yuan et al., 2007] Yuan, L., Glaser, K. J., Rouviere, O., Gorny, K. R., Chen, S., Manduca, A., Ehman, R. L., and Felmlee, J. P. (2007). Preliminary assessment of one-dimensional MR elastography for use in monitoring focused ultrasound therapy. *Physics in Medicine and Biology*, 52(19):5909. (page 43)

[Yutzy and Duerk, 2008] Yutzy, S. R. and Duerk, J. L. (2008). Pulse sequences and system interfaces for interventional and real-time MRI. *Journal of Magnetic Resonance Imaging*, 27(2):267–275. (page 26)

[Zebker and Lu, 1998] Zebker, H. A. and Lu, Y. (1998). Phase unwrapping algorithms for radar interferometry: residue-cut, least-squares, and synthesis algorithms. *Journal of the Optical Society of America A*, 15(3):586–598. (page 60)

[Zhang et al., 1998] Zhang, Q., Chung, Y.-C., Lewin, J. S., and Duerk, J. L. (1998). A method for simultaneous RF ablation and MRI. *Journal of Magnetic Resonance Imaging*, 8(1):110–114. (page 11)

[Zhao et al., 2008] Zhao, X., Zheng, Y., Liang, J., Chan, Q., Yang, X., Li, G., and Yang, E. (2008). In vivo tumor detection on rabbit with biopsy needle as MRE driver. *Annual*

International Conference of the IEEE Engineering in Medicine and Biology Society., 2008:121–124. (page 44)

[Zorgani et al., 2015] Zorgani, A., Souchon, R., Dinh, A.-H., Chapelon, J.-Y., Ménager, J.-M., Lounis, S., Rouvière, O., and Catheline, S. (2015). Brain palpation from physiological vibrations using MRI. *Proceedings of the National Academy of Sciences of the United States of America*, 112(42):12917–12921. (page 43)

Appendix A

Needle MRE driver - First version

The first version of the needle MRE driver is composed of a piezoelectric actuator (APA™ 150M, Cedrat) mounted on an MR-compatible needle (Fig. A.1). This version required someone to hold the needle during the experiments. Relevant characteristics of the actuator are reported in Table A.1. A preliminary study was carried out to evaluate the maximum displacement as a function of the applied excitation frequency, in the absence of any mechanical load (Fig.A.2). The actuator is hand held thanks to a handle. Maximum displacement varies between $50\mu m$ at 200 Hz and $105\mu m$ at 10 Hz.

Properties APA™150M	Value	Tolerance
Height	22 mm	± 0.2 mm
Length	55.10 mm	± 0.1 mm
Width	5 mm	± 0.05 mm
Unloading resonance frequency	1300 Hz	± 195 Hz
Blocking force	100 N	± 20 N
Max. no load displacement	169 μm	± 41 μm

Table A.1 – Standard properties of use and measurement of the actuator APA150M

.

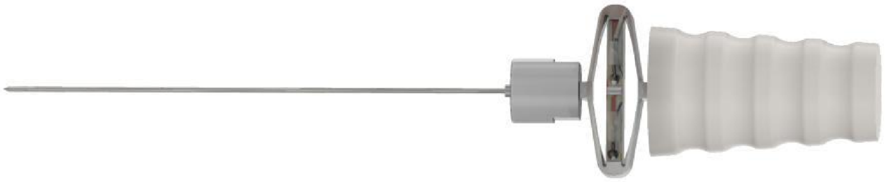

Figure A.1 – First version of the needle MRE driver.

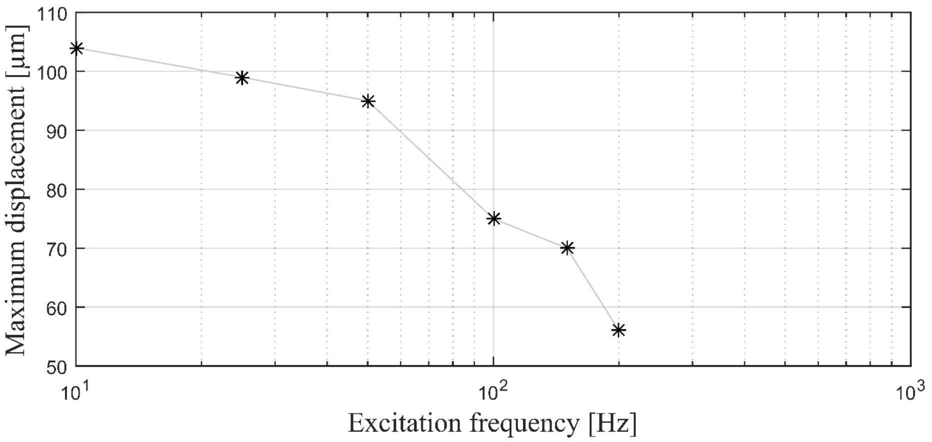

Figure A.2 – Maximum displacement of the needle obtained with the first version of the needle MRE driver as a function of the applied frequency, in the absence of mechanical load

Appendix B

Needle MRE driver - Second version

The second version of the needle MRE driver includes a more compact ring-shaped piezoelectric actuator (CMBR08, Noliac ®). The designed device is a small flat disk, 92 mm in diameter and 30 mm thick, that is placed on the skin of the patient. Then, the needle is manually inserted in its center (Fig.B.1). The needle is locked by a pneumatic clamping system that is remotely controlled. the whole system is made out of plastic and custom 3D printed elements, except for the piezoelectric actuator. This system can be easily adapted to any needle diameter by adapting the clamping ring. The radiologists does not need to hold the needle. Main relevant properties of the actuator are listed in Table.B.1. The maximum displacement was assessed as a function of the applied excitation frequency. Similarly to the first version of the device, measurements were performed in the absence of any mechanical load (Fig.B.2). Maximum displacement of the needle with no load varies between 180 μm and 280 μm. Two resonance frequencies are highlighted by this analysis (30 Hz and 115 Hz).

Properties CMBR08	Value	Tolerance
Height	1.3 mm	± 0.1 mm
Outer diameter	40 mm	± 1.20 mm
Inner diameter	8 mm	± 0.25 mm
Unloading resonance frequency	3400 Hz	
Blocking force	39 N	± 7.8 N
Max. no load displacement	230 μm	± 17.25 μm

Table B.1 – Standard properties of use and measurement of the actuator CMBR08

.

Figure B.1 – Second version of the needle MRE driver, based on a ring-shaped piezoelectric actuator.

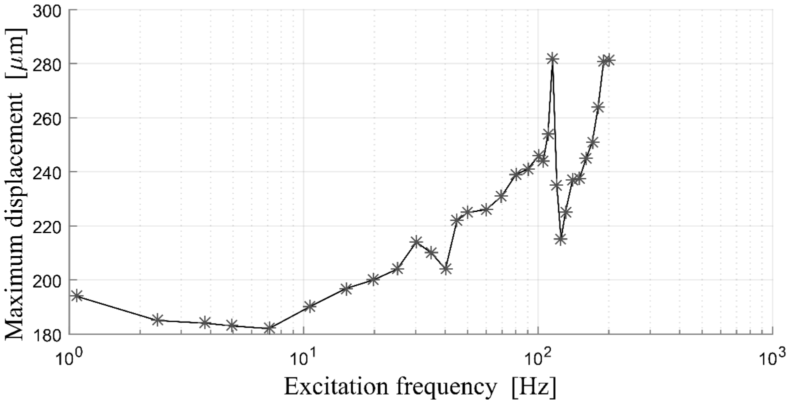

Figure B.2 – Maximum displacement of the needle obtained with the second version of the needle MRE driver as a function of the applied frequency.

Appendix C

Impact of the laser fibers on the wave propagation

Based on the results of the in vivo laser ablation monitoring, the impact of the laser fibers on the wave propagation was investigated. Indeed, a dramatic decrease in the wave amplitude that was propagating in the fiber region was observed during the experiment. Contrary to ex vivo experiments, laser fibers were almost parallel to the needle MRE driver.

Material and Method

Numerical simulations on the software COMSOL Multiphysics ® are performed in order to verify the following hypothesis: the orientation and the position of the fibers can affect the wave propagation. A setup including the liver, the needle MRE driver and 4 laser fibers is modeled on the software so that conditions of experiments are reproduced (Fig.C.1). The fiber laser is inclined at $\alpha = 15°$ to the axis of the needle MRE driver. Another configuration $\alpha = 90°$ is tested to simulate the conditions of the ex vivo experiment. Fiber tips are within a 0.8 cm square and placed at 2 cm from the needle MRE driver. A wave is generated by simulating a displacement of the needle with a excitation frequency of 50 Hz.

Results

The map of the vertical displacement at a given time in the plane perpendicular to the needle MRE driver and including the simulated ablated region is shown in Fig.C.2. The wave is circularly propagating around the needle MRE driver except in the region where the fibers are. The displacement in the fiber area is plotted as a function of time in Fig.C.3 and is compared to displacement observed without fibers. The two cases ($\alpha = 15°$ and $90°$) are compared. When $\alpha = 15°$, the displacement in the fiber area is decreased by a factor 5 relative to the displacement measured outside this area. Although the wave amplitude

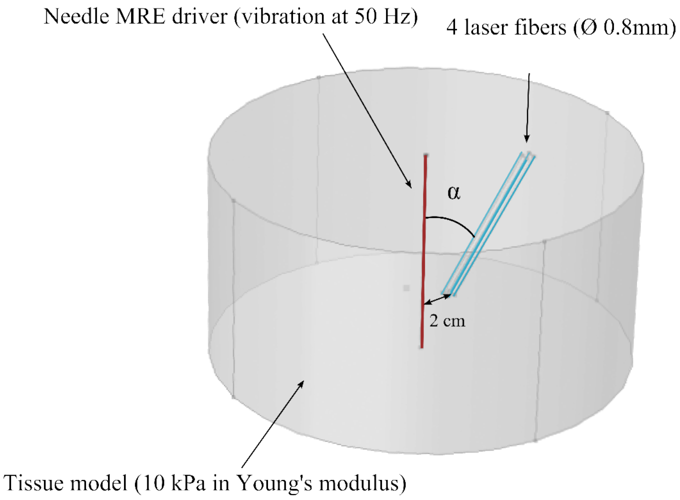

Figure C.1 – Experimental setup modeled on the simulation software. The model includes the needle MRE driver and the 4 laser fibers inserted with an angle α to the axis of the needle MRE driver.

is still reduced when $\alpha = 90°$, this position allows to improve the wave propagation in this area.

Conclusion

This study raises an important issue. The position of the fibers may affect the wave propagation generated by the needle MRE driver. Further investigations are needed to determine the optimal position, orientation and number of fibers that would ensure the possibility of reconstructing an elastogram inside the region of interest.

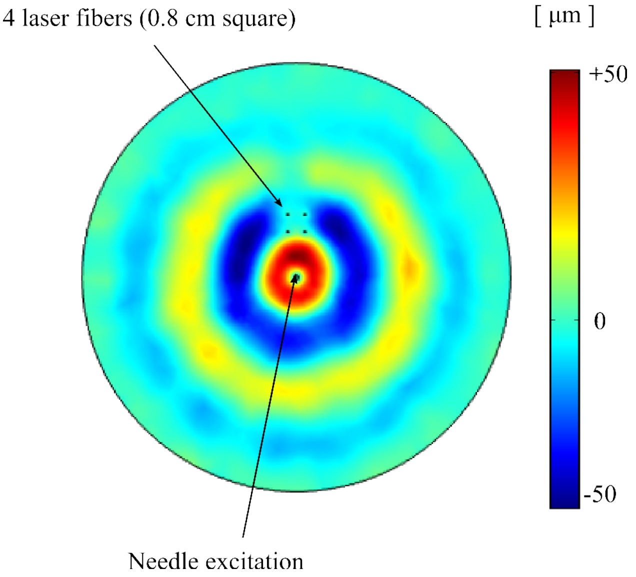

Figure C.2 – Displacement map in the horizontal plane that includes the fiber tips ($\alpha = 15°$). The wave is propagating around the needle MRE driver, except in the fiber area.

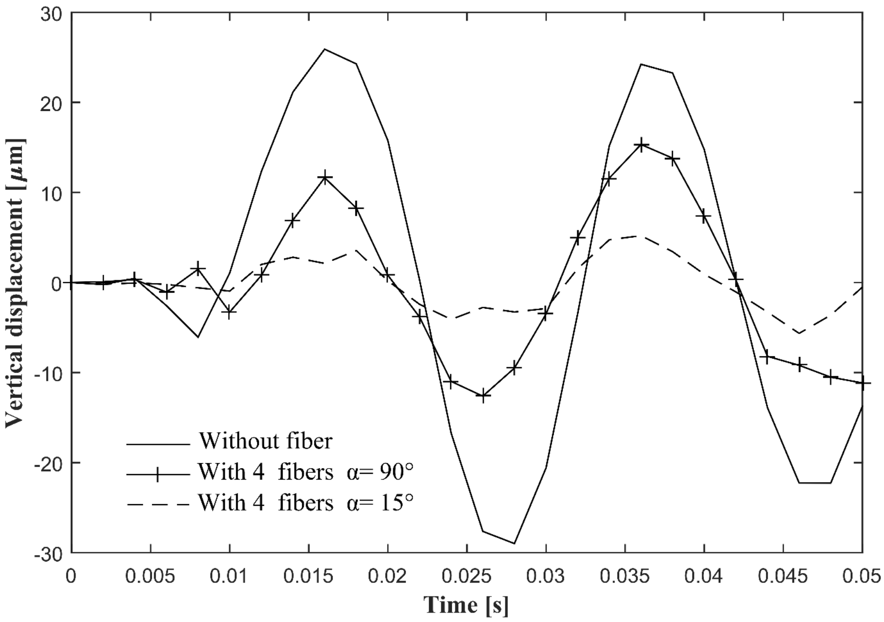

Figure C.3 – Displacement amplitude in the fiber area as a function of time in three configurations: $\alpha = 15°$(dotted line) and $\alpha = 90°$ (cross line) compared to the reference without fiber (solid line).

Appendix D

Publications

Peer-reviewed articles in international journals

N. Corbin, E. Breton, M. de Mathelin, and J. Vappou. MR elastography without phase image reconstruction: a new approach based on direct k-space raw data processing. *Magnetic Resonance in Medicine*, under review.

S. Chatelin, I. Charpentier, N. Corbin, L. Meylheuc, and J. Vappou. An automatic differentiation-based gradient method for shear wave inversion in magnetic resonance elastography: specific application in fibrous soft tissues. *Physics in Medicine and Biology*, under review.

N. Corbin, J. Vappou, E. Breton, Q. Boehler, L. Barbé, P. Renaud, and M. de Mathelin. Interventional MR elastography for MRI-guided percutaneous procedures. *Magnetic Resonance in Medicine*, 2015.

International conferences

N. Corbin, E. Breton, M. de Mathelin, and J. Vappou. Feasibility study of interventional magnetic resonance elastography for the monitoring of MR-guided percutaneous thermal ablations. *International Tissue Elasticity Conference, Verona, Italy*, 2015 (oral).

S. Chatelin, N. Corbin, I. Charpentier, and J. Vappou. An automatic differentiation of the 1D viscoelastic green's functions for magnetic resonance elastography reconstruction in anisotropic tissue. *International Tissue Elasticity Conference, Verona, Italy*, 2015 (oral).

N. Corbin, J. Vappou, E. Breton, Q. Boehler, L. Barbé, P. Renaud, and M. de Mathelin. Interventional magnetic resonance elastography for MRI-guided percutaneous procedures. *ISMRM congress, Toronto, Canada*, 2015 (oral). **Magna Cum Laude and first prize of the MRE study group**

N. Corbin, E. Breton, Q. Boehler, L. Barbé, P. Renaud, M. de Mathelin, and J. Vappou. All-in-one interventional MR elastography (MRE) system dedicated to MR-guided percutaneous procedures. *ISMRM congress, Milan, Italy*, 2014 (poster). **Stipend from the French Society of Magnetic Resonance in Biology and Medicine.**

N. Corbin, Q. Boehler, L. Barbé, P. Renaud, E. Breton, M. de Mathelin, and J. Vappou. Assisting MRI-guided percutaneous procedures with elastography: development of an interventional MR-elastography protocol. *International Tissue Elasticity Conference, London UK*, 2013 (oral).

Appendix E

Résumé en français

Introduction

La recherche contre le cancer vise à assurer au patient une vie la plus normale et longue possible tout en minimisant les risques et les complications du traitement. Parmi les grandes avancées de ces dernières années, figurent les procédures d'ablations thermiques percutanées. Ces dernières consistent à générer la nécrose des cellules visées en appliquant des températures très élevées (> 50°C) ou très faibles ($<$ 40°C). Les ablations thermiques présentent l'avantage de cibler la zone à traiter tout en minimisant les dommages aux tissus alentours. Un applicateur est inséré à travers la peau du patient jusqu'à la tumeur. Par radio-fréquences, laser, micro-ondes ou encore cryothérapie, la température est localement modifiée à l'extrémité de l'applicateur afin de détruire la tumeur [Webb et al., 2011]. Afin de guider le geste du praticien et de suivre en temps réel les effets de l'ablation sur les tissus, plusieurs techniques d'imagerie peuvent être employées: imagerie ultrasonore, imagerie par rayons X, imagerie par résonance magnétique (IRM). L'IRM offre la possibilité de choisir librement la position et l'orientation des coupes, d'obtenir un contraste dans les tissus mous, d'acquérir des images en temps réel et d'assurer l'absence de radiations ionisantes pour le patient et le praticien [Kahn and Busse, 2012]. L'IRM est d'autant plus appréciée en radiologie interventionnelle qu'une carte de température actualisée en temps réel peut être obtenue, ce qui permet de s'assurer d'atteindre la température de destruction des cellules empiriquement établie. Alors que le suivi des ablations thermiques est essentiel au bon déroulement de la procédure afin de s'assurer de la destruction complète de la tumeur et d'éviter d'endommager les tissus sains alentours, aucune information intrinsèque concernant l'état des tissus traités n'est disponible. L'objectif de ce projet vise à améliorer le suivi des ablations thermiques en apportant au radiologue une information supplémentaire liée aux propriétés mécaniques des tissus. Plusieurs études ont démontré l'altération de ces propriétés lors d'une ablation thermique et la pertinence de mesurer leurs changements afin de suivre avec précision une ablation. En IRM, les propriétés mécaniques des tissus sont mesurables par Elastographie par Résonance Magnétique (ERM)[Muthupillai et al., 1995].

Le principe de l'ERM est illustré Figure E.1. Grâce à un excitateur mécanique, une onde est générée à travers le tissu, le déplacement des particules engendré par cette vibration est encodé sur les images IRM de phase. Sachant que la vitesse de propagation des ondes dépend des propriétés mécaniques du tissu, il est possible de reconstruire une carte d'élasticité à partir des images acquises. L'ERM est aujourd'hui une technique utilisée cliniquement pour le diagnostic de certaines pathologies. Cependant, la durée d'acquisition et le temps de reconstruction nécessaires à l'obtention d'un élastogramme sont actuellement trop importants pour pouvoir utiliser l'ERM comme mesure en temps réel des changements des propriétés mécaniques lors d'une ablation thermique.Ce projet vise donc à développer l'ERM interventionnelle dédiée au suivi des procédures d'ablations thermiques. Deux approches sont explorées. La première consiste à développer un système complet d'ERM répondant aux critères de l'IRM interventionnelle. La seconde est consacrée au développement d'une méthode alternative de traitement des données acquises en ERM visant à rendre le procédé plus robuste et rapide.

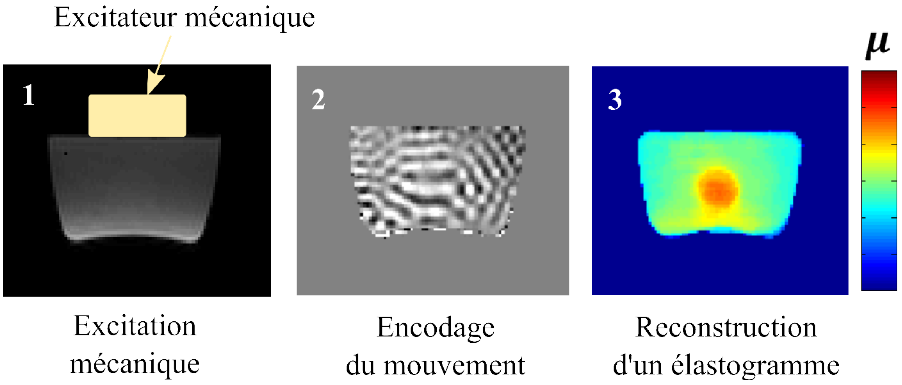

Figure E.1 – Principe de l'ERM illustré sur un gel de gélatine composé d'une inclusion plus rigide. Un excitateur mécanique génère une onde à travers le tissu. Le déplacement des particules induit par l'excitation est encodé sur les images IRM de phase. Sachant que la vitesse de propagation dépend des propriétés mécaniques des tissus traversés, la vitesse de propagation de l'onde est estimée à partir des images pour pouvoir reconstruire une carte d'élasticité.

Développement d'un système d'ERM interventionnelle

La première partie de ce projet vise à développer un système tout-en-un d'ERM interventionnelle composé d'un excitateur mécanique adapté aux contraintes de l'IRM interventionnelle, d'une séquence IRM d'encodage du mouvement permettant d'acquérir des images rapidement et d'un algorithme de reconstruction des élastogrammes répondant au besoin d'un taux de rafraichissement élevé des informations.

Excitateur ERM à aiguille

L'excitateur conventionnel d'ERM est un excitateur surfacique large que l'on pose sur la peau du patient. Cette configuration n'est pas adaptée à l'IRM interventionnelle car elle encombre l'espace de manipulation du radiologue déjà restreint et ne permet pas d'atteindre les régions profondes du corps du patient. Inspiré de la littérature en ERM [Chan et al., 2006], un excitateur à aiguille a spécifiquement été développé pour l'ERM interventionnelle (Fig.E.2. Un moteur piézoélectrique fait vibrer une aiguille dans le sens de sa longueur à une fréquence définie par l'opérateur. Puisque des aiguilles sont déjà utilisées lors d'une procédure percutanée, il semble que ce type d'excitateur soit le plus adapté. Outre son encombrement limité, l'avantage de cet excitateur est de focaliser la source de l'onde directement dans la région d'intérêt à des fréquences élevées ce qui contribue à une meilleure résolution de l'élastogramme.

Figure E.2 – Excitateur ERM à aiguille. Un moteur piezoelectrique est synchronisé avec la séquence IRM. Le moteur fait vibrer l'aiguille dans le sens de sa longueur.

Séquence rapide et interactive d'encodage du mouvement

Une séquence d'encodage du mouvement est caractérisée par l'implémentation d'un gradient bipolaire supplémentaire ce qui allonge significativement la durée d'acquisition des images ERM. Afin de réduire au maximum cette durée pour répondre aux besoins de l'IRM interventionnelle, les gradients d'encodage du mouvement (Motion Encoding Gradient, MEG) ont été implémentés sur une séquence d'écho de gradient rapide (Fig.E.3). Grâce à l'encodage fractionnel [Rump et al., 2007], l'acquisition d'une image nécessite entre 1 à 2 secondes. Cette séquence présente aussi l'avantage d'être interactive ce qui signifie que l'opérateur peut modifier la position et l'orientation des coupes sans interrompre l'acquisition [Pan et al., 2011] ce qui est très apprécié en IRM interventionnelle pour suivre les déplacements de l'aiguille en temps réel.

La durée d'acquisition d'une image n'est pas le seul paramètre à améliorer pour accélérer le protocole d'ERM puisque la reconstruction d'un élastogramme nécessite l'acquisition de plusieurs images de phase, généralement 8. Plusieurs images sont acquises avec différents décalages entre les gradients et l'excitation mécanique afin de pouvoir procéder à une analyse harmonique et filtrer tous les mouvements encodés qui ne sont pas dus à l'excitation générée. De plus, chaque image est acquise deux fois en inversant la polarité des gradients pour supprimer la constante de phase et multiplier par deux l'encodage du mouvement.

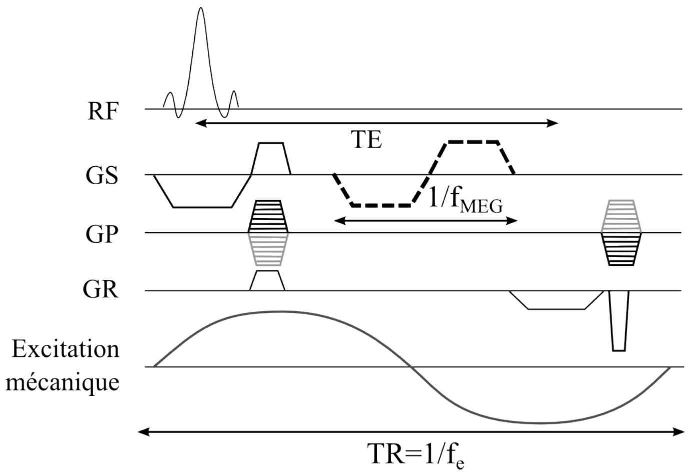

Figure E.3 – Chronogramme de la séquence d'écho de gradient rapide avec encodage du mouvement dédié à l'ERM interventionnelle. Le gradient d'encodage (MEG) est ici dans la direction de sélection de coupe (tirets). Le temps de répétition, TR, correspond à une période de vibration de l'excitation mécanique $1/f_e$. Le temps d'écho (TE) est minimisé grâce à l'encodage fractionnel ($f_{MEG} > f_e$).

Après une étude préliminaire, il s'est avéré que l'acquisition de 3 paires d'images de phase répondait au mieux au compromis temps/qualité de l'élastogramme ce qui réduit le temps total d'acquisition du jeu d'images nécessaire à la reconstruction d'un seul élastogramme.

Algorithme optimisé de reconstruction des élastogrammes

La dernière étape en ERM consiste à traiter les images de phase pour reconstruire une carte d'élasticité. Les images sont d'abord pré-traitées (différence puis analyse harmonique) afin de visualiser au mieux l'onde encodée puis un algorithme de résolution du problème inverse est appliqué à l'image finale afin de retourner un élastogramme. L'algorithme utilisé est l'algorithme d'estimation locale de fréquence [Knutsson et al., 1994, Manduca et al., 2001] qui a l'avantage d'être robuste et de nécessiter le minimum d'images IRM pour reconstruire un élastogramme. Tout ce procédé a été implémenté sur Matlab de telle sorte que les images sont traitées en temps réel. Afin d'augmenter le taux de rafraichissement des élastogrammes, le principe de fenêtre glissante a été implémenté: 6 images sont nécessaires à la reconstruction d'un seul élastogramme, mais un élastogramme est reconstruit toutes les paires d'images acquises (Fig.E.4). Chaque élastogramme est reconstruit à partir d'une nouvelle paire d'images et des 2 paires d'images précédentes déjà utilisées pour les élastogrammes précédents. Le taux de rafraichissement des élastogrammes atteint donc en moyenne 1 élastogramme toutes les 2 secondes. En parallèle, les mesures de température sont aussi effectuées à partir des images acquises [Le et al., 2006].

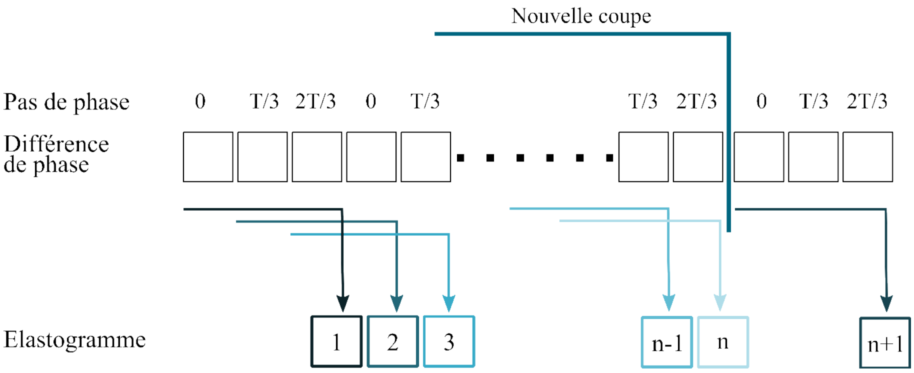

Figure E.4 – Principe de la fenêtre glissante appliqué à la reconstruction des élastogrammes en ERM interventionnelle, ici dans le cas de 3 pas de phase. Un élastogramme est obtenu à partir des deux paires d'images précédentes et la nouvelle. Ainsi, un élastogramme est reconstruit toutes les paires d'images acquises. Si un changement de position ou d'orientation de coupe intervient, trois nouvelles paires d'images sont nécessaires à la reconstruction du prochain élastogramme.

Validation du système

La faisabilité de l'ERM interventionnelle a été étudiée lors de plusieurs expériences. Afin de valider la possibilité de détecter des changements d'élasticité en temps réel, la solidification de la gélatine lors de son refroidissement a été étudiée. Le sytème d'ERM interventionnelle a permis de mesurer avec succès l'augmentation du module de cisaillement avec un taux de rafraichissement d'un élastogramme toutes les 2 secondes (Fig.E.5). Afin d'évaluer la possibilité de détecter des changements d'élasticité au cours d'une ablation thermique, une ablation au laser d'un foie de porc ex vivo a été réalisée sous guidage IRM avec le

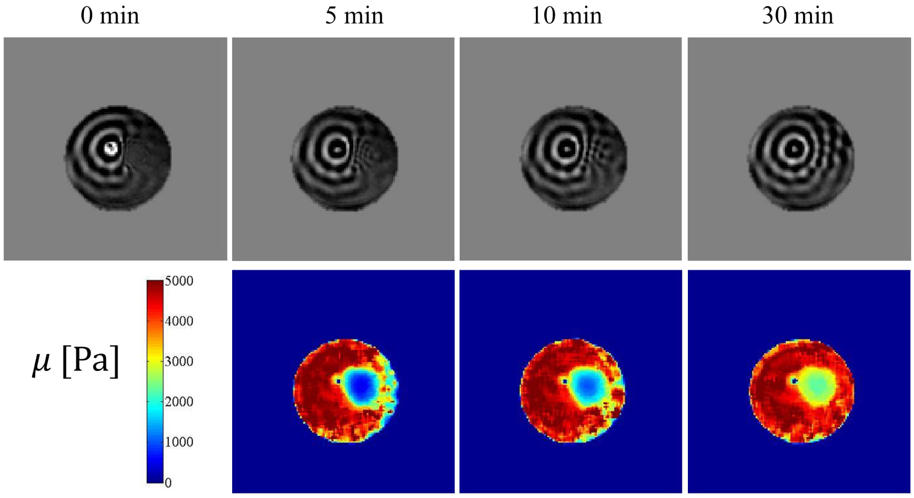

Figure E.5 – Evolution le la vitesse de propagation de l'onde (en haut) et élastogrammes correspondants (en bas) pendant la solidification de la gélatine dans l'inclusion. La longueur d'onde augmente ce qui correspond à l'augmentation de l'élasticité visible sur l'élastogramme.

système d'ERM interventionnelle. L'onde mécanique se propageant autour de l'excitateur mécanique, se déforme dans la région située à droite de l'aiguille, correspondant à un changement d'élasticité dans la lésion (Fig.E.6).

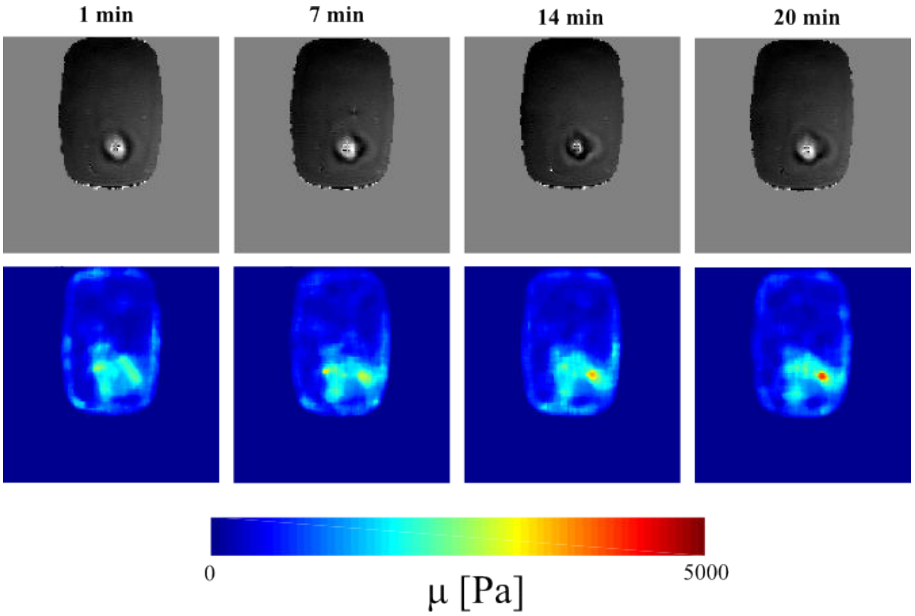

Figure E.6 – Evolution le la vitesse de propagation de l'onde (en haut) et élastogrammes correspondants (en bas) pendant l'ablation laser du foie ex vivo. La longueur d'onde augmente ce qui correspond à l'augmentation de l'élasticité visible sur l'élastogramme.

Une augmentation de l'élasticité dans la zone d'ablation a donc pu être observée avec succès tout au long de la procédure (Fig.E.7). Cette expérience a aussi permis de démontrer que la modification des propriétés structurelles du tissu ex vivo continuait encore un certain temps après avoir éteint le système d'ablation laser.

Après avoir démontré la stabilité et la répétabilité de la méthode in vivo sur modèle porcin en apnée, d'autres expériences ont été menées afin d'évaluer la faisabilité d'un monitorage d'ablation thermique in vivo avec le système d'ERM développé. Afin de pouvoir suivre une ablation de plusieurs minutes, le protocole a été synchronisé sur la respiration. Un nouvel élastogramme est alors calculé à chaque cycle respiratoire. Le suivi d'une ablation laser in vivo a été testé avec ce nouveau protocole. The experimental setup is shown in Fig.E.8.

La mesure simultanée de l'élasticité et de la température ont permis de mettre en valeur un comportement différent du comportement observé lors de l'expérience ex vivo: l'élasticité se stabilise dès que le système d'ablation est éteint (Fig.E.9).

Nouvelle approche de traitement des données en ERM

La seconde partie de ce projet propose une nouvelle approche de traitement des données en ERM diminuant considérablement le nombre d'étapes de traitement des images. Conventionnellement, les images de phase sont reconstruites, puis le déroulement de phase est

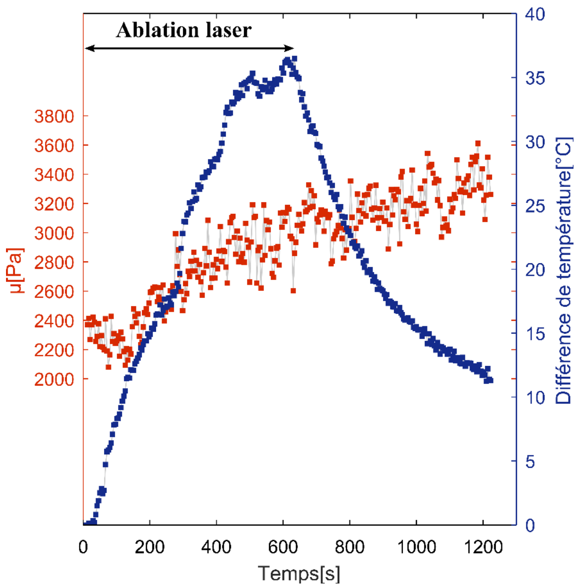

Figure E.7 – Evolution du module de cisaillement (en rouge) et de la température (en bleu) pendant l'ablation thermique d'un foie de porc ex vivo.

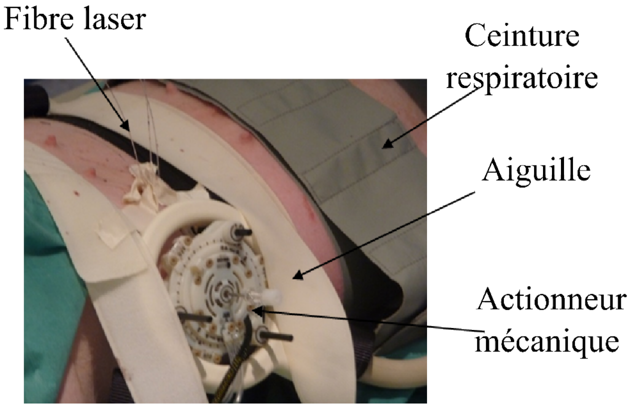

Figure E.8 – Dispositif expérimental de l'expérience d'ablation thermique in vivo. Une ceinture est utilisée pour mesurer le cycle respiratoire et permettre la synchronisation de l'excitation mécanique.Une aiguille est insérée au centre de l'actionneur mécanique. L'antenne est placée autour du dispositid. 4 fibres laser sont insérées dans une région proche du dispositif.

appliqué pour ne pas restreindre les données à $[\ \pi, \pi]$. Les images acquises avec polarité des MEG opposée sont soustraites l'une à l'autre puis l'analyse harmonique est effectuée afin de supprimer les mouvements parasites. L'approche proposée repose sur l'absence de reconstruction d'image de phase ce qui permettrait d'éviter aussi l'étape délicate du déroulement de phase. Cette méthode permettrait d'accélérer le processus et de diminuer les risques d'erreur dûs à la multiplicité des étapes de traitement d'images.

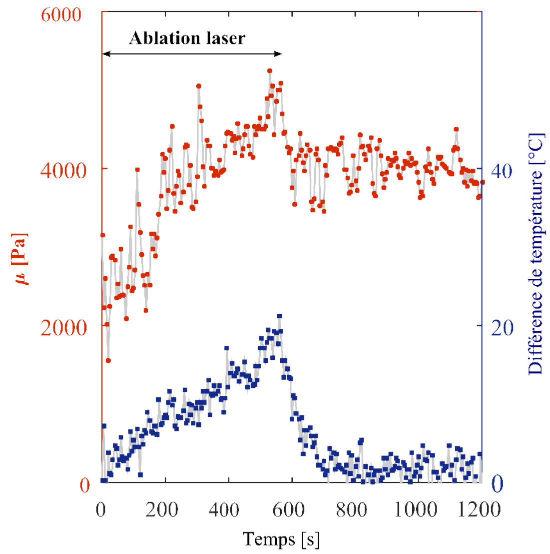

Figure E.9 – Evolution of the shear modulus(in red)and the temperature (in blue) during a laser ablation in swine liver in vivo (Experiment B).

Théorie

En IRM, l'image dans le domaine fréquentiel est d'abord acquise avant de reconstruire une image dans le domaine spatial. En ERM, la mesure des propriétés mécaniques repose sur l'estimation de la vitesse de propagation de l'onde générée, directement associée à sa fréquence spatiale. Basée sur le fait que cette fréquence spatiale se retrouve forcément dans le domaine fréquentiel de l'image, cette approche consiste à étudier les données brutes acquises sans reconstruire les images de phase dans le domaine spatial. Cependant une difficulté apparaît: la fréquence spatiale d'intérêt se situe dans l'image de phase ce qui résulte en une infinité d'harmoniques dans le domaine fréquentiel et non une seule composante fréquentielle comme cela aurait été le cas si la fréquence d'intérêt se situait dans l'image d'amplitude. La solution proposée est inspirée de l'analyse harmonique conventionnelle effectuée en ERM pour sélectionner seulement le mouvement dû à l'excitation générée. L'acquisition de plusieurs images avec des décalages entre le MEG et l'excitation est nécessaire. Une transformée de Fourier temporelle appliquée sur ce jeu de données brutes permet de séparer les différentes harmoniques et de ne sélectionner que la composante d'intérêt.

Plusieurs choix sont alors possibles: 1/ reconstruire une image d'onde pondérée avec la magnitude en appliquant une transformée de Fourier inverse aux données brutes pré-traitées; 2/ reconstruire une carte d'élasticité en appliquant un dérivé de l'algorithme d'estimation locale de fréquence aux données brutes pré-traitées 3/ détecter des changements d'élasticité en étudiant le déplacement des pics fréquentiels dans le domaine fréquentiel (Fig.E.11).

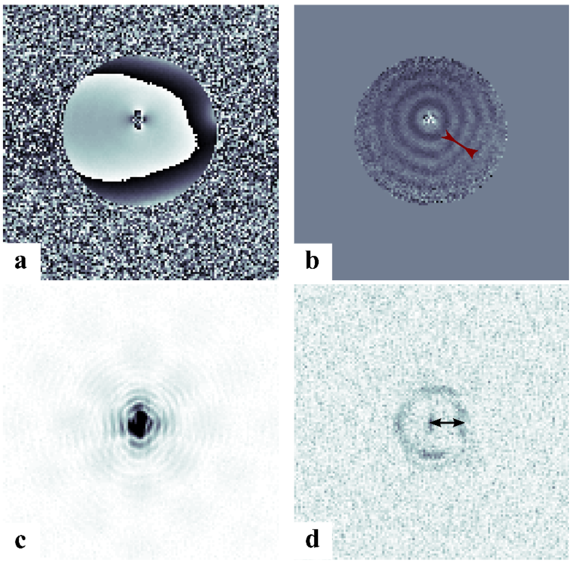

Figure E.10 – a) Image de phase classique provenant d'une acquisition ERM sur gélatine. b) Image reconstruite avec le procédé conventionnel (différence, déroulement de phase) c) Données brutes (en module) acquises dans le domaine des fréquences spatiales d) Mise en valeur des fréquences spatiales d'intérêt après avoir appliqué une analyse harmonique sur les données brutes. la solution proposé fait apparaître un cercle, dont le rayon correspond à la fréquence spatiale observée sur l'image (b).

Application

Cette nouvelle approche a été testée sur gélatine et in vivo sur un modèle porcin. Des images d'ondes et des élastogrammes reconstruits avec la méthode conventionnelle et la nouvelle méthode ont été comparés. Des résultats similaires ont été obtenus alors que la nouvelle méthode a considérablement réduit le nombre d'étapes de traitement des images. Le procédé de solidification de la gélatine a été suivi avec la méthode conventionnelle et la nouvelle approche consistant à détecter le déplacement des pics dans le domaine fréquentiel. Les résultats étaient équivalents alors que la nouvelle approche n'a pas nécessité de reconstruction d'image mais simplement une analyse des données brutes Fig.E.12).

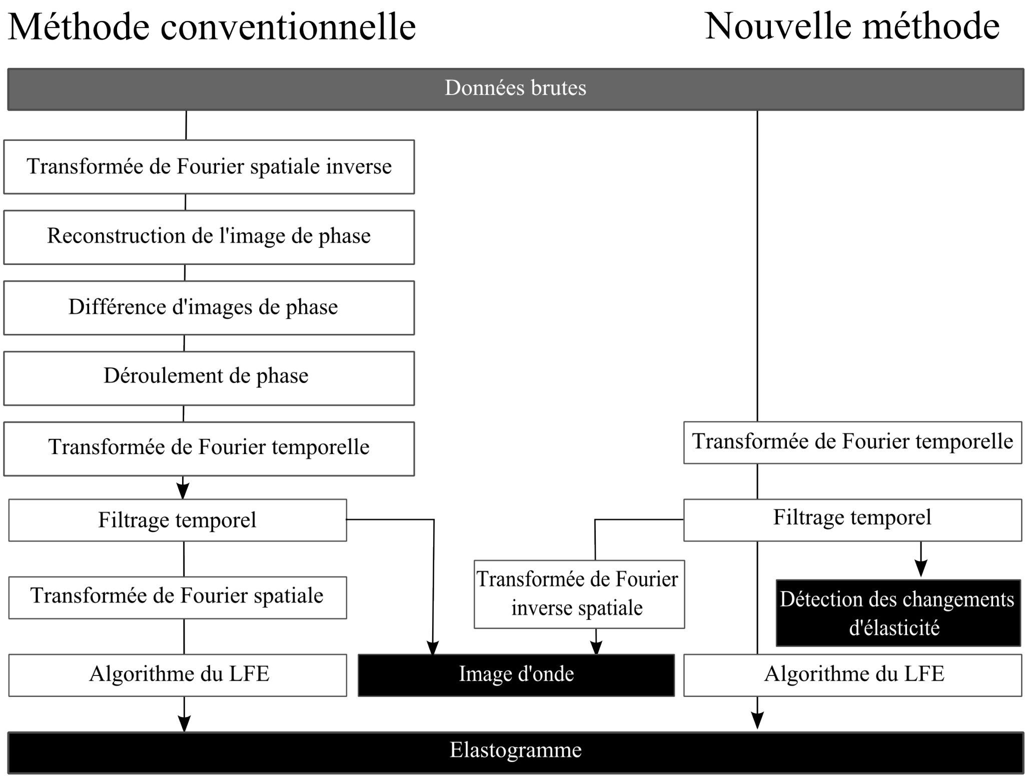

Figure E.11 – Comparaison des procédés de traitement des données avec la méthode conventionnelle et la méthode proposée. Sans reconstruire d'images de phase, il est possible de reconstruire un élastogramme, une image d'onde ou même de détecter des changements d'élasticité temporels.

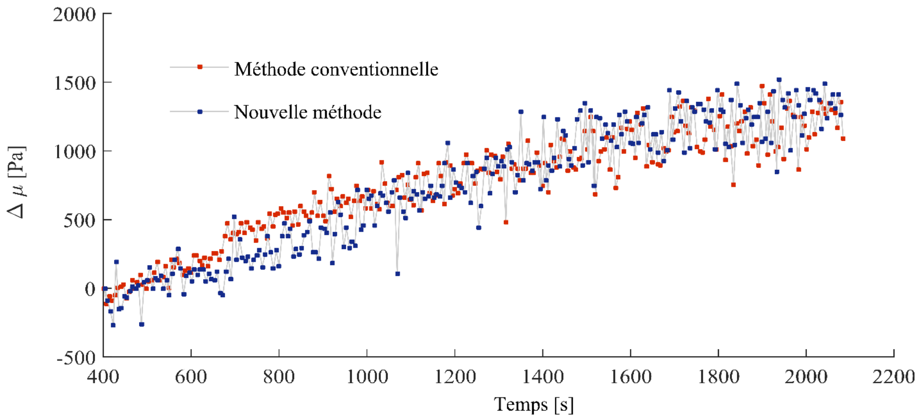

Figure E.12 – Evolution du module de cisaillement de la gélatine en cours de solidification observé à l'aide de la méthode conventionnelle d'ERM (en rouge) et de la nouvelle méthode (en bleu).

Conclusion

Dans le but d'améliorer le suivi d'une ablation thermique, l'ERM interventionnelle a été développée dans ce projet. Plusieurs approches ont été étudiées. La première consistait à développer un système tout-en-un d'ERM interventionnelle. Ce système est composé d'un excitateur à aiguille, d'une séquence IRM d'encodage de gradient rapide et interactive et d'un algorithme de reconstruction des élastogrammmes dont le taux de rafraichissement est optimisé pour répondre aux besoins de l'IRM interventionnelle. La seconde approche testée propose une méthode moins conventionnelle consistant à traiter les données brutes d'ERM. Cette méthode réduit le temps consacré aux traitement des images et limite ainsi le risque d'erreur.